SAND2018-11355R

Evaluation of Spent Nuclear Fuel Disposition in Salt (FY18)

Spent Fuel and Waste Disposition

Prepared for
US Department of Energy
Spent Fuel and Waste Science and Technology

Kristopher L. Kuhlman, Carlos M. Lopez,
Melissa M. Mills, Jessica M. Rimsza,
David C. Sassani

Sandia National Laboratories
September 24, 2018
M2SF-18SN010303031

DISCLAIMER

This information was prepared as an account of work sponsored by an agency of the U.S. Government. Neither the U.S. Government nor any agency thereof, nor any of their employees, makes any warranty, expressed or implied, or assumes any legal liability or responsibility for the accuracy, completeness, or usefulness, of any information, apparatus, product, or process disclosed, or represents that its use would not infringe privately owned rights. References herein to any specific commercial product, process, or service by trade name, trade mark, manufacturer, or otherwise, does not necessarily constitute or imply its endorsement, recommendation, or favoring by the U.S. Government or any agency thereof. The views and opinions of authors expressed herein do not necessarily state or reflect those of the U.S. Government or any agency thereof.

Sandia National Laboratories is a multimission laboratory managed and operated by National Technology and Engineering Solutions of Sandia LLC, a wholly owned subsidiary of Honeywell International Inc. for the U.S. Department of Energy's National Nuclear Security Administration under contract DE-NA0003525.

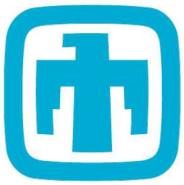

Sandia National Laboratories

SUMMARY

This report summarizes the 2018 fiscal year (FY18) field, laboratory, and modeling work funded by the US Department of Energy Office of Nuclear Energy (DOE-NE) Spent Fuel and Waste Science & Technology (SFWST) campaign as part of the Sandia National Laboratories Salt Research and Development (R&D) and Salt International work packages. This report satisfies level-two milestone M2SF-18SN010303031and comprises three related but stand-alone sections. The first section summarizes the programmatic progress made to date in the DOE-NE salt program and its goals going forward. The second section presents brine composition modeling and laboratory activities related to salt evaporation experiments, which will be used to interpret data collected during the heater test. The third section presents theoretical and numerical modeling work done to investigate the effects brine composition have on dihedral angle and the permeability of salt.

Version 0	September 24	DOE Concurrence	SNL Programmatic Tracking Number 865604
Version 1	October 4	Public Release	

This page is intentionally left blank.

CONTENTS

LIST OF FIGURES

LIST OF TABLES

ACRONYMS

AE	acoustic emissions
CBFO	Carlsbad field office (DOE-EM WIPP office)
DI	deionized
DOE	Department of Energy
DOE-EM	DOE Office of Environmental Management
DOE-NE	DOE Office of Nuclear Energy
DRZ	disturbed rock zone
EBS	engineered barrier system
EDS	energy-dispersive X-ray spectroscopy
EDZ	excavation disturbed zone
ERT	electrical resistivity tomography
FEP	features, events, and processes
FY	fiscal year (October-September)
GDSA	generic disposal system analysis
GRS	Gesellschaft für Anlagen- und Reaktorsicherheit gGmbH
GWB	G-seep WIPP brine
IC	ion chromatography
ICP-OES	inductively coupled plasma optical emission spectrometry
INL	Idaho National Laboratory
GWB	G-seep WIPP brine
LANL	Los Alamos National Laboratory
LBNL	Lawrence Berkeley National Laboratory
LLNL	Lawrence Livermore National Laboratory
MB-139	marker bed 139 (WIPP stratigraphic unit; also MB-140)
MD	molecular dynamics
MS	mass spectrometry
MU-0	map unit 0 (WIPP stratigraphic unit)
NBS	National Bureau of Standards
NEA	Nuclear Energy Agency (part of Organisation for Economic Co-Operation and Development)
NNLS	non-negative least squares
PA	performance assessment
R&D	research and development
RH	relative humidity
ROM	run-of-mine
SDDI	Salt Disposal Defense Investigations (proposed CBFO program)
SDI	Salt Disposal Investigations (proposed CBFO program)
SEM	scanning electron microscopy
SIT	specific ion interaction theory
SITED	salt investigations technical expansive database
SFWST	Spent Fuel & Waste Science & Technology (DOE-NE program)
SNL	Sandia National Laboratories
THMC	thermal-hydrological-mechanical-chemical (also THM & THC)
UFD	Used Fuel Disposition (former DOE-NE program)
URL	underground research laboratory
US	United States
WIPP	Waste Isolation Pilot Plant (DOE-EM site)
XRD	X-ray diffraction
XRF	X-ray fluorescence

This page is intentionally left blank.

EVALUATION OF SPENT NUCLEAR FUEL DISPOSITION IN SALT (FY18)

This report summarizes the 2018 fiscal year (FY18) field, laboratory, and modeling research funded by the US Department of Energy Office of Nuclear Energy (DOE-NE) Spent Fuel and Waste Science & Technology (SFWST) campaign as part of the Sandia National Laboratories Salt Research & Development (R&D) and Salt International work packages. This report satisfies level-two milestone M2SF-18SN010303031.

Three related but stand-alone sections comprise this report. The first section summarizes the progress made to date in the DOE-NE salt program and its goals going forward. The second section presents brine composition modeling and laboratory activities related to salt evaporation experiments, which will be used to interpret data collected during the heater test. The third section presents theoretical and numerical modeling work done to investigate the effects brine composition have on dihedral angle and the permeability of salt.

The Salt R&D and Salt International work packages are focusing on the borehole heater test at the Waste Isolation Pilot Plant (WIPP), which will be the topic of an upcoming 2019 level-2 milestone report. This report summarizes recent work on related and supporting topics.

We acknowledge the team involved in the Salt R&D field test effort, which this work supports. At Sandia National Laboratories (SNL) the team includes Kris Kuhlman, Melissa Mills, Courtney Herrick, Ed Matteo, and Martin Nemer. At Los Alamos National Laboratory (LANL) the team includes Phil Stauffer, Hakim Boukhalfa, Doug Ware, Doug Weaver, Brian Dozier, and Shawn Otto. At Lawrence Berkeley National Laboratory (LBNL) the team includes Jonny Rutqvist and Yuxin Wu. The organization of the borehole heater test at WIPP is outlined in *Project Plan: Salt In-Situ Heater Test* (Sandia, Los Alamos & Lawrence Berkeley National Laboratories), SAND2018-4673R.

1. Salt R&D Program Progress Under UFD and SFWST

Author: Kristopher L. Kuhlman

This report discusses the Salt R&D program's previous (FY14) and current (FY18) goals, presenting major activities funded by DOE-NE under the former Used Fuel Disposition (UFD) program and the current Spent Fuel and Waste Science and Technology (SFWST) program. First, to place the previous and current program goals in context, the background section enumerates salt's benefits and challenges as a disposal medium for heat-generating radioactive waste. The following sections mention highlights from the laboratory, field, modeling, and theoretical programs that have been funded by DOE-NE through the Salt R&D program. Since the Salt R&D program currently has an *in-situ* field-testing focus, this summary recounts the history of the current field test program for disposal of heat-generating waste at WIPP. Salt R&D program future plans include execution of the field test, numerical model developments to benefit generic disposal system analysis (GDSA) integration, and interpretation of data collected as part of the field test.

1.1 Background

Salt's strengths as a host medium for disposal of heat-generating waste are well-known, going back to the 1950s, when geologic salt deposits were first considered promising for radioactive waste disposal (e.g., Hess et al., 1957; Serata & Gloyna, 1959). The United States (US) has extensive bedded and domal salt deposits (Perry et al., 2014). Salt is still currently being researched as a candidate media for future heat-generating radioactive waste disposal in the US (e.g., UFD Campaign, 2012; SNL et al., 2018) because it has favorable containment properties, including:

- Far from excavations, salt is impermeable to brine or gas flow ($\leq 10^{-20}$ m^2; Beauheim & Roberts, 2002);
- Intact salt formations have low porosity ($< 1\%$) and are dry ($< 5\%$ total water);
- Salt has high thermal conductivity (~ 5 W/(m $\cdot$ K)) compared to granite or clay;
- Hypersaline brines associated with salt are biologically simple (NEA, 2018);
- Salt is easily mined with a continuous miner and does not present a silica dust inhalation hazard;
- Granular salt derived from mining can be used to backfill excavations, which will eventually reconsolidate to the same low-porosity and low-permeability properties of undisturbed salt; and
- Salt will creep closed and heal excavations or damage associated with mining.

These containment benefits are illustrated through: 1) geologic stability of salt formations over millions of years, 2) domal salt's common role as a hydrocarbon migration trap over geologic time, 3) worldwide use of solution-mined salt caverns for industrial storage of liquids and gases over decades, and 4) further natural analogues to waste disposal found around the world (e.g., NEA, 2014).

Salt's well-known excellent containment benefits over geologic spatial and temporal scales are tempered by complexities associated with short-term prediction of near-field behavior in salt excavations, including:

- Salt is very soluble in water:
    - Salt is susceptible to rapid dissolution into any fresh water that encounters it;
    - Salt solubility is temperature-sensitive, which is a mechanism behind fluid inclusion migration under a temperature gradient;
    - Salt solubility is stress-sensitive (i.e., pressure solution) at typical conditions; and

  - Salt dissolution into regional groundwater systems can lead to density-driven convection, depending on the system configuration.

- Water exists in geologic salt in multiple forms:
  - Intergranular brine found in variably connected porosity (with connectivity under equilibrium conditions a function of pressure, temperature, and composition – see Section 3 of this report);
  - Fluid inclusions (intragranular brine) migrate under a thermal gradient and will release explosively (i.e., decrepitate) at high temperature, depending on the confining stress;
  - A significant portion of water in bedded evaporite deposits is present as hydrous minerals – each hydrous mineral dehydrates at a different temperature; and
  - The distinction between intragranular and intergranular brine is less clear than the distinction to hydrous minerals.
- Evaporite brines are more complex than dilute waters:
  - Hypersaline brines require complex activity coefficient models (e.g., Pitzer or SIT) to predict waste solubilities, mineral precipitations, and corrosion processes (see Section 2 of this report);
  - Evaporite brines are corrosive to some common engineering materials (e.g., steel); and
  - Hot, chloride-rich brines are associated with acidic condensate (Kuhlman et al., 2017a).
- Salt has complex geomechanical behavior compared to crystalline rocks:
  - Salt cannot support shear stresses (i.e., it creeps due to differential stresses from excavations) and has negligible tensile strength, resulting in continuous transient creep closure and tensile fracture around excavations;
  - Salt requires visco-plastic stress-strain constitutive models to accurately predict its geomechanical behavior;
  - Salt's creep behavior is different under typical laboratory mechanical testing conditions (i.e., high deviatoric stress and high strain rate) and long-term field-relevant stress and strain conditions (i.e., low deviatoric stress and low strain rate); and
  - Materials that undergo large plastic deformations are more difficult to predict in geomechanical simulations than infinitesimal elastic deformation seen in rigid rocks.

From the point of view of long-term performance assessment (PA) (i.e., $\geq$ 10,000 years), the containment benefits offered by the salt host formation at the km-scale significantly outweigh any complexities related to maintaining salt excavations, conducting salt-based laboratory experiments, and predicting short-term and near-field (i.e., m-scale) behaviors.

Motivated by the well-known containment benefits of salt and seeking to better understand the complexities of salt, many laboratory and field tests relevant to radioactive waste disposal have been conducted in salt since the 1950s in the US and Germany. The Waste Isolation Pilot Plant (WIPP) hosted field tests in the 1980s and 1990s related to both its mission (transuranic low-level waste) and heat-generating waste associated with high-level waste. WIPP provides operational disposal experience as the only licensed, operating radioactive waste disposal facility in the world. Germany used the Asse salt mine as an underground research lab (URL) to conduct scientific tests and radioactive waste disposal demonstrations from the 1960s to the early 2000s. Sealing and plugging demonstrations are currently being carried out at the low-level radioactive waste disposal site Morsleben, as this former salt mine is decommissioned.

Several recent DOE-NE Salt R&D reports summarize historic field and laboratory tests conducted mostly at WIPP and Asse, along with a few other locations around the world (e.g., Avery Island salt dome in Louisiana, two Carey salt mines in Kansas, Mississippi Chemical potash mine in New Mexico, and Amélie potash mine in France). Kuhlman et al. (2012) summarized historical field tests in salt, focusing on tests at WIPP. The review process also led to the creation of the "salt investigations technical expansive database" (SITED) web-based knowledge archive (Kuhlman, 2013). Kuhlman & Sevougian (2013) presented a more comprehensive world-wide summary of historical field and laboratory studies in salt, placing each test into a matrix framework of features, events, and processes (FEPs). The report categorized tests by their relation to different aspects of repository long-term performance. Section 4 of Kuhlman & Malama (2013) summarized the results of historic field and laboratory tests involving brine migration during heating in both domal and bedded salt. Kuhlman et al. (2017a) presented a conceptual plan for a new brine-migration borehole heater test at WIPP, with several appendices summarizing aspects of historic tests that were drawn upon for the design of the new test.

1.2 Salt R&D Program Initial Direction

The DOE-NE Salt R&D program began as part of the initial DOE-NE Used Fuel Disposition (UFD) campaign. The initial UFD roadmap exercise (UFD Campaign, 2012) developed a list of priorities based on a methodical ranking system constructed from expert input. Salt was included as one of three mined repository candidate media (with argillite and crystalline rocks), along with deep borehole disposal. The results of this ranking process (their Appendix B) took the FEPs that might be considered at a future radioactive waste disposal program and prioritized future research on topics supporting each FEPs relative to two factors: 1) impact to the overall disposal safety case and 2) the current state-of-the-art of knowledge about the topic. Salt-specific FEPs scored high on this ranked list, including the effects of brine flow processes in salt, effects of repository excavation on the salt host rock and the development of the disturbed rock zone (DRZ) around excavations in salt, dehydration of hydrous evaporite minerals, and the salt host rock's stratigraphy and properties (see gray FEPs in Table 1).

The UFD roadmap (UFD Campaign, 2012) discussed the importance of collaborating with existing international underground research laboratories (URLs) and mentioned the benefits of developing some URL capabilities domestically (their §4.2.7). The roadmap indicated the benefits of a URL included site-specific, concept-specific, and generic benefits, including:

- Supplement and focus site characterization efforts (site-specific URL);
- Repository system demonstration for system engineering, handling, emplacement, and licensing issues (concept-specific URL);
- Validation of conceptual and numerical models under relevant conditions (generic URL); and
- Provide generic information regarding a geology type that may be useful at future sites of the same geology (generic URL).

The work that has gone on in the DOE-NE Salt R&D program to implement a field test at WIPP has been motivated by the two generic URL aspects given above. Site-specific characterization, and concept-specific demonstration efforts are more relevant to DOE Office of Environmental Management (DOE-EM), the implementer of the WIPP site and mission. Two large-scale demonstrations were initially funded by DOE-EM to accomplish this. The work currently being funded by DOE-NE Salt R&D is generic (i.e., not site- or concept-specific) to validate conceptual, mathematical, and numerical models useful at possible future salt sites.

Table 1. Page 1 of ranked 2012 roadmap FEPs (UFD Campaign, 2012); salt FEPs gray

Rank	Index	FEP Title	Media	Score
1	2.2.01.01	Evolution of EDZ	Argillite	8
2	2.2.08.01	Flow Through the Host Rock	Salt	7.73
	2.2.08.02	Flow Through the Other Geologic Units (confining units, aquifers)	Salt	7.73
	2.2.08.06	Flow Through EDZ	Salt	7.73
3	2.2.08.04	Effects of Repository Excavation on Flow Through the Host Rock	Salt	7.1
4	2.2.08.07	Mineralogic Dehydration	Salt	6.49
5	2.2.01.01	Evolution of EDZ	Deep Borehole	6.13
6	2.2.09.01	Chemical Characteristics of Groundwater in Host Rock	Deep Borehole	5.86
	2.2.09.02	Chemical Characteristics of Groundwater in Other Geologic Units, Non-Host-Rock	Deep Borehole	5.86
	2.2.09.05	Radionuclide Speciation and Solubility in Host Rock	Deep Borehole	5.86
	2.2.09.06	Radionuclide Speciation and Solubility in Other Geologic Units, Non-Host-Rock	Deep Borehole	5.86
7	2.2.09.03	Chemical Interactions and Evolution of Groundwater in Host Rock	Deep Borehole	5.4
	2.2.09.04	Chemical Interactions and Evolution of Groundwater in Other Geologic Units	Deep Borehole	5.4
8	1.2.03.01	Seismic Activity Impacts EBS and/or EBS Components		4.94
9	2.1.09.13	Radionuclide Speciation and Solubility in EBS		4.86
10	2.1.03.02	General Corrosion of Waste Packages		4.34
	2.1.03.03	Stress Corrosion Cracking of Waste Packages		4.34
	2.1.03.04	Localized Corrosion of Waste Packages		4.34
	2.1.03.05	Hydride Cracking of Waste Packages		4.34
11	2.1.02.01	SNF Commercial, DOE Degradation (Alteration, Dissolution, Release)		4.01
12	2.2.07.01	Mechanical Effects on Host Rock	Salt	3.83
	2.2.07.01	Mechanical Effects on Host Rock	Argillite	3.83
13	2.2.02.01	Stratigraphy and Properties of Host Rock	Crystalline	3.74
	2.2.02.01	Stratigraphy and Properties of Host Rock	Deep Borehole	3.74
	2.2.02.01	Stratigraphy and Properties of Host Rock	Salt	3.74
	2.2.02.01	Stratigraphy and Properties of Host Rock	Argillite	3.74
⋮	⋮	⋮	⋮	⋮

A workshop was held in spring 2013 to propose tests to conduct during large-scale disposal demonstrations planned at WIPP (Sevougian et al., 2013 – discussed further in subsequent section). The report from this workshop included both a list of candidate field and laboratory tests proposed by the meeting participants and the following list of Salt R&D research priorities (for FY14 and follow-on years). This list of "FY14 and beyond" priorities from Sevougian et al. (2013) is reproduced here, with an additional column indicating the status of these different components in FY18 (Table 2).

Table 2. Status of FY14 Salt R&D priorities in FY18

FY14 Salt R&D Priorities (Sevougian et al., 2013)		FY18 Status
1)	Existing Salt Data Compilation and Assessment	Complete (Kuhlman et al. 2012; Kuhlman & Sevougian, 2013)
2)	Test Planning for Re-Entry into the North Experimental Area of WIPP	Investigation complete (Brady et al. 2014), project never pursued
3)	Laboratory studies	
	3a) Hot Granular Salt Consolidation, Constitutive Model and Micromechanics	Partially complete (Bauer & Urquhart 2014; Stormont et al., 2017)
	3b) Laboratory Interbed Shear Testing	Never pursued (DOE-EM now investigating: Sobolik, 2017)
	3d) Laboratory Thermomechanical Testing of Intact Salt	Never pursued
	3e) THMC Experiments to Study the Effect of Creep and Clay Interbeds on Permeability and Brine Migration in Salt at High Temperatures and Pressures	Never pursued
	3f) Study of Thermodynamic Properties of Brines, Minerals and Corrosion Products in High Temperature Systems	Never pursued
	3g) Radionuclide Solubility Measurements	Never pursued
4)	Modeling Studies related to Salt	
	4a) Safety Framework	Partially complete (Kuhlman & Sevougian, 2013); ongoing GRS/SNL FEP collaboration
	4b) Total System Performance Assessment (TSPA) Model Development	Ongoing GDSA integration
	4c) Generic Salt Repository Benchmarking – US/German Collaborative Effort	Ongoing GRS/SNL collaboration (REPOTREND vs. PFLOTRAN)
	4d) TMHC Model Development	Ongoing LBNL work related to field test
	4e) Brine Migration Modeling in Rock Salt	Ongoing LANL, LBNL & SNL work related to field test
5)	International collaboration	Ongoing
6)	Salt Instrumentation Development and Test Methodologies	Ongoing related to field test
7)	Thermal field testing	Ongoing related to field test

Several laboratory study testing priorities from FY14 (Table 2) were never pursued because they are of secondary importance to the development of a long-term safety case in salt, and they were either too risky or expensive for their level of safety case importance. Given the level of funding available for Salt R&D from FY14 to FY18 has not been high enough to pursue all these goals, the funding of specific research proposals is a balance between technical importance, technical risk, and implementation cost. Large laboratory or field experiments have higher cost and risk associated with them, so they must be planned carefully. Field experiments at WIPP must also work with the existing schedule, drivers, and regulations that apply there, which may not exist for laboratory or modeling exercises.

Sevougian et al. (2013) also mapped the FY14 and beyond Salt R&D Priorities (Table 2) to the list of salt FEPs to illustrate their connection to the future safety case for disposal of heat-generating waste in salt (see their Table 6-2), illustrating the possible importance of each test to operational and long-term disposal safety.

1.3 Recent DOE-NE Salt R&D Program Highlights

The Salt R&D program has included aspects of numerical modeling (both process modeling and PA modeling), laboratory testing, and field testing; recent highlights are mentioned from these areas.

Hansen & Leigh (2011) presented a review of salt repository science near the beginning of the DOE-NE Salt R&D program. They reviewed relevant history, stated the state-of-the-art in salt geomechanics, and presented a baseline list of FEPs that might be applied to a salt repository concept for heat-generating waste. Kuhlman & Malama (2013) presented an analogous history and state-of-the-art review but focused on brine migration aspects. Kuhlman (2014) summarized state-of-the-art in brine migration modeling efforts. Hansen et al. (2014) presented a state-of-the-art review focused on the topic of granular salt reconsolidation.

International collaboration has been an integral part of the Salt R&D program, with ongoing participation in the US/German Workshop on Salt Repository Research, Design, and Operation, now in its 9th year (e.g., Hansen et al., 2018; Hansen et al., 2017). Ongoing collaborations between Sandia and Gesellschaft für Anlagen- und Reaktorsicherheit (GRS) have included: development of salt FEPs, development of a salt knowledge archive, PFLOTRAN/d^{3}f regional groundwater flow comparisons, and PFLOTRAN vs. REPOTREND PA model benchmarking (all discussed in previous workshop proceedings).

The recent focus of the DOE-NE Salt R&D field testing program has been on brine availability in repository excavations in salt (Kuhlman et al. 2017a). Availability of brine includes the characterization of how much brine of each type is present in the evaporite formation, and the conditions under which this brine moves through excavation damage to an opening (i.e., a borehole or drift). The movement of brine through salt to excavations is controlled by the interaction of the excavation, the DRZ, and the drift-scale stratigraphy of the host rock. Geologic salt is impermeable without the overprint of fracturing and damage accumulation associated with excavations or the heterogeneity of more permeable and more brittle non-salt units (e.g., clay, anhydrite, polyhalite, carnallite) in evaporite formations. Migration of brine in a two-phase system is non-linear and depends on the state of the system, too (e.g., liquid and gas pressure, temperature, stress, liquid and brine saturation, and brine composition). Availability of brine is an important part of the safety case because it controls: waste package corrosion, transport of radionuclides, and can provide back-pressure to slow down creep closure of excavations.

The following sections discuss the previous and ongoing modeling and laboratory efforts as part of the Salt R&D program. The final subsections discuss the relevant history and future plans regarding the WIPP borehole heater test.

1.3.1 Performance Assessment (PA) Modeling

The DOE-NE Salt R&D program is generic by design (i.e., no candidate disposal site). Perry et al. (2014) presented nation-wide reconnaissance studies illustrating the range of salt repository sites possible, based solely on depth and presence of salt formations. Sandia has organized the Generic Disposal System Analysis (GDSA) program under DOE-NE which is conducting PA type analyses of generic reference cases, including ones for salt (Freeze et al. 2014; Sevougian et al., 2015; Stein et al., 2016), along with references cases for argillite, crystalline, and deep borehole disposal.

Although not their focus, salt has also been considered as one of several candidate disposal media in the dual-purpose canister (DPC) direct disposal DOE-NE research program (Hardin et al. 2013). Some PA modeling in a generic salt repository concept was completed as part of a project to consider DOE-Managed HLW and SNF wastes (Sevougian et al., 2016). Salt's already stated long-term disposal benefits means most generic salt disposal cases provide robust containment. The primary mechanism for release in the WIPP PA is through inadvertent human intrusions, which are not considered as part of the GDSA scenario development process.

1.3.2 Process Modeling

GDSA or PA modeling are focused on making predictions using large km-scale domains and long-term performance relevant time scales, while "process models" mean numerical modeling of physical processes across a range of temporal and spatial scales. PA modeling explicitly incorporates uncertainty into model predictions through systematic variation of uncertain parameters (e.g., Monte Carlo), and typically must approximate processes that are of second-order importance to long-term repository safety. Often process modeling is done to solve high-fidelity multi-physics problems to determine if they have impacts on long-term performance. If these impacts are significant, GDSA may need to integrate these processes or relationships into its numerical models. Process models are often used for formal FEP-screening arguments, which are not part of the primary PA or GDSA model. Process models would also be used to interpret validation data sets collected during field tests.

Numerical process model development has been conducted primarily at Los Alamos and Lawrence Berkeley (Kuhlman, 2014). Numerous salt-relevant improvements have been made to the thermal-hydrologic-chemical simulator, FEHM (e.g., Stauffer et al., 2013; Bourret et al., 2016; Johnson et al., 2018). Improvements have been made in TOUGH-FLAC to handle large deformation associated with excavations in salt, and dual-continuum approaches have been included to incorporate the migration and contribution of fluid inclusions in salt (Rutqvist et al., 2018).

Recent FEHM and TOUGH-FLAC modeling has been performed to predict the response of the borehole heater test at WIPP (Rutqvist et al., 2018; Johnson et al., 2018; Boukhalfa et al., 2018), and this has been used to design aspects of the test. These aspects of the validation modeling will continue as more data are collected and possible follow-on tests are designed.

1.3.3 Laboratory Studies

Laboratory investigations have included the most diverse topics and have been conducted across all three participating laboratories. Previous work included LANL fluid inclusion migration and hydrous mineral studies (Caporuscio et al., 2013; 2014) and SNL hot granular salt reconsolidation studies (Bauer & Urquhart, 2014). Stormont et al. (2017) performed work at SNL and the University of New Mexico on laboratory reconsolidation of granular salt, while characterizing the hydrologic and mechanical properties for different levels of compaction and temperatures. Kuhlman et al., (2017) summarized laboratory work on glass dissolution and partitioning of fission products into salt phases. Berkeley performed laboratory work related to geophysical instrumentation in previous field demonstration efforts (Stauffer et al., 2015). Laboratory work is now primarily focused on support of the field test, either through sample analyses or methods development efforts. Although these laboratory efforts are not significantly expensive or risky, they are being wound down to better focus resources and personnel on execution of the field test. The second section of this report discusses ongoing laboratory work to develop laboratory methods needed to analyze brine samples collected as part of the latest field test.

1.3.4 Recent Field Studies at WIPP

In the 1980s and 19990s there were several large-scale disposal demonstrations (e.g., Rooms A1-A3 & B) and scientifically motivated coupled processes interaction field tests (e.g., Rooms H & Q) conducted underground at WIPP (Kuhlman et al., 2012; Kuhlman & Sevougian, 2013). Among those, the heated tests were not for the current WIPP mission but were conducted to benefit another future salt site for disposal of defense high-level waste (initially the Deaf Smith site in Texas). More recently, there have been renewed efforts to perform both large-scale disposal demonstrations and more targeted small tests, relevant to heat-generating waste of different energy densities.

1.3.4.1 SDI and SDDI

The current DOE-NE Salt R&D program does not include a large-scale field-demonstration component, due to the program's generic mandate and the concept-specific and site-specific nature of drift-scale

demonstrations. DOE-NE is conducting laboratory and borehole-scale field studies of a generic nature. The two previously proposed DOE-EM drift-scale disposal demonstrations are discussed here, as they provide context for the current *in situ* field test campaign.

From 2011 to early 2014 DOE-EM Carlsbad Field Office (CBFO) planned to conduct a drift-scale disposal demonstration at WIPP. This work began with the Salt Disposal Investigations (SDI) concept, which was relevant to hotter radioactive waste (several kilowatts per canister) with canisters placed individually into an alcove-style disposal arrangement and backfilled for shielding (Figure 1; CBFO, 2011). This disposal demonstration was relevant to the DOE-NE mission of spent reactor fuel disposal but was less relevant to the DOE-EM defense high-level waste cleanup mission.

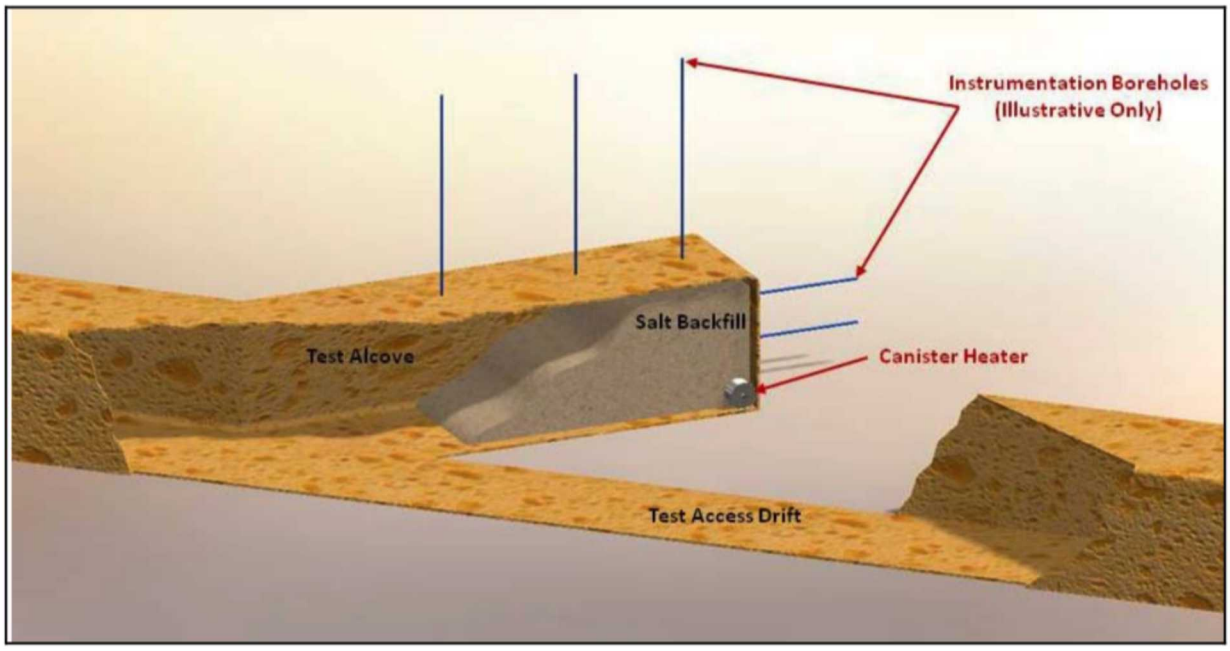

Figure 1. Salt Disposal Investigations (SDI) alcove disposal demonstration concept (CBFO, 2011)

Beginning in 2013, the disposal demonstration plan was modified from SDI to the Salt Defense Disposal Investigations (SDDI) to focus on closely spaced in-drift disposal of cooler (few hundreds of watts per canister) waste (Figure 2; CBFO, 2013). The cooler "defense" waste was more relevant to the DOE-EM defense high-level waste cleanup mission than the DOE-NE spent reactor fuel mission.

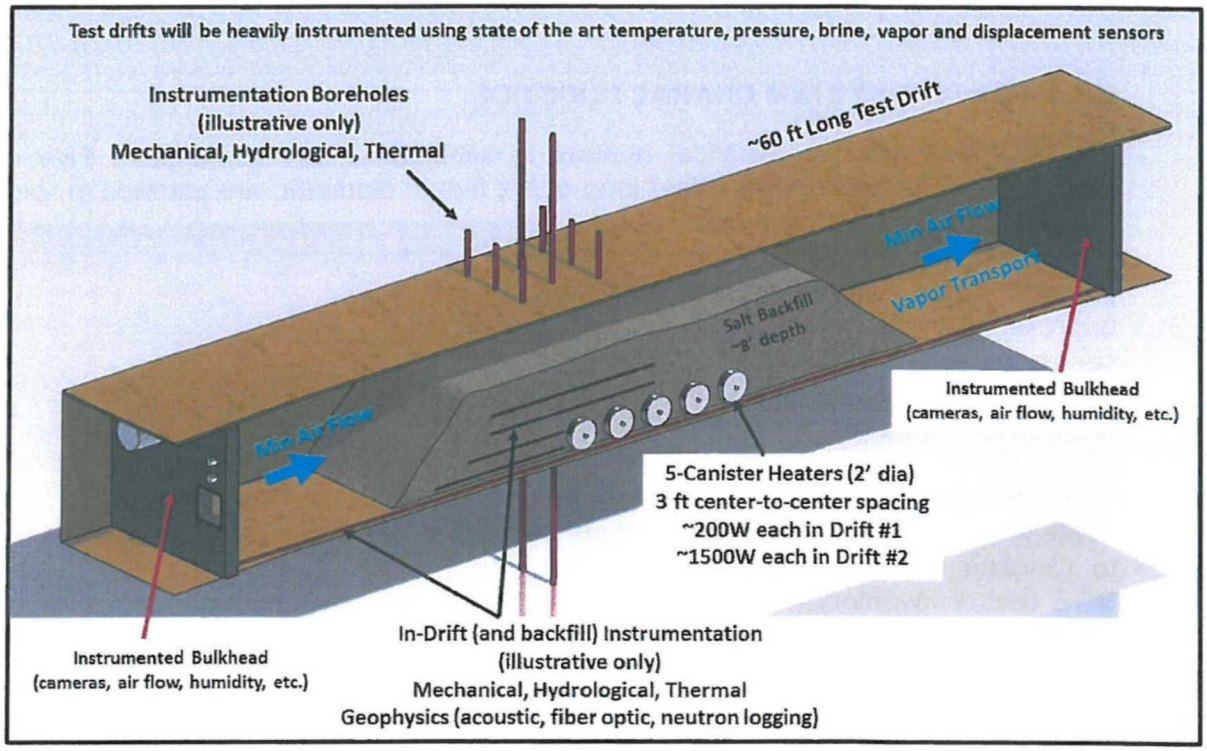

Figure 2. Salt Defense Disposal Investigations (SDDI) in-drift disposal demonstration concept (CBFO, 2013)

To execute these demonstrations, a new experimental area was mined south of Rooms A and B at WIPP in the same stratigraphic level as the disposal rooms, rather than the elevated level of the old north experimental area (see two mine levels in Figure 3 and Figure 9 of next section). This new experimental area is referred to as the "SDI area" on WIPP maps (see WIPP layout in Figure 10 of next section).

Both of these disposal demonstrations (SDI and SDDI) focused on observations of the near-field (e.g., evolution of humidity in granular salt and room closure around waste packages) and at early time (i.e., during controlled ventilation) repository evolution, which are primarily important for process modeling and as "initial conditions" for PA/GSDA models of repository long-term performance.

1.3.4.2 WIPP Experimental Area Re-entry Proposal

As part of DOE-NE's contribution to the DOE-EM large-scale disposal demonstrations, Sandia performed a review of the historic tests and a catalog of the field experiments done at WIPP (i.e., items 1 and 2 in Table 2). This investigation focused on enumerating the experiments from the 1980s and 1990s that were left in place (Brady et al. 2014). Based on these investigations, preliminary re-entry plans were made to either enter old experimental rooms or core samples from proposed adjacent rooms to obtain salt and canister samples with decades of exposure times at ambient conditions (Figure 3).

These re-entry activities were never executed, due to their significant operational cost and their unknown contribution to the safety case. The condition of the canisters, sensors, and experiments is unknown, and it is unclear what would be learned from them, without a significant re-investigation effort. Although these experiments present a unique opportunity, they are also a significant unknown.

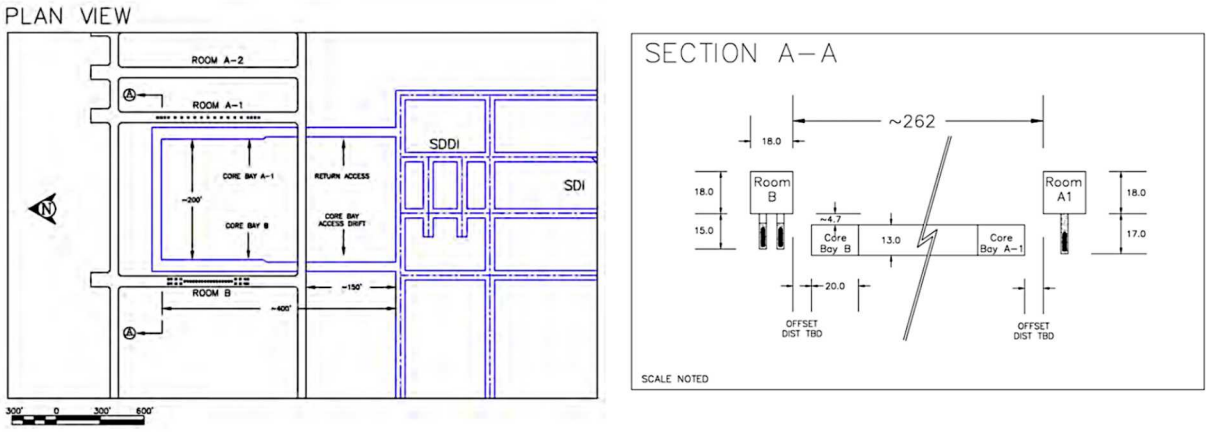

Figure 3. Proposed re-entry to WIPP Rooms A & B (Brady et al., 2014; Sevougian et al. 2013)

1.3.4.3 2013 Salt Field Test Workshop

During the planning and development of SDDI by DOE-EM, DOE-NE convened a workshop in Albuquerque (March 6-7, 2013) titled *"Advancing the Science and Engineering Supporting Deep Geologic Disposal of Nuclear Waste in Salt."* At this workshop staff from participating US national laboratories discussed how generic Salt R&D could be executed to compliment and coexist with the large-scale disposal demonstrations being planned at WIPP (Sevougian et al. 2013). Building upon the UFD roadmap, this workshop formulated an expert consensus on the relative importance of various field test safety case issues and put forth recommendations for R&D activities to address them, including modeling studies, laboratory studies, and smaller-scale field testing (Table 3).

Recommendations about the R&D field testing, laboratory testing, and modeling activities to pursue were based on their expected relevance to the objectives and goals of a safety case for a generic bedded salt repository, as well as their ability to help resolve remaining uncertainties associated with the technical issues they are designed to address. The workshop included a re-examination of the motivation and ranking of different repository-relevant processes, building on the 2011 roadmap exercise (UFD Campaign, 2012).

Table 3. Tests proposed at 2013 workshop (Sevougian et al., 2013; Table 7-3); aspects of current testing program in gray

ID	Name	Type	Principal Investigators
Primarily in situ, large-scale field testing (with modeling)			
H-1	Clay seam shear test	In situ tests in the new URL; Laboratory tests; Constitutive modeling; International collaborations	Frank Hansen (SNL)
H-2	Single heater test	Generic in situ tests in the new URL; International collaborations; Modeling prediction and validation	Frank Hansen (SNL), Carlos Jove-Colon (SNL)
H-3	Large-scale seal test	In situ tests in the new URL; International collaborations; Modeling; Lab - ACI concrete testing	Frank Hansen (SNL)
H-4	Salt defense disposal investigations (SDDI) thermal test	In situ thermal test; Laboratory tests; THM and THMC model validation	Doug Weaver (LANL)
H-5	Water migration tracer test during the proposed SDDI experiment	In situ field test with lab analysis; including pre-, during, and post-test transport modeling	Philip Stauffer (LANL), Florie Caporuscio (LANL), Paul Reimus (LANL), Ernie Hardin (SNL)
Laboratory testing followed by in situ testing (with modeling)			
H-6	Salt decrepitation effects	Laboratory tests initially; borehole & in situ field testing later; THM process and constitutive modeling	Kris Kuhlman (SNL)
H-7	Development of an integrated geophysical imaging system for field-scale monitoring of brine migration and mechanical alteration in salt repositories	Laboratory tests; Field testing at LBNL Geophysical Measurement Facility (GMF); (no modeling initially but later some pre-test modeling)	T.M. Daley, Y. Wu, J. Birkholzer, and J.B. Ajo- Franklin (LBNL)
Laboratory testing followed by in situ testing (no modeling)			
H-8	Geophysical and acoustical monitoring of fluid migration and fracture evolution for WIPP salt thermal tests	Initial lab sensitivity experiments; followed by in situ field tests at WIPP during SDDI thermal tests (no modeling)	Peter Roberts (LANL)
H-9	In situ and laboratory testing of moisture monitoring methods	Laboratory tests; In situ field tests (no simulation modeling mentioned)	Dan Levitt (LANL)
Laboratory testing (with modeling)			
H-10	THMC experiments to study the effect of creep and clay on permeability and brine migration in salt at high temperatures and pressures	Complex THMC laboratory experiments; coupled process modeling to predict/interpret the results	Tim Kneafsey and Seiji Nakagawa (LBNL)
Laboratory testing (no modeling)			
H-11	Long-term steel corrosion analyses from Room A1/B re-entry	Laboratory test; (no simulation modeling mentioned)	Pat Brady (SNL)
H-12	Imaging brine migration in salt using neutron and synchrotron X-ray Tomography	Laboratory tests (no simulation modeling)	Hongwu Xu (LANL), Jonathan Ajo-Franklin (LBL)
H-13	Validation of constitutive models and parameterization of unsaturated brine flow in intact and crushed salt	Laboratory test (no simulation modeling)	Kris Kuhlman (SNL); Bwalya Malama (SNL)
H-14	Stability of polyhalite in the Salado Formation	Laboratory test (no simulation modeling)	Florie Caporuscio (LANL)

ID	Name	Type	Principal Investigators
H-15	Stability of hydrous phases (corrensite, bassanite) in the Salado Formation	Laboratory test (applicable for SDDI waste emplacement studies)— (no simulation modeling)	Florie Caporuscio (LANL)
H-16	Use of ultra-low field (ULF) nuclear magnetic resonance (NMR) and magnetic resonance imaging (MRI)) to map and quantify brine content in an undisturbed salt core.	Laboratory test (no simulation modeling)	Florie Caporuscio (LANL)
H-17	Elevated-temperature measurements of Pu-III and Nd-III solubility in low to moderate ionic strength aqueous Solutions	Laboratory tests (no modeling)	Jonathan Icenhower and David Shuh (LBNL); Donald Reed (LANL)
H-18	Laboratory study on the long-term porosity and permeability reduction in salt backfill under elevated temperature conditions	Laboratory tests (no modeling)	Tim Kneafsey and Seiji Nakagawa (LBNL)
Modeling and simulation studies only (no physical tests)			
H-19	Mechanistic modeling of brine and vapor movement	Theoretical and modeling study	Qinjun Kang (LANL)
H-20	THM optimization of preclosure repository design	Coupled process modeling	Jonny Rutqvist and Laura Blanco-Martin (LBNL); Phil Stauffer and Florie Caporuscio (LANL)
H-21	Benchmarking simulations for THM behavior of rock salt	THM(C) benchmark modeling - model-to model comparisons for a simplified repository, for a lab/field THM experiment; and for the planned SDDI test	Jonny Rutqvist and Jens Birkholzer (LBNL); Phil Stauffer and Bruce Robinson (LANL); Carlos Jove-Colon, Kristopher Kuhlman, and Ernest Hardin (SNL)
H-22	THM model of salt rock microstructural damage and healing	Mechanistic microstructure modeling of coupled processes in salt	Daisuke Asahina and Jim Houseworth (LBNL)
H-23	Brine migration in salt: Review and constitutive model development	Constitutive models	Jim Houseworth, Jonny Rutqvist, Hui-Hai Liu, Jens Birkholzer (LBNL)
Proposals from researchers not present at the workshop			
H-24	Validation experiments using a geocentrifuge to examine canister movement in a salt repository	Lab testing	Earl D. Mattson, Mitchell A. Plummer (INL)

The shaded rows in Table 3 indicate proposed tests that are at least partially aligned with the current DOE-NE borehole heater test at WIPP. The current test is similar to the proposed "Single Heater Test" (H-2), and includes aspects of the "Water Migration Tracer Test" (H-5), "Integrated Geophysical Imaging System" (H-7), "Geophysical and Acoustical monitoring" (H-8), "Stability of Hydrous Phases" (H-14 and H-15), "Mechanistic Modeling of Brine and Vapor Movement" (H-19), "Benchmarking THM Simulations" (H-21), and "Brine Migration in Salt: Review and Constitutive Model Development" (H-23). The original authors' descriptions of each proposed test from this table comprise Appendix H of Sevougian et al. (2013).

These tests were contributed by a group of researchers from several national laboratories, and many of the proposed tests are inspired by or build upon concepts explored in various historical *in situ* tests in salt (Kuhlman & Sevougian, 2013; Kuhlman et al., 2017a). Several of the proposed experiments listed in Table 3 were never pursued and may never be pursued, since this aspect of the workshop was a "brainstorming" exercise. Many of these ideas have never gotten past a concept or proposal, because they

represent too much cost or risk, for the perceived benefit to the salt long-term disposal safety case, but this concept-generating exercise was fruitful.

In 2014, work funded by DOE-EM related to the large-scale disposal demonstrations at WIPP (SDI and SDDI) was stopped. Work funded by DOE-NE on laboratory experiments, numerical modeling, and generic small-scale testing has continued, but by FY17 the program has focused laboratory and modeling efforts to those supporting field testing.

1.3.4.4 FY17 and FY18 Field Test Planning

Although aspects of the field test planning have been ongoing for several years (e.g., Stauffer et al., 2015), work towards the current field test began in earnest in FY17. The DOE-NE Salt R&D and Salt International programs have been planning and implementing a heated coupled-process and brine-availability test at WIPP (e.g., Kuhlman et al., 2017a; Johnson et al., 2017; SNL et al. 2018; Johnson et al. 2018). Beginning in summer 2018, the DOE-NE SFWST program is executing a preliminary equipment and procedural "shakedown" borehole heater test in existing boreholes at WIPP (Figure 4) as the first stage of the planned heater test program (Boukhalfa et al., 2018).

Figure 4. Existing boreholes at WIPP (at E-140/N-1050) used in summer FY18 shakedown tests

Multiple brine availability tests (at least one heated and one ambient) will be started in late 2018 (FY19) in drilled-for-purpose boreholes at WIPP. Figure 5 shows the components of the test in the central borehole. These boreholes and the instrumentation installed in them include modifications and lessons learned from the equipment shakedown test implemented in the existing boreholes. The testing program includes parallel tests, in similar sets of heated and unheated boreholes to investigate the impacts temperature have on brine availability. The main borehole includes a packer and heater, with moisture inflow measured using a dry nitrogen extraction system (Kuhlman et al. 2017a).

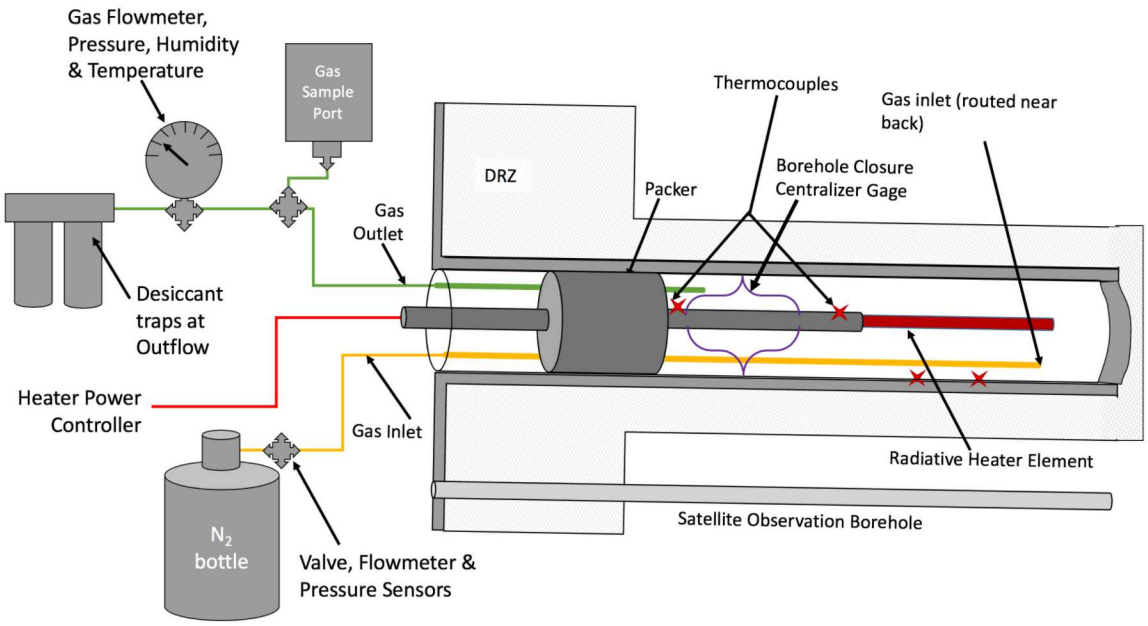

Figure 5. Schematic cross-sectional view of central borehole components in heated test at WIPP

Borehole closure will be monitored in the central borehole, and the permeability of the test interval will be monitored by falling-head gas permeability testing behind the packer (i.e., before, during and after heating). Gas compositional samples will be collected in the central borehole during the test to monitor any gases produced from the salt, including analyses on the stable isotopes of water.

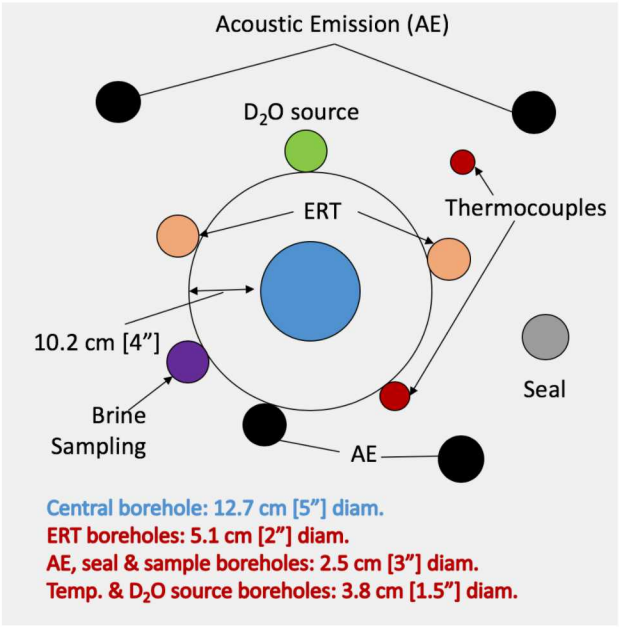

Figure 6. Schematic drift view of satellite observation boreholes and central borehole

Figure 6 conceptually shows the planned satellite boreholes positioned around the central borehole. These boreholes will be isolated from the access drift mine ventilation by plugs and include:

- Tracer source of deuterated water (D_2O) to be monitored in liquid water condensed from gas samples collected in the main borehole;
- Liquid brine samples collected before, during, and after heating to be analyzed for brine composition changes associated with the three sources of brine in salt (i.e., intergranular, intragranular, and hydrous minerals);
- Thermocouple boreholes to observe the temperature distribution along two boreholes at different radial distances from the heated borehole;
- Acoustic emissions (AE) observation boreholes, for passively observing the timing and estimating the location of acoustic emissions related to the heating of the borehole and associated creep or damage accumulation (i.e., porosity and permeability increase);
- Electrical resistivity tomography (ERT) source/sensor boreholes to conduct 3D ERT surveys before, during, and after heating to estimate changes in the distribution of brine and porosity surrounding the heated borehole; and
- Cement sealing test, including installation of a laboratory-constructed instrumented cement plug to observe impacts of brine and temperature on salt/cement seal development.

Geological, compositional, and microstructural analyses will be made on salt samples from cores collected during construction of the boreholes, from solid salts precipitated in the heated borehole, and from post-test cores collected after the end of the test. These analyses will include estimation of water and mineral content, observation of fluid inclusions, and microstructural analysis of dislocations and sub-grains in salt.

The evolving design of the current *in situ* test is presented in more detail other recent DOE-NE Salt R&D reports (Kuhlman et al. 2017a; Johnson et al., 2017; Boukhalfa et al., 2018). The interpretation and assessment of the data collected during this test will provide opportunity to confirm, validate, and modify numerical and constitutive models to better represent processes in salt.

1.4 Salt R&D Program Future Direction

The research priorities of the Salt R&D program started from the identified priority FEPs from the UFD 2012 roadmap (UFD Campaign, 2012) and the 2013 workshop (Sevougian et al., 2013). Some tasks identified in these reports have been completed, some were never pursued, while the ones discussed in the previous section continue to be investigated (Table 2). Related to GDSA integration (i.e., the incorporation of ongoing process model advances into PA models), several new priorities have arisen.

1.4.1 GDSA Integration

A focus of the SFWST program in general is integration of research performed under each individual work package into the GDSA framework, which is primary centered around PFLOTRAN. Even though Salt R&D's focus is on field testing, GDSA integration remains a secondary priority, especially when the incorporation of process model advances into GDSA can simultaneously support interpretation of field test results.

The GDSA integration focus includes uncertainty quantification with process models and strategies for both "tight" and "loose" coupling of processes with PFLOTRAN. Tight coupling here means direct implementation of a feature in PFLOTRAN, or iterative coupling of a numerical model with PFLOTRAN at each time step of a simulation. Loose coupling here means a more indirect method for including the effects of a process into GDSA models, like look-up-tables, reduced-order-models, or even setting parameters and initial conditions for PFLOTRAN based on the output of other, more complex and less compatible models. It is typically more physically realistic, but more computationally expensive, to include physical processes in large-scale simulations through some manner of tight coupling. Ideally, any

use of approximate loose coupling would be compared to analogous predictions made with tight coupling, to ensure the results are representative and physically realistic under the desired conditions.

Beyond the goals of the Salt R&D project from the original roadmap (Table 1) and those specified in FY14 (Table 2), several additional processes or behaviors are listed that could be integrated into PA/GDSA modeling. Some of these capabilities are already available in noted process models:

- Pitzer or specific ion interaction theory (SIT) model for activity coefficients at high ionic strength allowing process models to consider full chemistry (i.e., all observed ionic species) in evaporites. This would be directly implemented in PFLTORAN; it is currently done either with EQ3/6 or TOUGH-REACT.
- Consider physical thermal-hydrologic-chemical (THC) effects of dense, saline brines (e.g., impacts of salinity on vapor pressure, capillarity changes during significant porosity changes, and non-linear thermal conductivity) into GDSA models. This would be directly implemented in PFLTORAN; some of these capabilities are currently implemented in FEHM.
- Consider high-temperature environments above brine boiling point (e.g., around hot waste canisters with dry-out and heat pipes) in GDSA models while treating full chemistry. This would be directly implemented in PFLTORAN; some of these capabilities are currently implemented in TOUGH-REACT and FEHM.
- Incorporation of thermal-hydrological-mechanical (THM) coupled processes or THM predictions into GDSA models. It is well known that permeability and porosity in salt is related to excavation-induced damage. Time-dependent hydrologic properties should be explicitly linked to damage evolution in an appropriate geomechanical model. This either would involve a significant effort to implement these features into PFLOTRAN (i.e., large-deformation capabilities and viscoplastic constitutive models would be needed), or a loose coupling of the output of an existing THM code like TOUGH-FLAC into the initial conditions or parameters of PFLOTRAN.
- Validation of existing process models in GDSA, with implementation of new process models as needed (some of these processes given in previous bullets), to explain field data collected from borehole heater tests.

These are mostly GDSA modeling integration efforts, that may also be useful for interpreting aspects of the data collected during the field test. The field test data will provide a physically relevant validation data set for checking if implemented processes are correct, and to show the processes are physically important under relevant conditions. Numerical model prediction of field observations is a complex and iterative process, requiring close work between those collecting the data and those developing the numerical models. Uncertainty quantification and parameter estimation methods from GDSA can be applied to the process of matching validation observations from the field tests.

1.4.2 Summary and Future

In summary, the ranking of FEPs during the initial UFD roadmap exercise (UFD Campaign, 2012) indicated salt-relevant FEPs are both important to the safety case and require additional study. These FEPs are strongly related to the current focus of the current field heater test exercise (Table 1). The study areas listed during the 2013 workshop (Sevougian et al., 2013; Table 2) included several laboratory studies that have not been pursued but are otherwise well-aligned with the current field heater test exercise. Most of the tests proposed during the workshop (Table 3) were never executed, but aspects of several of them exist in the current ongoing heater test. The never-executed laboratory studies and field tests have been considered to be of secondary importance towards the long-term safety case for disposal of heat-generating waste in salt. These tests also had higher risks or costs associated with their execution that were not commensurate with their potential resulting benefit to the safety case. Because of this

situation, several of these laboratory and field tests that were not executed as they received a low priority for implementation within existing budgets.

The generic research that has been conducted under the Salt R&D program during the life of the UFD and SFWST programs so far has contributed to the long-term safety case for disposal of heat generating waste in salt. THC and THM process models have seen improvements that allow more physically realistic simulations of the complex drift-scale and early-time behavior in excavations in salt. Recent geomechanical laboratory experiments and international collaborations have improved understanding of bedded salt, and salt in general (e.g., granular salt reconsolidation and creep at low deviatoric stress). International collaborations have continued, which have allowed the DOE-NE program to benefit from ongoing research in Germany, the United Kingdom, and the Netherlands. The brine availability experiments now being conducted will allow the DOE-NE program to directly contribute back to these international partners with validation datasets and improved understanding on brine migration away from clay or anhydrite layers near excavations in bedded salt.

In FY19 the Salt R&D program looks forward to two primary goals: execution of the brine availability field test at WIPP and several GDSA integration activities. These integration activities would benefit both the GDSA program and also assist in the interpretation of results collected during the WIPP heater test. Although there has been some shift in implementation focus for the Salt R&D program away from more substantial laboratory activities, the focus remains on producing R&D relevant to bolstering the generic safety case for disposal of heat-generating waste in salt.

1.5 References

Bauer, S.J. & A. Urquhart, 2014. *Thermophysical Properties of Reconsolidating Crushed Salt*. SAND2014-2240, Sandia National Laboratories, Albuquerque, NM.

Beauheim, R.L. & R.M. Roberts, 2002. Hydrology and hydraulic properties of a bedded evaporite formation, *Journal of Hydrology, 259*(1-4):66-68.

Boukhalfa, H., P.J. Johnson, D. Ware, D.J. Weaver, S. Otto, B.L. Dozier, P.H. Stauffer, M.M. Mills, E.N. Matteo, C.G. Herrick, M.B. Nemer, K.L. Kuhlman, Y. Wu & J. Rutqvist, 2018. *Implementation of a Small Borehole Heater Test at WIPP*. M3SF-18LA010303014, Los Alamos National Laboratory.

Bourret, S.M., P.J. Johnson, G.A. Zyvoloski, S.P. Chu, D.J. Weaver, S. Otto, H. Boukhalfa, F.A. Caporuscio, A.B Jordan, P.H. Stauffer, 2016. *Experiments and Modeling in Support of Generic Salt Repository Science*. FCRD-UFD-2016-000445, LA-UR-16-27329.

Brady, P.V., C.G. Herrick, K.L. Kuhlman, B. Malama, M.D. Schuhen & B.A. Stenson, 2014. *Sandia Experimental Programs Background and Proposed Activities for Forensic Investigation of Rooms B and A1*. ERMS 561663, Carlsbad, NM: Sandia National Laboratories.

Caporuscio, F.A., H. Boukhalfa, M.C. Cheshire, A.B. Jordan & M. Ding, 2013. *Brine Migration Experimental Studies for Salt Repositories*. LA-UR-13-27240, Los Alamos National Laboratory, Los Alamos, NM.

Caporuscio, F.A., H. Boukhalfa, M.C. Cheshire & M. Ding, 2014. *Brine Migration Experimental Studies for Salt Repositories*. LA-UR-26603, Los Alamos National Laboratory, Los Alamos, NM.

Carlsbad Field Office (CBFO), 2011. *A Management Proposal for Salt Disposal Investigations with a Field Scale Heater Test at WIPP*, DOE/CBFO-11-3740, Revision 0, US Department of Energy Office of Environmental Management, Carlsbad Field Office.

Carlsbad Field Office (CBFO), 2013. *Test Specification for the Salt Defense Disposal Investigations Thermal Test in WIPP*, DOE/CBFO-13-3510, Revision 0, US Department of Energy Office of Environmental Management, Carlsbad Field Office.

Freeze, G.A., W.P. Gardner, P. Vaughn, S.D. Sevougian, P. Mariner, V. Mousseau & G. Hammond, 2013. *Enhancements to Generic Disposal System Modeling Capabilities*, FCRD-UFD-2014-000062, SAND2013-10532P, Albuquerque, NM: Sandia National Laboratories.

Hansen, F.D. & C.D. Leigh, 2011. *Salt Disposal of Heat-Generating Nuclear Waste*, SAND2011-0161, Albuquerque, NM: Sandia National Laboratories.

Hansen, F.D., T. Popp, K. Wieczorek & D. Stuhrenberg, 2014. *Granular Salt Summary: Reconsolidation Principles and Applications*. FCRD-UFD-2014-000590, SAND2014-16141R.

Hansen, F.D., W. Steininger & W. Bollingerfehr, 2017. *Proceedings of the 7th US/German Workshop on Salt Repository Research, Design, and Operation*. SFWD-SFWST-2017-000008, SAND2017-1057R.

Hansen, F.D., W. Steininger, W. Bollingerfehr, K.L. Kuhlman & S. Dunagan, 2018. *Proceedings of the 8th US/German Workshop on Salt Repository Research, Design, and Operation*. SFWD-SFWST-2018-000485, SAND2018-1339R.

Hardin, E.L., D.J. Clayton, R.L. Howard, J.M. Scaglione, E. Pierce, K. Banerjee, M.D. Voegele, H.R. Greenberg, J. Wen, T.A. Bushcheck, J.T. Carter, T. Severynse & W.M. Nutt, 2013. *Preliminary Report on Dual-Purpose Canister Disposal Alternatives (FY13)*, FCRD-UFD-2013-000171 Rev. 1, SAND2013-10068P.

Hess, H.H., J.N. Adkins, W.B. Heroy, W.E. Benson, M.K. Hubbert, J.C. Frye, R.J. Russell & C.V. Theis, 1957. *The Disposal of Radioactive Waste on Land*. Publication 519, Report of the Committee on Waste Disposal of the Division of Earth Sciences, National Academy of Sciences.

Johnson P.J., Boukhalfa H., Weaver D.J., Otto S., Dozier B.L., Stauffer P.H., Mills M.M., Matteo E.N., Kuhlman K.L., Rutqvist J., & Wu Y, 2017. *Test Plan Document for Thermal Testing in Salt Test Plan*, TP-18-001-REVISION 0LA-UR-17-30762, DMS-SFWD-SFWST-2017-000043.

Kuhlman, K.L., S. Wagner, D. Kicker, R. Kirkes, C. Herrick & D. Guerin, 2012. *Review and Evaluation of Salt R&D Data for Disposal of Nuclear Waste in Salt*, FCRD-UFD-2012-000380, SAND2012-8808P.

Kuhlman, K.L., 2013. Historic testing relevant to disposal of heat-generating waste in salt, *American Nuclear Society Radwaste Solutions*, 20(4):22–28.

Kuhlman, K.L., 2014. *Summary Results for Brine Migration Modeling Performed by LANL, LBNL, and SNL for the UFD Program*. FCRD-UFD-2014-000071, SAND2014-18217R, Albuquerque, NM: Sandia National Laboratories.

Kuhlman, K.L. & B. Malama, 2013. *Brine Flow in Heated Geologic Salt*, SAND2013-1944, Albuquerque, NM: Sandia National Laboratories.

Kuhlman, K.L. & S.D. Sevougian, 2013. *Establishing the Technical Basis for Disposal of Heat-Generating Waste in Salt*, FCRD-UFD-2013-000233, SAND2013-6212P.

Kuhlman, K.L., M.M. Mills & E.N. Matteo, 2017a. *Consensus on Intermediate Scale Salt Field Test Design*, SFWD-SFWST-2017-000099, SAND2017-3179R. Albuquerque, NM: Sandia National Laboratories.

Kuhlman, K.L., E.N. Matteo, T. Hadgu, B. Reedlunn, S.R. Sobolik, M.M. Mills, L.D. Kirkes, Y. Xiong & J.P. Icenhower, 2017b. *Status Report on Laboratory Testing and International Collaborations in Salt*, SFWD-SFWST-2017-000100. Albuquerque, NM: Sandia National Laboratories.

Nuclear Energy Agency (NEA), 2014. *Natural Analogues for Safety Cases of Repositories in Rock Salt*, NEA/RWM/R(2013)10. Nuclear Energy Agency Organisation for Economic Co-Operation and Development.

Nuclear Energy Agency (NEA), 2018. *Microbial Influence on the Performance of Subsurface, Salt-Based Radioactive Waste Repositories*, NEA No. 7378. Nuclear Energy Agency Organisation for Economic Co-Operation and Development.

Perry, F.V., R.E. Kelley, P.F. Dobson & J.E. Houseworth, 2014. *Regional Geology: A GIS Database for Alternative Host Rocks and Potential Siting Guidelines*, FCRD-UFD-2013-000068, LA-UR-14-20368.

Rutqvist, J., M. Hu, Y. Wu, L. Blanco-Martin, J. Birkholzer, 2018. *Salt Coupled THMC Processes Research Activities at LBNL: FY2018 Progress*. LBNL-2001170. Berkeley, CA: Lawrence Berkeley National Laboratory/.

Sandia National Laboratories (SNL), Los Alamos National Laboratory (LANL) & Lawrence Berkeley National Laboratory (LBNL), 2018. *Project Plan: Salt in situ Heater Test*, SAND2018-4673R.

Sevougian, S.D., R.J. MacKinnon, B.A. Robinson, C.D. Leigh & D.J. Weaver, 2013. *RD&D Study Plan for Advancement of Science and Engineering Supporting Geologic Disposal in Bedded Salt – March 2013 Workshop Outcomes*. FCRD-UFD-2013-000161, Rev. 0, SAND2013-4386P.

Sevougian, S.D., G.A. Freeze, W.P. Gardner, G.E. Hammond, P.E. Mariner, R.J. MacKinnon, 2015. *Performance Assessment Modeling of a Generic SNF/HLW Repository in Salt with Coupled Thermal-Hydrologic Effects – 15423*. Waste Management Conference, Phoenix Arizona.

Sevougian, S.D., E.R. Stein, M.B. Gross, G.E. Hammond, J.M. Frederick, P.E. Mariner, 2016. *Status of Progress Made Towards Safety Analysis and Technical Site Evaluations for DOE Managed HLW and SNF*. FCRD-UFD-2016-000082 Rev 1, SAND2016-11232R.

Serata, S. & E.F. Gloyna, 1959. *Development of Design Principle for Disposal of Reactor Fuel Waste into Underground Salt Cavities*, Atomic Energy Commission.

Sobolik, S., 2017. *Experimental Investigation of WIPP Salt Samples and Clay Seams.* Waste Isolation Pilot Plant Test Plan TP 17-03, Carlsbad, NM: Sandia National Laboratories.

Stauffer, P.H., D.R. Harp, A.B. Jordan, Z. Lu, S. Kelkar, Q. Kang, J. Ten Cate, H. Boukhalfa, Y. Labyed, P.W. Reimus, F.A. Caporuscio, T.A. Miller & B.A. Robinson, 2013. *Coupled Model for Heat and Water Transport in a High Level Waste Repository in Salt*. FCRD-UFD- 2013-000206, LA-UR-13-27584.

Stauffer, P.H., A.B. Jordan, D.J. Weaver, F.A. Caporuscio, J.A. Ten Cate, H. Boukhalfa, B.A. Robinson, D.C. Sassani, K.L. Kuhlman, E.L. Hardin, S.D. Sevougian, R.J. MacKinnon, Y. Wu, T.A. Daley, B.M. Freifeld, P.J. Cook, J. Rutqvist & J.T. Birkholzer, 2015. *Test Proposal Document for Phased Field Thermal Testing in Salt*. FCRD-UFD- 2015-000077, LA-UR-15-23154.

Stein, E.R., S.D. Sevougian, G.E. Hammond, J.M. Frederick & P.E. Mariner, 2016. *Performance Assessment of a Generic Repository in Bedded Salt*. MR41C-2711, SAND2016-12457C, American Geophysical Union Fall Meeting, San Francisco, California.

Stormont, J.C., B. Lampe, M. Mills, L. Paneru, T. Lynn & A. Piya, 2017. *Improving the Understanding of the Coupled Thermal-Mechanical-Hydrologic Behavior of Consolidating Granular Salt*. NEUP 13-4384, Fuel Cycle Research and Development.

UFD Campaign (Used Fuel Disposition Campaign), 2012. *Used Fuel Disposition Campaign Disposal Research and Development Roadmap*, FCR&D-USED-2011-000065 Rev 1.

2. Brine Composition Modeling and Evaporation Experiments

Authors: Carlos M. Lopez, Melissa M. Mills, and Kristopher L. Kuhlman

A primary goal of the ongoing borehole heater tests at WIPP is characterization of brine availability, specifically quantifying the brine available to excavations that do not intersect mapped clay seams or marker beds, and its availability as a function of temperature (Kuhlman et al. 2017; Johnson et al. 2017; SNL et al., 2018; Boukhalfa et al., 2018). Liquid brine will be sampled from boreholes, and brine composition will be monitored through time through parallel unheated and heated experiments.

This section presents preliminary results of ongoing laboratory experimental work and EQ3/6 brine composition modeling as part of the Salt R&D heater test. This laboratory effort is developing and improving analytical methods for analyzing brines and solids collected before, during and after the upcoming heater test. The modeling effort is developing comprehension regarding brine composition and evolution and assembling the modeling tools and approaches needed to interpret the brine and precipitant composition data that will be collected during the heater test.

2.1 Background and Motivation

The borehole heater test at WIPP will sample brine produced from the salt under both unheated and heated conditions. Water comes from three primary sources from within the salt:

1. brine between grains in pores (intergranular brine);
2. fluid inclusions (intragranular brine); and
3. hydrous minerals (e.g., clay, gypsum, epsomite or polyhalite).

One of the objectives of the heater test is to attempt to discern the contributions from these brine sources through time at different temperatures. The three brine sources produce water under different conditions and due to different driving forces, illustrated as follows:

- Intergranular brine exists in a connected pore network near excavations and can move due to a pressure gradient. Water can evaporate into mine ventilation air and move in the vapor phase. Both brine and vapor can move in response to applied temperature (i.e., pressure increase from thermal expansion).
- Fluid inclusions cannot move under fluid pressure gradients and typically only move under temperature gradients (away or towards the heat source depending on their gas content). Fluid inclusions will be liberated at the decrepitation point (~250 °C). When fluid inclusions move to grain boundaries or are liberated through decrepitation, they can then flow to the borehole through the intergranular pore network (see previous bullet).
- Water of hydration cannot move under pressure gradients and is only liberated when minerals are heated above their dehydration temperature. This water is given off as steam, which can move through the intergranular porosity as vapor. Depending on the salt temperature, the vapor can condense and dissolve salt to create a brine that can flow to the borehole through the intergranular pore network (see first bullet).

Fluid inclusions and hydrous minerals can act as spatially distributed sources for additional intergranular brine, depending on the conditions. Given the complex spatial and temporal response of these different brine sources to temperature, temperature gradient, mine ventilation humidity, and fluid pressure, the goal of this work is to discern whether these three water sources can be differentiated compositionally.

In the field test, the brine collected in sampling boreholes (Figure 6 of previous section) may flow to the borehole from multiple simultaneous sources, may include brine created from dissolution of salt through deliquescence, and will include dehydration of the brine in the borehole through the vapor extraction

system. The geochemical simulator EQ3/6 is being used to predict the evolution of brine, predict the precipitant expected in the heated borehole, and better understand the contributions from each of the possible brine components present in the salt.

The laboratory experiments presented here provide validation datasets for compositional modeling of relevant brines under controlled experimental conditions at a range of relevant temperatures. Observations were made of liquid composition evolution and solid phases present during stages of the evaporation experiments.

2.2 Numerical Model

EQ3/6 version 8.0a was used to perform the geochemical modeling of the evaporation experiments. It is a geochemical model with Pitzer capabilities developed at Lawrence Livermore National Laboratories (LLNL) to simulate isothermal batch reactions. It is split into two functions that work in series: EQ3 and EQ6. EQ3 equilibrates a starting solution and computes charge balance accounting for formation of complexes. Beginning with the EQ3 output, EQ6 then computes the desired reaction on the equilibrated solution, dissolving and precipitating solids when necessary. Simulations included EQ6 reactions of mixing two EQ3-simulated brines and the removal of water from a starting EQ3-simulated brine (i.e., evaporation of water and concentration of brine).

EQ3/6 requires a reference thermodynamic database for its calculations, which includes formation reactions for a wide variety of minerals and complexes, Pitzer interaction parameters, and reaction log equilibrium constants as a function of temperature. The modeling presented here used a thermodynamic database used during the Yucca Mountain Project, also used by Jové Colón, et al. (2012).

2.3 Modeling and Experimental Methodology

The numerical modeling methodology is similar to the approach taken by Jové Colón et al. (2012), and the experimental methodology is similar to the approach taken by Krumhansl et al. (1991) and McCaffery et al. (1987). The starting composition of brine was first equilibrated with EQ3, which predicts the composition of the solution, based on measurements of species concentrations, pH, and the partial pressure of CO_2 and O_2 in the atmosphere. Using the results of EQ3, EQ6 then simulates the removal of water from the system, representing evaporation of water and concentration of the brine. As the activity of water in the solution decreases and minerals precipitate, the composition of the system evolves.

Figure 7 shows composition of WIPP brines as Na/Cl vs. K/Mg mass ratios (i.e., ratios of concentrations in mg/L rather than moles/L). Each point represents a brine sample (key data listed in Table 4), while the gray line connects points from the evaporation experiment of Krumhansl et al. (1991). This type of representation was used by Krumhansl et al. (1991) to represent various brines observed at WIPP and it is adopted here to represent both laboratory and modeling results.

The use of concentration ratios for the axes allows the plotting of solutions with very different ionic strengths (e.g., seawater and WIPP brine) and it may reduce error associated with large dilution factors needed by most analytical methods. Each axis is normalized by a high-concentration species (Cl^- or Mg^{++}) which increases in concentration during evaporation. The numerators in each axis (Na^+ or K^+) decrease in concentration after crossing a geochemical divide (e.g., Hardie & Eugster, 1970; Eugster et al., 1980; Harvie et al., 1982), due to the presence of new solid salts (e.g., NaCl, $MgSO_4$, or KCl) that additionally constrain the concentrations of aqueous species through the mass action law. Evaporation proceeds towards the lower-left corner of the mass-ratio figure.

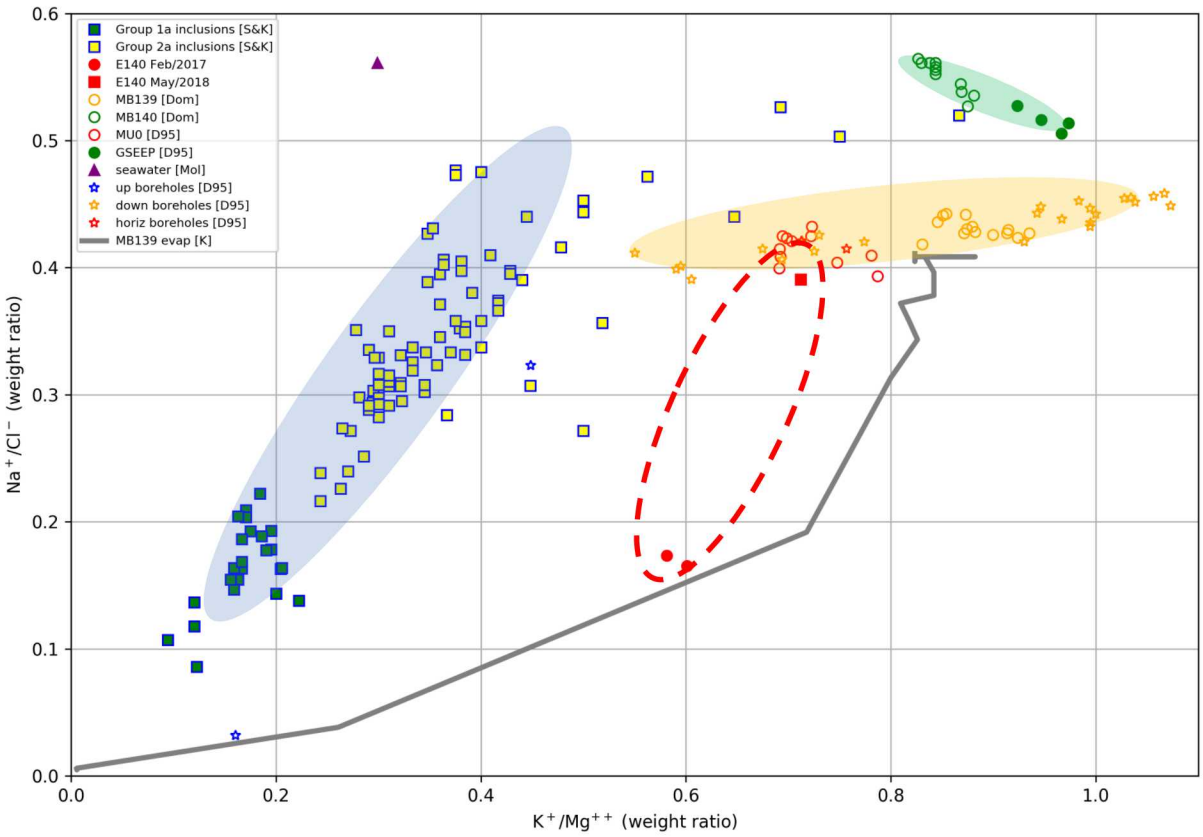

Figure 7. Mass ratios of WIPP brines. Blue ellipse: WIPP fluid inclusions; yellow ellipse: near MB-139; green ellipse: near MB-140; red dashed ellipse: E-140 boreholes.

Different brine types in Figure 7 are grouped visually using colored ellipses. The fluid inclusions from Stein & Krumhansl (1988) (green and yellow squares with blue outlines) tend to have K^+/Mg^{++} ratios that are low and similar to seawater (purple triangle at top). The distinction between group 1 and group 2 fluid inclusions (Krumhansl et al., 1991) is not utilized here. Data from Map Unit 0 (MU-0) horizontal boreholes (Deal et al 1995; red circles and stars) represent the expected composition of intergranular brine to be sampled in the ongoing heater test; these samples plot near the middle of the the yellow ellipse.

Marker Bed 140 (MB-140) vertical boreholes (Roberts et al 1999; green circles) have higher Na^+/Cl^- ratios than samples from vertical boreholes into Marker Bed 139 (MB-139) and horizontal boreholes to MU-0 (both in orange ellipse). MU-0 samples (red circles) have a lower K^+/Mg^{++} ratio than MB-139 samples (orange circles). G-seep WIPP brine (GWB) plots with the MB-140 samples. MB-139 is located immediately below the WIPP disposal horizon (Figure 9) and MB-140 is located stratigraphically below MB-139 (below the interval shown in Figure 9).

Although there is some scatter in the fluid inclusion (intragranular brine) data, there exists a noticeable difference between intergranular brine from the WIPP disposal horizon (green and yellow ellipses and data down-and-to-the-left impacted by evaporation) and fluid inclusions (blue ellipse). This illustrates the expected difference between contributions from intergranular and intragranular brine using compositional analysis.

Table 4. Summary of brine compositions (borehole locations in Figure 10) [g/L]

		Cl^-	Br^-	$SO_4^=$	Na^+	K^+	Mg^{++}	Ca^{++}	Li^+	B
Created brines	Dissolved WIPP ROM salt 1	219	n.d.	2.4	130	0.81	0.12	0.42	n.d.	0.19
	Dissolved WIPP ROM salt 2	220	n.d.	2.8	122	0.90	0.15	0.48	n.d.	0.08
	G-seep brine (GWB) recipe	198	2.2	18	100	19	14	0.4	0.04	1.46
	Adjusted WIPP brine recipe	186	1.5	17	84	14	23	0.28	0.04	1.5
Sampled brines	MU-0 Sample OH20-4039 4/92	193	1.5	17	82	16	22	0.34	n.a.	1.5
	MU-0 Sample OH20-4058 8/92	188	1.5	17	78	15	21	0.27	n.a.	1.4
	MU-0 Sample OH23-4040 4/92	190	1.5	16	80	15	22	0.28	n.a.	1.5
	MU-0 Sample OH23-4056 8/92	185	1.5	16	80	15	21	0.27	n.a.	1.5
	MU-0 Sample OH26-4041 4/92	189	1.5	16	80	16	22	0.28	n.a.	1.5
	MU-0 Sample OH26-4057 8/92	186	1.5	16	79	15	22	0.26	n.a.	1.5
	MU-0 Sample OH45-4042 4/92	188	1.7	16	77	16	21	0.29	n.a.	1.5
	MB-139 QPB-02 (Krumhansl)	163	1.2	13	67	14	17	0.30	0.02	1.5
	E140 SNLCH114 (Feb 2017)	259	2.9	30	43	28	46	0.11	0.05	2.9
	E140 SNLCH111 (Feb 2017)	280	3.2	33	49	29	50	0.12	0.038	2.7
	E140 SNLCH114 (May 2018)	168	3.9	20	66	22	31	0.14	n.d.	1.4
Ratios	avg. MU-0 / avg. dissolved	0.9	-	6.3	0.6	18	158	0.6	-	11
	avg. MU-0 / GWB recipe	1.0	0.7	1.0	0.8	0.8	1.5	0.7	-	1.0
	avg. MU-0 / adjusted recipe	1.0	1.0	1.0	1.0	1.1	0.9	1.0	-	1.0

n.a. = not analyzed; n.d. = not detected

2.3.1 Previous Evaporation Experiments

The evaporation experiments were made to replicate and extend data reported in Krumhansl et al. (1991), a survey on WIPP brines including an evaporation study on MB-139 brine. Although there are many studies related to the evaporation of seawater for commercial salt production (e.g., McCaffery et al. 1987; Babel and Schrieber, 2014), there are few studies on the evolution of WIPP brines or brines of similar compositions.

In Krumhansl et al. (1991), a brine was sampled from QPB-02 (a vertical borehole intersecting MB-139 just below the floor in the Room Q access drift) and was left to evaporate for seven months in open air at ambient temperature (i.e., humidity and temperature during the experiment were not controlled or measured). Liquid samples of brine were analyzed to estimate the ion composition evolution during evaporation. Chloride ion concentrations were measured through titration and precipitation of silver chloride without dilution. Sulfate and bromide concentrations were determined by ion chromatography (IC) of the brine diluted 5,000 and 1,000 times, respectively. Cation concentrations were determined using an emission spectrograph after dilution of 300 to 600 times. The reported lithium ion concentrations in Krumhansl et al. (1991) are incorrect by a factor of 1,000 (reported as parts-per-thousand, but they should be parts-per-million; corrected values are given in Table 6).

The results from the Krumhansl et al. (1991) report were simulated to verify that EQ3/6 could provide predictions comparable to lab measurements (Figure 8, Table 4). Modern seawater evaporation data were available from Babel & Schreiber (2014) (Table 5). These data represent averages across several brine

evaporation ponds using modern seawater as the starting solution. The stages listed in Table 5 correspond to geochemical divides, where different mineral phases are present in solid form. MU-0 intergranular brine is similar in composition to seawater at stage 2.1 (the halite stage), but with elevated levels of K^+ compared to seawater. EQ3/6 was also used to simulate this evaporation data (purple lines in Figure 8).

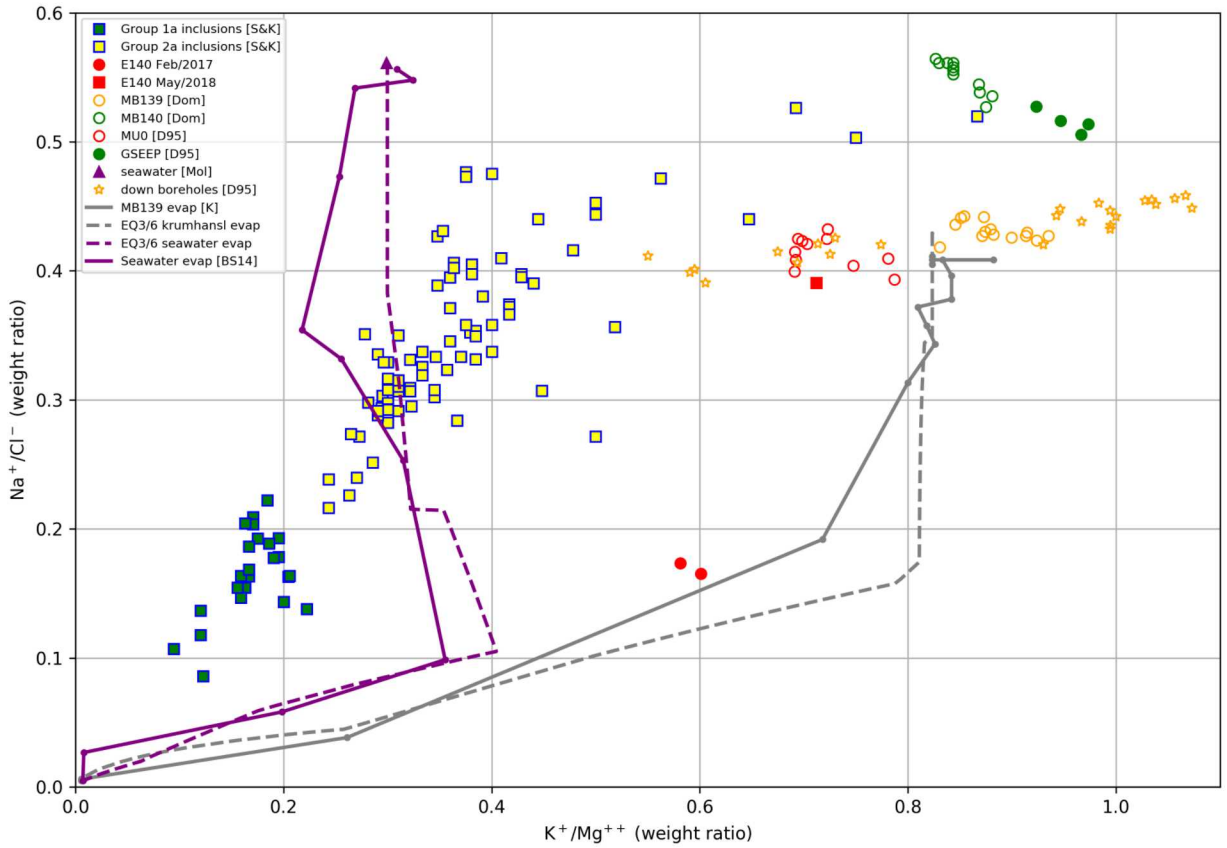

Figure 8. Observations of WIPP brine evaporation (gray) and seawater evaporation (purple). Corresponding EQ3/6 predictions are dashed lines; evaporation proceeds down and left.

Both published evaporation experiments in Figure 8 show general agreement between observations and EQ3/6 simulations for experiments at ambient (~25 C) temperature. The solid lines represent experimental evaporation data, while the dashed lines of the same color are EQ3/6 simulations. The purple lines represent the seawater evaporation data from Babel & Schreiber (2014) and the gray lines denotes the WIPP brine evaporation experiment performed by Krumhansl et al. (1991).

Experimental data (solid lines) are lines connecting a small number of observed points. The seawater evaporation data plotted in Figure 8 are listed in Table 5 (11 samples) and the data from the Krumhanel et al. (1991) evaporation experiment are listed in Table 6 (16 samples). The EQ3/6 model results include a much larger number of points (several hundred points each) with less interpolation between model-predicted points.

Table 5. Evolution of modern seawater during evaporation (Babel & Schrieber, 2014) [g/L]

	Stages	Density [kg/m^3]	TDS	Cl^-	Br^-	$SO_4^=$	Na^+	K^+	Mg^{++}	Ca^{++}
0	Seawater	1.022	35.8	19.8	0.068	2.77	11	0.408	1.32	0.42
1	Gypsum beginning	1.084	124.7	69.0	0.234	10.1	37.8	1.47	4.53	1.54
2	Halite beginning	1.204	307.9	176	0.578	19.1	95.1	3.6	13.4	0.45
2.1	Halite	1.22	334.4	188	0.95	28.9	89	5.3	20.9	0.237
2.2	Halite	1.247	332	185	1.33	36.4	65.6	7.73	35.5	0.17
2.3	Halite	1.238	383.8	190	1.83	65.4	63	12.9	50.5	0.096
3	Epsomite beginning	1.286	400.2	191	2.97	82.2	48.2	17.7	56.1	-
4	Sylvite beginning	1.29	410.3	224	4.77	56.1	22.1	25.9	72.9	-
5	Carnallite beginning	1.305	418.2	258	5.3	35.4	15	17	85.7	-
5.1	Carnallite	1.325	462.6	305	7.38	27.1	8.15	0.86	109	-
6	Bischofite beginning	1.364	504.8	337	7.53	34.9	1.68	0.86	122	0.06

The data reported in Table 4 of Krumhansl et al., (1991) are listed in Table 6. The lithium ion concentrations have been changed to have the correct units, compared to the initial reported values. The first sample in Table 6 (0% mass loss) is the brine sampled from MB-139, also listed in Table 4 (MB-139 QPB-02).

Table 6. Krumhansl et al. (1991; Table 4) MB-139 brine evaporation experiment [g/L]

Sample	Mass Loss %	Cl^-	Br^-	$SO_4^=$	Na^+	K^+	Mg^{++}	Ca^{++}	Li^+	B
1	0.0	163	1.2	13	67	14	17	0.30	0.0235	1.45
2	1.1	163	1.5	13	66	14	17	0.30	0.0232	1.44
3	2.0	164	1.4	13	67	14	17	0.30	0.0259	1.45
4	2.9	164	1.4	13	67	15	17	0.31	0.0237	1.46
5	4.3	164	1.4	14	67	15	18	0.32	0.0252	1.52
6	9.6	164	1.5	14	65	16	19	0.34	0.0247	1.56
7	9.7	164	1.5	15	62	16	19	0.33	0.0252	1.58
8	14.1	164	1.6	16	61	17	21	0.36	0.0283	1.68
9	16.7	165	1.6	16	59	18	22	0.37	0.0301	1.79
10	20.0	166	1.7	18	57	19	23	0.30	0.0237	1.89
11	24.9	166	1.8	19	52	20	25	0.27	0.0301	2.08
12	40.7	172	2.7	27	33	28	39	0.16	0.0455	3.02
13	57.0	193	5.2	47	7.4	18	69	0.04	0.0983	5.61
14	61.6	245	7.8	29	1.5	0.6	107	0.03	0.1270	4.51
15	65.8	248	79	211	1.2	0.5	89	0.02	0.1720	5.62
16	66.0	245	100	285	1.3	0.5	91	0.02	0.1990	6.35

2.3.2 Creation of a Representative MU-0 Brine

In February 2017, samples were collected from standing brine at the back of two adjacent horizontal boreholes in the E-140 drift at WIPP (see samples from SNLCH111 and SNLCH114 in Table 4 and solid red circles near bottom middle in Figure 7). These boreholes are now being used for the hardware-debugging stage of the ongoing heater test (see Section 1 of this report). The composition of these February 2017 samples was quite different from the brine used as the starting point in the Krumhansl et al. (1991) evaporation experiment (see MB-139 QPB-02 in Table 4 and upper right end of gray line in Figure 7) or other reported samples for MU-0 (Table 4 and open red circles in Figure 7), because the brine had experienced significant evaporation from exposure to mine ventilation over at least 3 years. The February 2017 sample is similar to MB-139 brines after significant evaporation (i.e., between samples 11 and 12 in Table 6); solid red circles in Figure 7 plot near gray line of the Krumhansl et al. (1991) evaporation experiment.

A sample was collected from SNLCH114 before installation of the packer and heater in May 2018 (Table 4 and filled red square in Figure 9). This more recent sample is a more representative brine sample, similar to that seen historically in MU-0 (orange circles). Between February 2017 and May 2018, the borehole was cleaned out and isolated from the mine ventilation with a sewer plug. The later sample more closely represents the expected unmodified intergranular brine composition in the formation (yellow ellipse).

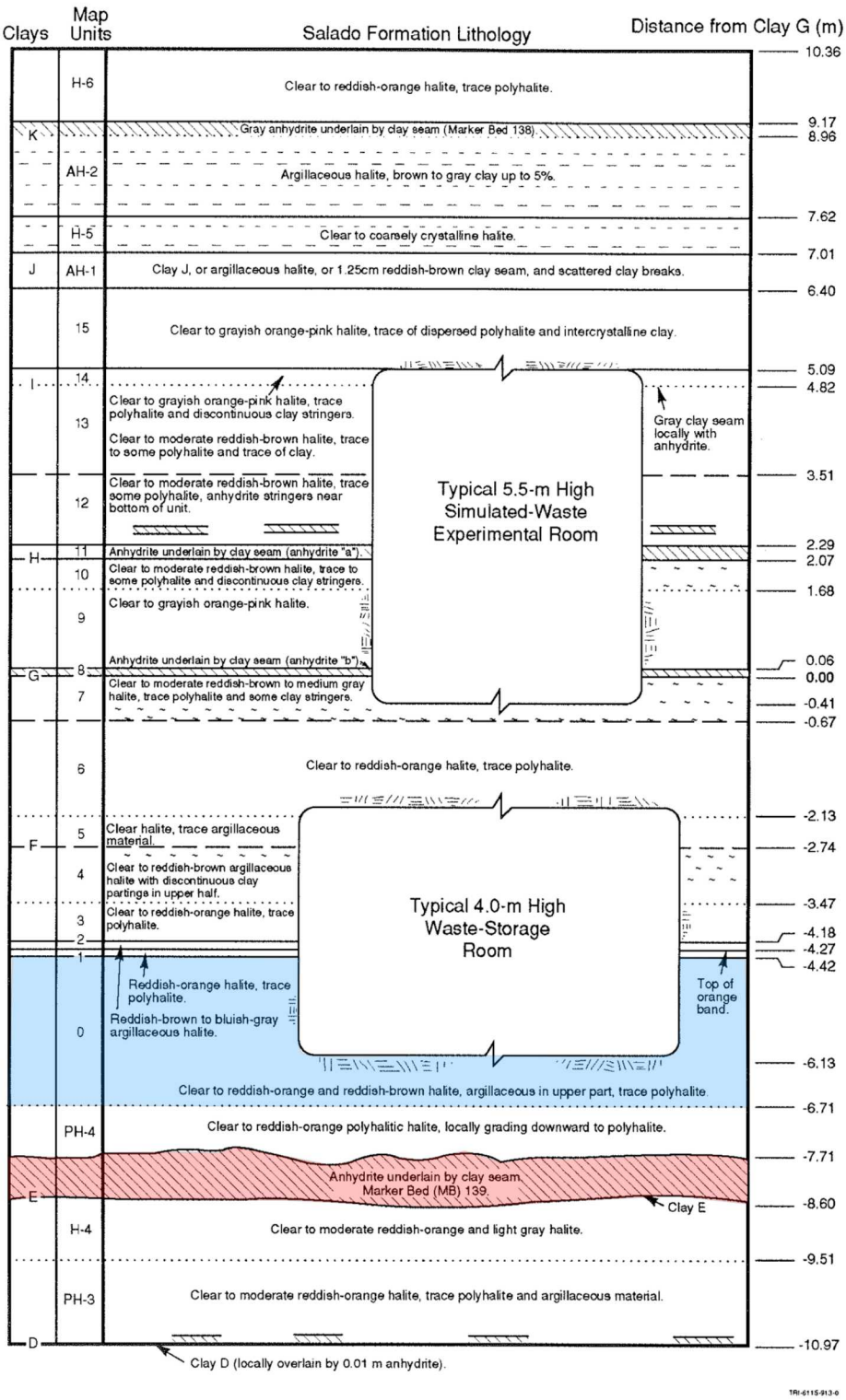

Figure 9. WIPP horizon stratigraphy (modified from Fig 2-3 of Roberts et al. 1999). MU-0 indicated in blue, MB-139 indicated in red.

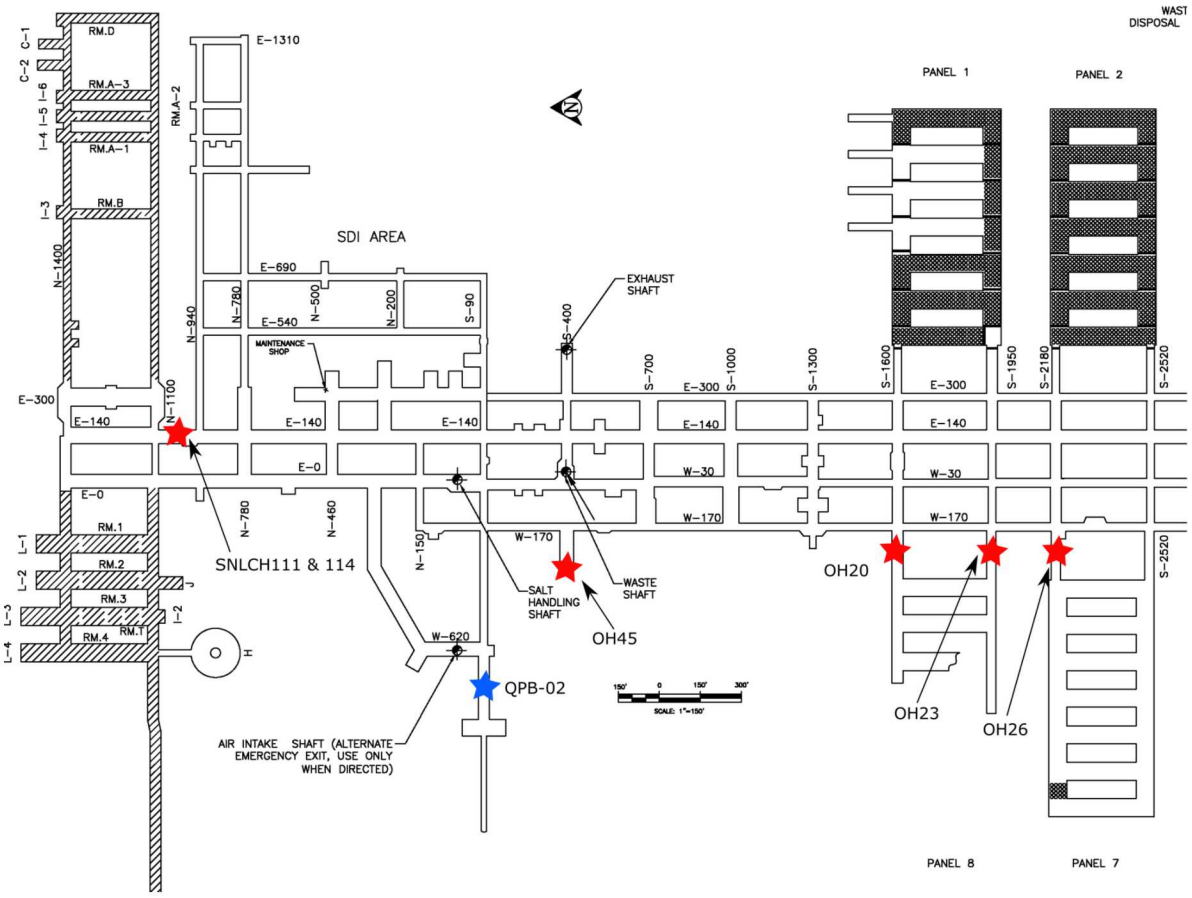

Figure 10. WIPP underground with borehole locations; horizontal boreholes (red stars) and vertical borehole (blue star) sampled for brine composition (data in Table 4)

Large quantities of brine were not available from MU-0 to conduct laboratory evaporation experiments using the brine expected during the upcoming heater test (see Table 4, data from Tables D1 & D2 of Deal et al., 1995). Surrogate brines were created to use in laboratory evaporation experiments.

The first attempt to recreate WIPP brine dissolved WIPP run-of-mine (ROM) salt. The WIPP ROM salt was obtained in 2017 derived from Panel 8 mining activities before the 2014 WIPP shutdown, and was not systematically sorted, sampled, or prepared. ROM salt was added to one liter of deionized (DI) water and agitated on a shaker table until it no longer dissolved (about 4 days). Compositional analyses of this brine showed the brine from dissolved salt was very different from the intergranular brines observed in MU-0 (see two red stars near upper right in Figure 11). The brines from dissolved salts had much lower levels of K^+, Mg^{++}, $SO_4^=$, and B (i.e., components associated with non-halite minerals like sylvite, anhydrite, polyhalite, borax, and epsomite); significantly elevated levels of Na^+ and Cl^- (i.e., ions associated with halite); and no detectable Li^+ or Br^- (i.e., brine components not associated with any minerals – see Table 4). Although there are no common bromine minerals, bromine is found in Salado Formation halite on the order of 25-105 parts per million (Adams, 1969), with the actual amount related to the concentration of Br^- in solution at the time of halite precipitation. Observed species in the brine created from WIPP ROM salt indicate it was created mostly from dissolving halite, with possible minor amounts of sylvite (KCl), antarcticite ($CaCl_2 \cdot 6H_2O$), and tachyhydrite ($Mg_2CaCl_6 \cdot 12H_2O$), based solely on the resulting brine stoichiometry (not on the identification of mineral phases).

A second attempt to create WIPP brine from WIPP salt first pulverized the ROM salt using a mortar and pestle before dissolving it into one liter of DI water on a shaker table in an attempt to better dissolve less-

soluble sulfate minerals. This second attempt resulted in brine of similar composition to the first ROM salt derived brine. Both of these brine samples are very different from intergranular or intragranular brine observed in boreholes or fluid inclusions observed at WIPP (Table 4, Figure 11).

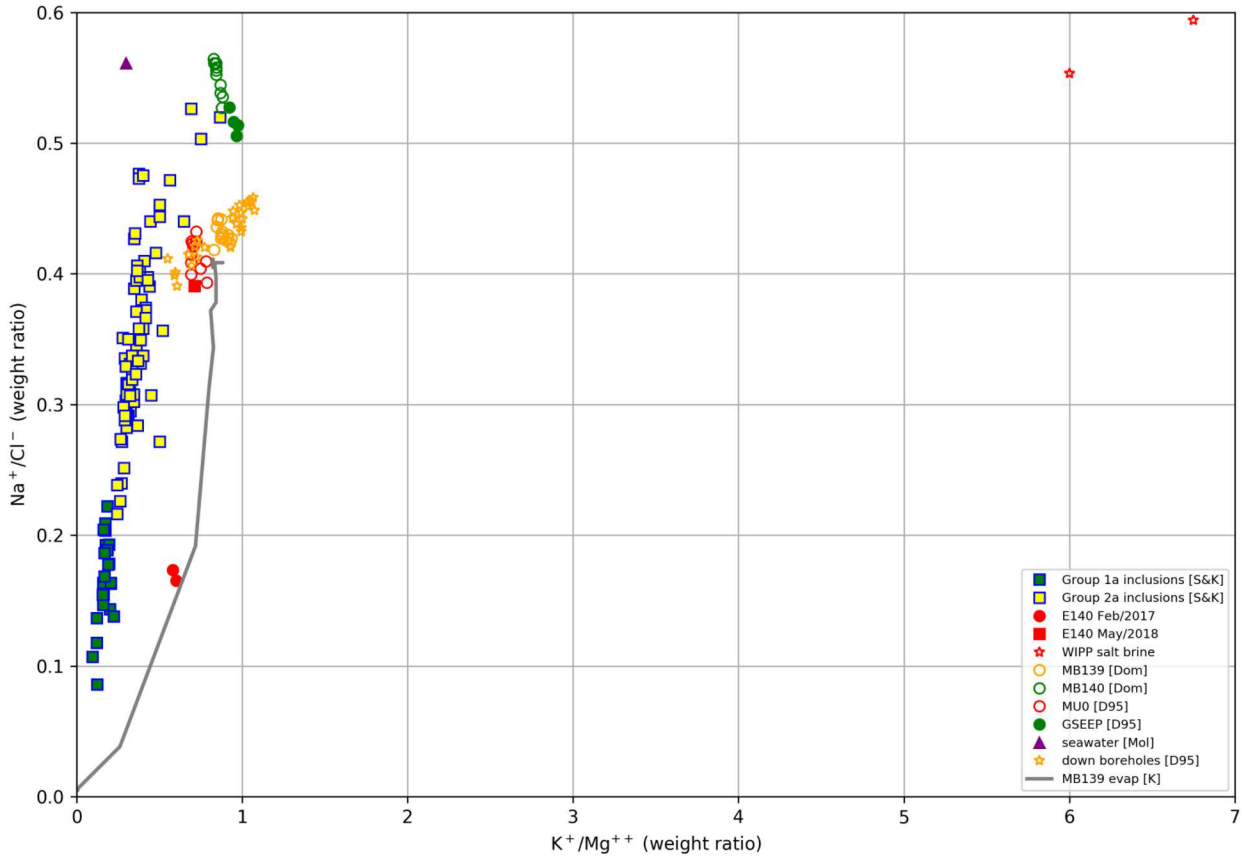

Figure 11. Mass ratio plot with samples from dissolved WIPP salt (red stars in upper right corner)

These naive attempts to create WIPP brine from WIPP salt illustrate how dissolving WIPP salt does not result in a solution that looks like WIPP intergranular brine. This is analogous to creation of a brine during the dissolution of salt through condensation of steam as humid vapor is exposed to cooler salt. It should be straightforward to compositionally discern MU-0 intergranular brine from re-condensed vapor that has re-dissolved WIPP salt.

During *in-situ* borehole heater tests related situation may occur. If the relative humidity (RH) is less than 75% (deliquescence RH for halite) but greater than the deliquescence point for other minerals (e.g., some Mg-Cl salts can deliquesce at RH below 50%), other minerals may preferentially dissolve before halite in the humidity, without liquid condensation. While this process would result in a brine different from that produced using DI water and ROM salt, it is unlikely this process would result in a brine compositionally similar to MU-0 intergranular brines either. Further experiments could be conducted to test this hypothesis.

To create a brine closer to the expected MU-0 intergranular brine composition, an existing approach (Xiong, 2008) to create G-Seep WIPP Brine (GWB in Table 4, based on GSEEP samples from the floor of Room G at WIPP, shown in Figure 7) was modified. Using the same salts as Xiong (2008), a brine was created using different proportions the salts to match the expected MU-0 brine composition better (Table 7). The synthetic brine was created to match an average MU-0 brine observed by Deal et al. (1995), specifically the arithmetic average of composition observed in the seven MU-0 samples listed in Table 4.

Table 7. G-seep WIPP brine recipe and modified MU-0 recipe [g salt/L solution]

Salt	GWB (Xiong, 2008)	MU-0 brine
NaCl	179.61	177.08
KCl	34.84	29.45
LiCl	0.19	0.21
$Na_2B_4O_7 \cdot 10(H_2O)$	15.06	12.91
$CaCl_2 \cdot 2(H_2O)$	2.03	1.04
NaBr	2.74	1.96
$MgCl_2 \cdot 6(H_2O)$	207.05	180.44
Na_2SO_4	25.23	24.02

Evaporation experiments were modeled at 25, 75, and 100 ºC. EQ3/6 simulations were performed at a pH of 6.65 (i.e., corresponding to predictions of the NBS pH scale), which is based on typical reported pH values from Deal et al. (1995).

2.3.3 Current Evaporation Experiments

Evaporation studies in the laboratory were conducted in a vacuum oven (at ambient Albuquerque atmospheric pressure) to simulate borehole conditions, at 50, 75, and 100 ºC. The experiment sampling strategy evolved through several iterations to address adequate sample volume, sampling schedule, sample collection and separation techniques, and to refine analytical procedures on lab instruments. The schedule of exposure times for brine samples in the oven were varied by sample volume and oven temperature, to leave enough liquid sample and create enough solid sample for subsequent analytical procedures.

The first approach considered extracting samples periodically from a single large volume (similar to the approach of Krumhansl et al., 1991). However, this approach was not used as the removal of liquid brine samples could alter the system composition (i.e., change the solid/liquid ratio), and this approach would make it difficult to collect representative samples of precipitated minerals before the endpoint. Secondly, it was believed a beaker of evolving brine and precipitant could be stratified (i.e., not well-mixed), and small liquid samples extracted from a large beaker might not be representative of the entire volume.

The first iteration of our experimental procedure included brine samples of 10 mL in multiple 50 mL beakers (see Figure 12). Individual beakers were removed from the oven after different lengths of exposure times, allowing collection of a solid and liquid sample, while minimally influencing the evolution of the remaining samples (aside from impacts to the overall humidity inside the oven). After removal from the oven, they were weighed to document evaporative water mass loss followed by extracting the total liquid in the beaker to further dilute and analyze.

To better isolate any remaining liquid brine from the precipitant (i.e., held to crystals by surface tension), the second procedural iteration used centrifuge tubes with a permeating filter. During sampling, beaker solid and liquid contents were immediately emptied into filter tubes and centrifuged. Brine was extracted from the centrifuge tubes and diluted to analyze on the IC and inductively coupled plasma optical emission spectrometry (ICP-OES). Precipitant solids were collected for analysis on the XRF, SEM, and re-dissolved for additional compositional analysis.

During all evaporation experiments, the timing of sample collection was important. The degree of evaporation in the experiment does not progress linearly with time (i.e., evaporation proceeds slowly at first, then it accelerates rapidly), and it is influenced by the overall humidity in the oven. There were

several beginning trials to determine appropriate sampling schedules and exposure times at each temperature. Sampling too early produced similar samples (too little evaporation occurred). Sampling too late resulted in too little liquid left for analyses. The sampling schedule was different for each temperature. Sampling schedules were varied between replicate tests at the same temperature to producing better coverage of the total evaporation curve, with the goal of better constraining model predictions.

Figure 12. Evaporation experiments in vacuum oven and isolated precipitants (evaporation proceeds left to right)

2.3.4 Characterization of Solution

Ion chromatography (IC) analysis was conducted to estimate concentrations of major anions and cations of evaporated brines. An IC separates molecules or ions based on their affinity to an exchanger, resulting in peak conductivity responses at different retention times for each ion that can be deduced to determine concentration with respective standards and calibration. For anions, an AS23 analytical column was used to measure F^-, Cl^-, NO_2^-, NO_3^-, Br^-, $SO_4^=$, and P^-, and for cations, a CS12 analytical column to measure K^+, Ca^{++}, Na^+, Mg^{++}, Li^+, and NH_4^+. Calibration standards of concentrations 0.1, 1, 5, 10, 25, and 50 mg/L were used. The IC cannot detect uncharged species (e.g., H_2SiO_4 or $B(OH)_3$).

Due to the very high ionic strengths of these brines (Table 4), samples were diluted by a factor of 1:10,000 with DI water. An issue with the cation analysis was peak interferences between species due to sizable differences in peak area (proportional to concentration). For instance, the peak retention time for Mg^{++} and Ca^{++} were very close, thus even with a high dilution, Mg^{++} produced a large response peak that overshadowed the much smaller Ca^{++} peak. The Ca^{++} response was a "rider peak" on the falling limb of the Mg^{++} peak, which makes it difficult to accurately estimate Ca^{++} concentration on the IC. The high dilution factor (required to prevent plugging the IC column with Na^+, Cl^-, and Mg^{++}) reduced the Li^+ response to just below the IC detection limit. Therefore, the ICP-OES was used to accurately estimate Li^+ and Ca^{++} concentrations.

A PerkinElmer Optima 8000 ICP-OES was used to estimate the elemental concentrations in the liquid brines, most importantly for Li^+ and Ca^{++}. It uses a plasma ignited from argon gas to atomize and ionize samples, thereby exciting ions, changing their energy state, causing them to emit light at a characteristic wavelength that can be detected by a spectrometer. The ICP-OES instrument is more flexible than the IC; it has several relevant options used when performing analysis, such as changing the spectrometer view to be more or less sensitive, adjusting detected wavelengths, and changing analysis times. Using these options, samples did not have to be diluted as much as in the IC, and single elements could be analyzed independent of others. Dilution factors were 1:100 and 1:1,000 with 2% nitric acid.

Measurements of pH were not possible in all laboratory samples; smaller, more evaporated samples often had enough liquid to allow analysis via IC and ICP-OES (with significant dilution), but not enough to estimate pH in their undiluted state. When enough sample is available, the pH of brines is estimated by first measuring the pH using a probe calibrated with typical pH standard buffers (i.e., at low ionic

strength), then correcting the pH value using published factors that depend on brine composition (e.g., Kirkes, 2018). Correction factors have been developed for typical WIPP brines, but they do not cover the high ionic strengths encountered during the later portions of the evaporation experiments. To estimate pH, the correction factors will either be extrapolated beyond their valid range or re-calibrated to the relevant ionic strengths.

2.3.5 Characterization of Precipitant

To further characterize the evolution the brine, the precipitated solid phases were analyzed using several approaches. First, the precipitated solids were re-dissolved in DI water and analyzed using similar methods used with the liquid brine samples, to estimate ratios of ion concentrations. Initial attempts to identify minerals in the solid phase using X-ray diffraction (XRD) were not successful, since halite is present at such high levels in all samples and this mineral dominates the XRD response, making it difficult to identify second- and third-order minerals of interest. Some of the secondary minerals are similarly soluble in water as halite (e.g., sylvite or antarcticite), therefore the solid salt samples could not simply be washed with DI water to remove halite before analysis. As such, it was attempted to discern what assemblages of minerals could produce ratios of ions observed in re-dissolved brines, and the elemental makeup of precipitated salt samples using X-ray fluorescence (XRF).

XRD can be used to identify minerals directly, but another analysis step is required to estimate mineral makeup from XRF elemental composition or relative ion composition in re-dissolved brine. The analysis first started with a list of candidate minerals expected to precipitate (Eugster et al., 1980). These minerals were represented as a matrix (minerals as rows, ionic species as columns; Table 8). The concentration of ionic species obtained from IC and ICP-OES analyses in brines created by re-dissolving the solids comprised a vector. The concentrations were converted to molarities (assuming a one-liter solution, these were then converted to moles) to build a vector of observed mole ratios (presented in results section).

This mineral composition matrix and brine composition vector were used to solve for a mineral composition vector with the relative amounts of each mineral that could result in the measured ionic species. The mineral composition vector was estimated using the non-negative least squares (NNLS) method, available from the Python scipy library (www.scipy.org). NNLS imposes a constraint of a zero-minimum value for each unknown in the matrix. Using standard least squares resulted in physically unrealistic negative relative quantities of minerals.

Table 8. Stoichiometry of minerals considered in evaporation experiments excluding H_2O [mol/mol]

	Carnallite	Kainite	Halite	Kieserite[1]	Leonite[2]	Sylvite	Anhydrite[3]	Polyhalite	Glauberite	Aphthitalite	Antarcicite	Bischofite	Bloedite	Syngenite	Tachyhydrite	Thenardite
Ca	0	0	0	0	0	0	1	2	1	0	1	0	0	1	1	0
K	1	1	0	0	2	1	0	2	0	3	0	0	0	2	0	0
Mg	1	1	0	1	1	0	0	1	0	0	0	1	1	0	2	0
Na	0	0	1	0	0	0	0	0	2	1	0	0	2	0	0	2
Cl	3	1	1	0	0	1	0	0	0	0	2	2	0	0	6	0
SO_4	0	1	0	1	2	0	1	4	2	2	0	0	2	2	0	1

1. kieserite, epsomite & hexahydrite only differ by hydration
2. leonite & picromerite only differ by hydration
3. anhydrite and gypsum only differ by hydration

Analysis was done using a ThermoFisher XRF to estimate of the elemental composition of the precipitated solids independently from the IC/ICP-OES analyses of re-dissolved salts. An X-ray gamma source excites atoms in a solid sample, where secondary or fluorescent X-rays are emitted. Each element produces a unique set of characteristic X-rays at certain wavelengths and orbital shells. However, the available detector type was not able to detect elements with an atomic number less than 10 (i.e., including fluorine, boron, and lithium). Sample preparation involved crushing by mortar and pestle to create well-mixed homogenous-sized particles.

A Tescan Vega3 LM scanning electron microscope (SEM) was also used to investigate mineral orientation and morphology, as well as approximate composition, of precipitant solids. The SEM is equipped with an energy-dispersive X-ray spectroscopy (EDS) detector which can produce image maps of energy spectrums for elemental analysis. In order to be examined by SEM, precipitants were gently placed on a carbon stub, and further sputter coated with Au/Pd to create a conductive surface to reduce charging during imaging with the electron beam.

2.4 Results and Discussion

Brine composition during the three temperatures of evaporation experiments are listed in Table 9, Table 10, and Table 11. The data are plotted along with the corresponding EQ3/6 model results in mass-ratio figures (Figure 13, Figure 14, and Figure 15) and with both solid phases and liquid components in experimental progress figures (Figure 19, Figure 20, and Figure 21).

2.4.1 Brine Composition at 50 ºC

The 50 ºC evaporation experiments took the longest time to execute (≤ 50 hours). Table 9 shows the composition observed in the samples (4 or 6 samples) across the three experimental replicates. All the data listed in Table 9 are plotted as pink hexagons in Figure 13. Even though the experiment of Krumhansl et al. (1991) was run at ambient room temperature (assumed 25 ºC), the data shown 50 ºC are similar, given the difference in the starting compositions (MU-0 vs MB-139; Table 4). The recent E-140 MU-0 samples (red circles and square) also fall within the scatter of the 50 ºC experimental data.

Table 9. Brine composition in 50 ºC evaporation experiments [g/L]

	Mass loss [%]	Time [hrs]	Cl^-	Br^-	$SO_4^=$	Li^+	Na^+	K^+	Mg^{++}	Ca^{++}	B
1-1	35.5	24	180.3	4.845	32.71	0.028	52.95	30.84	44.45	0.190	-
1-2	50.5	47	208.8	6.656	51.29	0.054	22.07	33.67	74.30	0.111	-
1-3	56.6	53	213.3	7.997	60.79	0.069	9.058	27.36	87.95	0.084	-
1-4	59.7	72	227.4	9.974	93.90	0.122	5.445	6.908	114.6	0.045	-
2-1	29.3	16	210.4	3.593	27.36	0.04	68.82	23.58	34.83	0.19	3.28
2-2	29.2	20	200.2	3.612	26.20	0.03	71.43	26.08	36.01	0.48	3.22
2-3	39.2	24	251.5	5.207	39.70	0.05	60.58	30.44	51.77	0.40	4.54
2-4	59.2	40	241.6	7.330	41.64	0.12	7.64	23.69	118.3	-	10.47
2-5	60.2	44	267.5	9.222	90.30	0.14	8.65	27.37	122.6	-	12.83
2-6	61.4	48	315.8	10.274	38.08	0.16	4.07	6.66	119.4	-	13.89
3-1	9.2	7.9	197.2	3.041	19.24	0.078	78.79	17.03	23.49	0.317	2.417
3-2	24.7	23.8	196.1	3.615	23.63	0.082	62.12	20.42	29.32	0.393	2.845
3-3	31.3	29.8	202.7	4.187	28.27	0.089	56.71	24.41	34.91	0.493	3.316
3-4	34.9	32.8	205.9	3.969	30.93	0.091	51.39	26.55	38.66	0.521	3.630
3-5	50.5	47.8	229.8	6.006	49.59	0.122	22.89	35.72	64.50	0.593	5.747
3-6	54.2	55.8	250.4	7.010	59.96	0.134	13.69	28.09	78.42	0.213	6.876

The samples in Table 9 are numbered based on the order they were removed from the vacuum oven, but degree of evaporation should be judged by the final composition, not by the exposure time or mass loss percentage (possibly some exchange of vapor/condensate between beakers through humidity in the oven).

The potassium ion concentration first goes up in each of the experiments (Table 9), then it declines in later samples. This is due to precipitation of a potassium-bearing salt, where the other component(s) of the salt are present in higher concentrations than potassium (i.e., the sample is crossing a geochemical

divide). Sylvite may be precipitating at this point in the evaporation progress. Only the second experiment progressed far enough (e.g., sample 2-6) to show a drop in the concentration of sulfate ion, due to the precipitation of a sulfate salt (where the other components of the salt are higher concentration than sulfate) and a corresponding geochemical divide. Sample 2-6 also shows the highest concentrations of lithium, chloride, and bromine ions, further indicating it had evaporated the most of all the samples collected at 50 ºC.

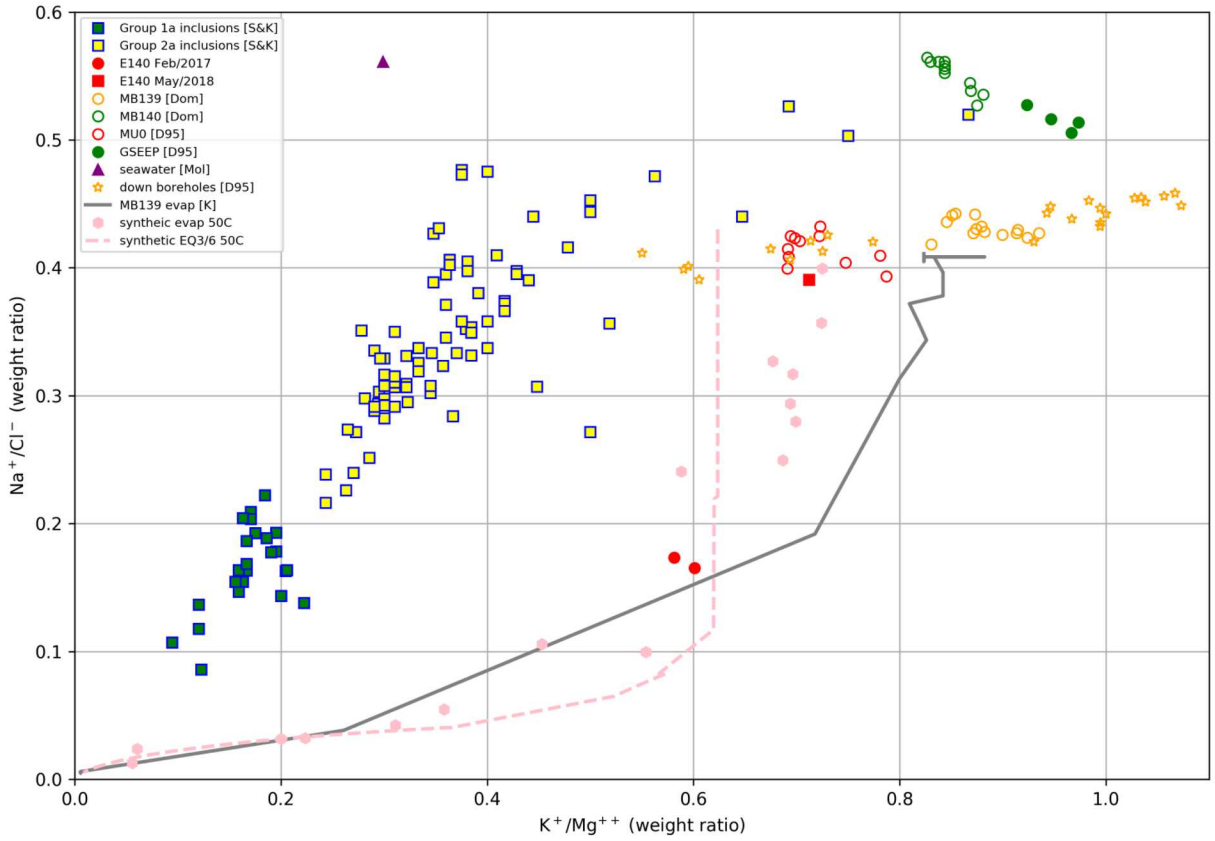

Figure 13. Mass ratio plot showing 50 ºC data (pink hexagons) and EQ3/6 results (dashed line)

The EQ3/6 simulation (pink dashed line) shows good agreement with the observations. The data show a shallower slope during the beginning phase of evaporation. The model predicts a vertical line, while the data show a gentler slope. This is seen in both the Krumhansl et al. (1991) evaporation experiment data (at 25 ºC), and the recent lab data (i.e., see general agreement between slopes of pink hexagonal dots and gray line). The model is predicting no change in the K/Mg ratio during the initial phase of evaporation (i.e., a vertical line), while the data show a change in this ratio (i.e., a steep slope but not vertical). This slope may be due to potassium and magnesium ion concentrations increasing at different rates during evaporation experiments. This apparent discrepancy between observations and EQ3/6 model predictions will be investigated further.

2.4.2 Brine Composition at 75 ºC

The three replicates of the 75 ºC evaporation experiments ran much faster (≤ 8.5 hours) than the 50 ºC evaporation experiments, but they also did not progress as far in the evaporation process. Sulfate ion concentrations only increased, and only sample 2-6 showed a decrease in potassium ion concentrations. There are fewer samples located in the later part of the evaporation curve at 75 ºC (Figure 14), after the break in slope, compared to the 50 ºC experiment (Figure 13).

Table 10. Brine composition in 75 ºC evaporation experiments [g/L]

	Mass loss [%]	Time [hrs]	Cl^-	Br^-	$SO_4^=$	Li^+	Na^+	K^+	Mg^{++}	Ca^{++}	B
1-1	29.4	5.3	176.0	2.591	22.83	0.04	66.66	24.51	34.09	0.45	3.07
1-2	33.7	6	210.4	3.164	29.30	0.04	63.59	26.87	37.95	0.48	3.40
1-3	42.0	6.8	211.1	3.982	36.32	0.05	50.01	35.07	50.65	0.63	4.35
1-4	43.6	7.3	212.5	4.270	38.17	0.05	44.66	35.06	49.76	0.67	4.48
1-5	51.5	7.8	228.5	5.416	49.14	0.07	26.61	48.39	69.65	0.71	6.01
1-6	53.8	8.3	250.3	5.678	55.03	0.07	21.43	49.39	73.65	0.61	6.38
2-1	20.6	3.5	265.7	2.587	21.72	0.074	68.77	19.95	28.41	0.405	2.852
2-2	27.1	4.5	270.5	2.845	25.28	0.076	64.30	23.17	33.10	0.473	3.158
2-3	38.3	6	284.5	3.700	34.68	0.090	49.36	29.66	43.12	0.549	3.980
2-4	44.1	7	286.2	4.210	41.19	0.099	36.55	35.14	51.78	0.655	4.659
2-5	49.0	7.5	298.4	4.904	50.47	0.112	25.13	37.15	62.57	0.720	5.486
2-6	56.1	8.5	332.1	6.351	71.75	0.140	10.96	25.85	88.29	0.461	7.704
3-1	13.0	2	261.8	2.344	19.09	0.061	75.61	17.84	25.88	0.328	2.465
3-2	19.3	3	265.4	2.633	21.49	0.065	68.73	19.48	28.25	0.338	2.692
3-3	28.6	4	272.1	2.973	26.31	0.070	61.93	23.84	35.79	0.422	3.269
3-4	33.4	5	271.4	3.435	29.64	0.077	56.56	26.40	39.07	0.479	3.589
3-5	43.5	6	278.3	4.330	39.74	0.091	37.69	34.56	51.63	0.604	4.606
3-6	49.8	7	296.8	5.041	51.14	0.102	24.75	36.74	66.82	0.640	5.838

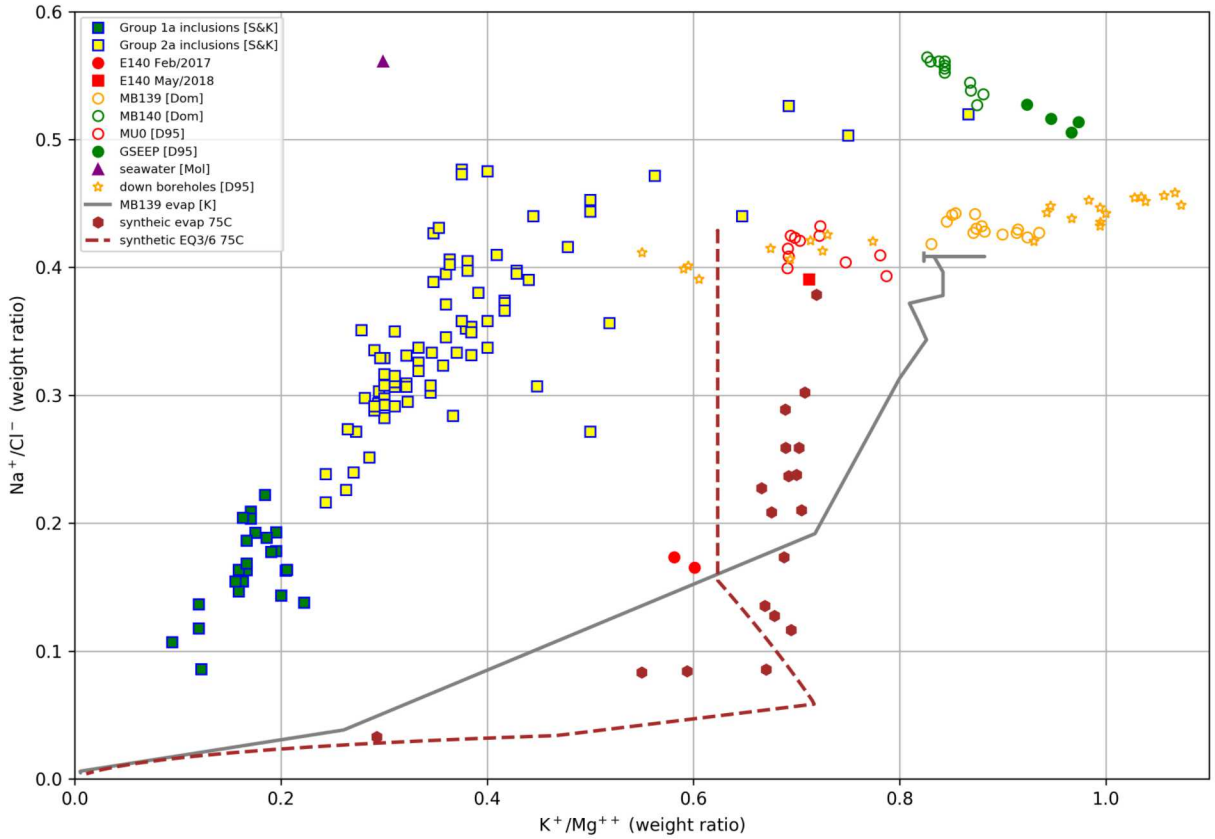

Figure 14. Mass ratio plot showing 75 ºC data (brown hexagons) and EQ3/6 results (dashed line)

The data make a well-defined cluster, the location of which generally agrees with the EQ3/6 predictions. The model shows vertical line, followed by a significant kick to the right (compared to the 50 ºC model predictions). The laboratory observations show a steeper slope than was observed in the Krumahnel et al., (1991) experiment, the recent samples from E-140, or the 50 ºC (Figure 13), but not as steep as the model prediction. The difference in observed and predicted slope will be investigated further.

2.4.3 Brine Composition at 100 ºC

The 100 ºC evaporation experiments ran the fastest (≤ 5.5 hours) but show the largest amount of scatter in the data. The samples are labeled based on their exposure time in the vacuum oven, but the concentrations of conservative species (i.e., chloride, bromide, and lithium) indicate the last samples (1-4, 2-4, 3-4 and 4-4) experienced less evaporation than their immediate predecessors (1-3, 2-3, 3-3, and 4-3). The last 100 ºC evaporation samples also all developed a crust across the top of the liquid in the beaker, which slowed evaporation progress. Especially in these later samples, exposure time in the oven is not directly related to mass lost, or progress indicated by brine composition.

Table 11. Brine composition in 100 ºC evaporation experiments [g/L]

	Mass loss %	Time [hrs]	Cl^-	Br^-	$SO_4^=$	Li^+	Na^+	K^+	Mg^{++}	Ca^{++}	B
1-1	22.0	1	225.3	3.207	35.91	0.01	82.40	25.12	29.34	0.12	2.62
1-2	37.6	2	207.7	3.413	47.98	0.03	54.32	30.56	41.00	0.28	3.59
1-3	47.0	3	237.1	5.121	43.65	0.05	41.74	49.29	61.41	1.31	5.19
1-4	49.0	4	230.7	5.033	40.44	0.05	50.37	46.19	59.82	0.47	5.18
2-1	17.4	1	190.0	2.509	19.23	0.06	90.78	20.02	29.80	0.19	2.36
2-2	37.3	2	209.2	3.569	31.31	0.07	58.29	27.83	41.53	0.41	3.35
2-3	52.0	3.3	264.4	6.304	57.89	0.11	20.93	52.12	84.24	0.52	6.86
2-4	49.2	4	234.3	4.445	42.57	0.09	45.65	42.29	64.62	0.68	5.42
3-1	33.7	2	308.8	9.909	38.91	0.072	52.49	25.37	37.74	0.483	3.481
3-2	56.0	4.5	258.3	6.885	65.55	0.130	11.12	25.82	89.72	0.288	7.505
3-3	58.8	5	251.0	7.738	67.92	0.164	8.963	20.27	94.10	0.218	9.751
3-4	54.9	5.5	219.2	6.248	51.89	0.123	13.76	28.94	83.44	0.240	7.366
4-1	48.1	2	218.9	5.641	44.05	0.0762	28.13	41.85	60.45	0.615	5.322
4-2	56.0	4.5	248.3	7.037	58.36	0.0968	11.36	28.75	87.06	0.225	7.574
4-3	58.4	5	242.0	7.937	65.74	0.1192	8.897	23.98	95.59	0.136	9.328
4-4	57.8	5.5	251.2	7.802	57.46	0.1114	9.598	24.98	92.00	0.124	8.78

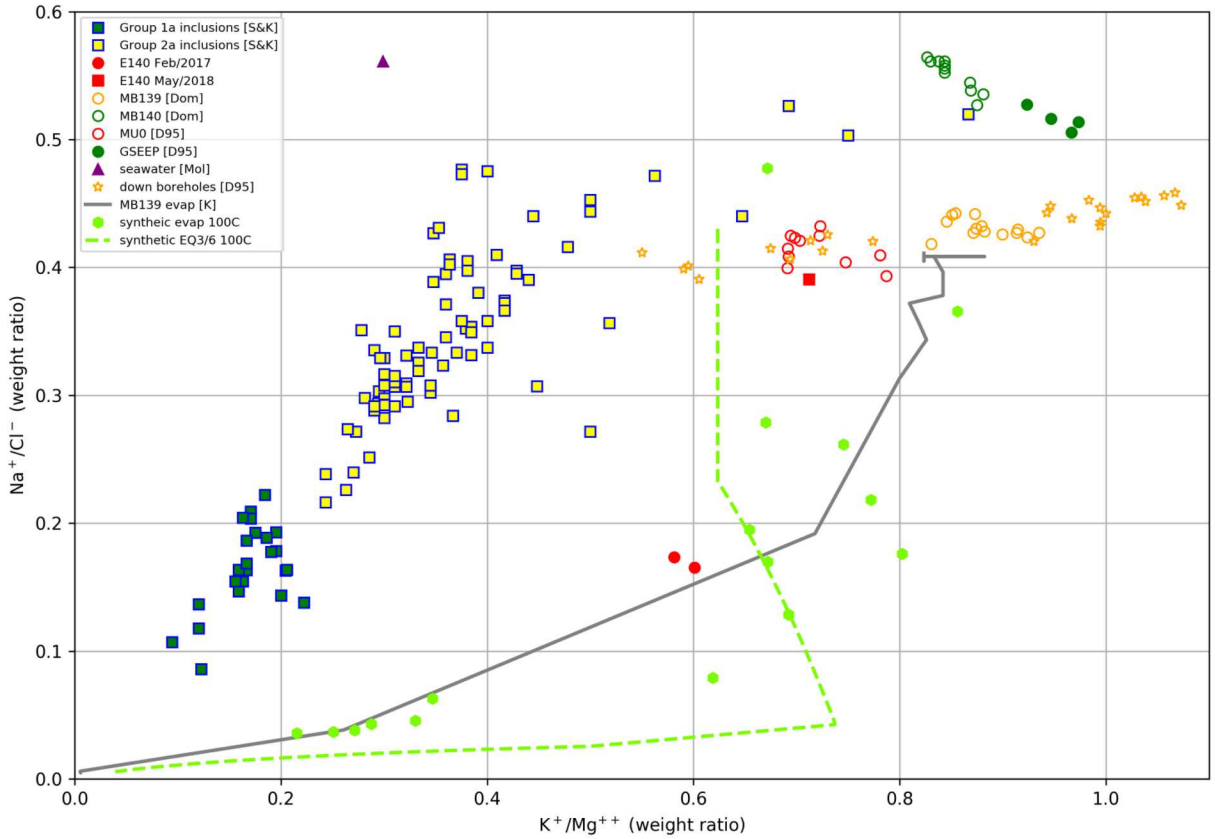

Figure 15. Mass ratio plot showing 100 ºC data (green hexagons) and EQ3/6 results (dashed line)

The model prediction for the 100 ºC experiments shows the most significant kick to the right after the initial vertical stage (Figure 15), but the laboratory data are too scattered to conclusively support or refute this prediction. The cause of the high degree of variability observed in the 100 ºC experiments is not clear, since the same analytical procedures were used to analyze the resulting brines as were used on the samples from the 50 ºC and 75 ºC experiments. It is possible the hot solid and liquid components changed after being taken out of the oven, during the short time the brine and solid phases were together at room temperature before centrifugation. It is also possible the hotter samples interacted more strongly than the 50 ºC and 75 ºC experiments with the ambient humidity in the oven and the lab, which was not controlled and varied between the replicates.

2.4.4 EQ3/6 Summary

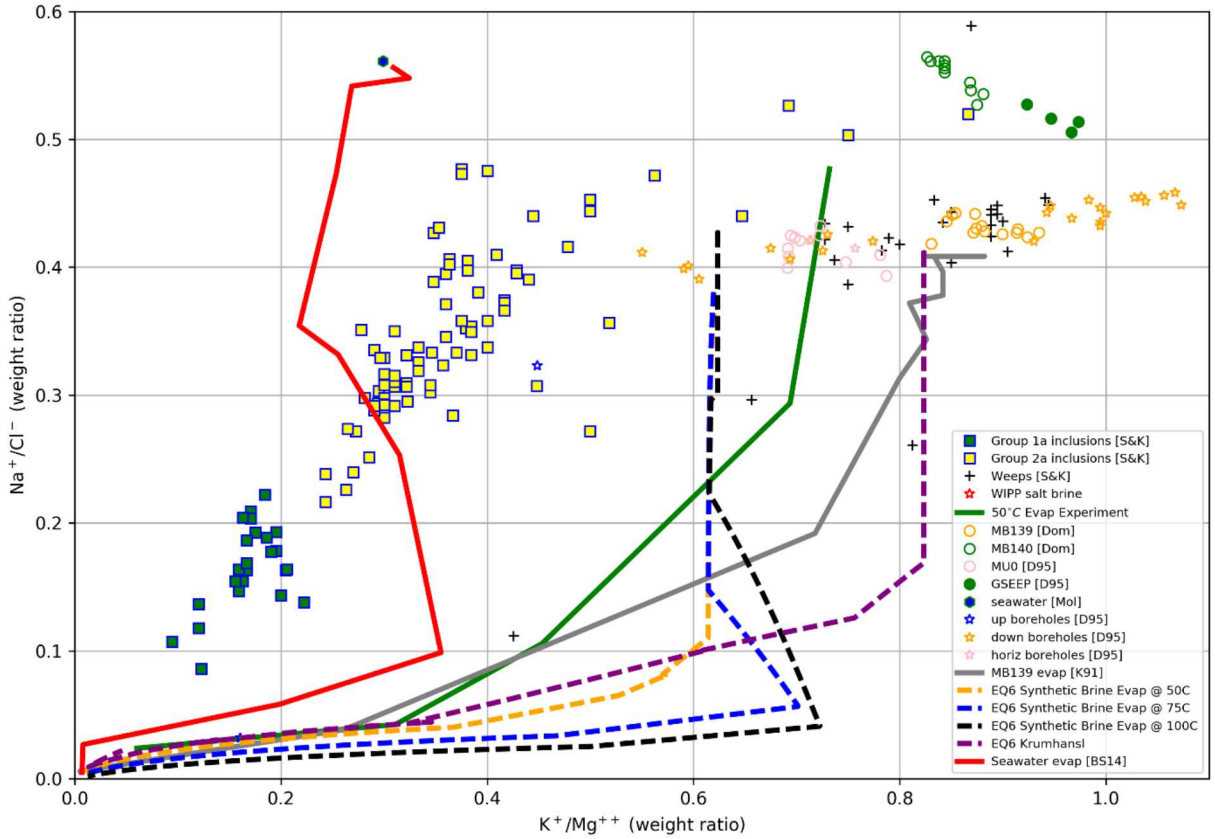

Figure 16. Mass ratio plot showing multiple EQ3/6 simulations

Figure 16 compares EQ3/6-simulated evaporation of the synthetic brine at three temperatures to literature data and our simulated evaporation of the MB-139 brine detailed in Krumhansl et al. 1991. All four sets of EQ3/6 results display the same initial behavior; as evaporation proceeds, the Na/Cl ratio decreases as the K/Mg ratio stays the same (a vertical line), until they reach a kink. Changes in the slope of the model predictions represent changes in the minerals present (i.e., divides). The nature of the predicted "kink" in the EQ3/6 results is a function of temperature, with a larger kink to the right at higher temperatures.

Figure 16 also clearly shows how the model predictions are nearly identical at early times, which is not necessarily supported by the data.

2.4.5 Solid Composition Results

Table 12, Table 13, and Table 14 present the compositional results for analysis on re-dissolved salts. The absolute values of the data are not meaningful, only the relative concentrations (i.e., ratios). Table 12 shows composition for re-dissolved salts from the second replicate evaporation experiment (same sample names as in Table 9). The first three samples (2-1 through 2-3) are almost entirely halite (sodium and chloride), with minor amounts of potassium in the first two samples.

The later three samples (2-4 through 2-6) show significant amounts of sulfate and potassium, which agrees with the data in Table 9 that show potassium ion concentrations decreasing in the last three samples, indicating a geochemical divide related to a potassium-bearing salt, where potassium is combining with a higher concentration ion (e.g., Cl^- or $SO_4^{=}$). The sulfate ion concentration continues to

increase until the last sample (2-6), indicating it is precipitating with a species of higher concentration (e.g., Mg^{++}, which also shows elevated levels in sample 2-6 of Table 12).

Table 12. Re-dissolved precipitant in 50 ºC evaporation experiment [g/L]

	Cl^-	$SO_4^=$	Na^+	K^+	Mg^{++}	Ca^{++}
2-1	5.160	-	3.45	0.08	-	-
2-2	5.352	-	3.50	0.02	-	-
2-3	5.228	-	3.47	0.00	-	-
2-4	4.551	0.343	2.60	0.41	0.15	0.0063
2-5	4.849	0.196	2.77	0.30	0.17	0.0034
2-6	4.351	0.563	2.21	0.49	0.30	0.0089

While the 50 ºC evaporation experiment showed a clear transition in precipitated salts (dashed line in Table 12), the variation in salts observed in the 75 ºC evaporation experiment is more gradational (Table 13). The relative level of potassium in the initial samples at 75 ºC (~40% of chloride concentrations) is much higher than that observed in any of the 50 ºC samples, and this ratio drops with evaporation progress. The 75 ºC evaporation experiment shows more diversity in precipitants at early stages in the evaporation progress, compared to the 50 ºC experiments, which showed only halite. None of the 75 ºC samples showed detectable levels of sulfate, which was important in samples 4-6 at 50 ºC, supporting the previous statement that the 75 ºC experiments did not progress as far along the evaporation curve as the 50 ºC experiments.

Table 13. Re-dissolved precipitant in 75 ºC evaporation experiment [g/L]

	Cl^-	$SO_4^=$	Na^+	K^+	Mg^{++}	Ca^{++}
1-1	5.000	-	3.423	2.016	0.0131	0.0163
1-2	4.109	-	2.557	1.005	0.0117	0.0163
1-3	4.785	-	3.109	0.713	0.0187	0.0163
1-4	4.929	-	2.666	0.505	0.0217	0.0168
1-5	4.861	-	2.370	0.483	0.0278	0.0178
1-6	4.600	-	2.841	0.560	0.0374	0.0184

The 100 ºC evaporation experiment is more similar to the 50 ºC experiment, since primarily sodium and chloride are present in the early samples (samples 1-1 and 1-2 in Table 14). Contrary to the 50 ºC data, the 100 ºC experiment shows traces of magnesium in early samples, rather than potassium. In the hotter experiment, none of the re-dissolved precipitant samples show detectable levels of potassium, while this was the third most concentrated species (behind sodium and chloride) in all but one (2-6 at 50 ºC) of the samples of the 50 ºC and 75 ºC tests.

Table 14. Re-dissolved precipitant in 100 ºC evaporation experiment [g/L]

	Cl^-	$SO_4^=$	Na^+	K^+	Mg^{++}	Ca^{++}
1-1	5.398	-	3.32	-	0.04	-
1-2	5.132	-	3.18	-	0.05	-
1-3	5.154	-	3.25	-	0.06	0.0018
1-4	5.198	0.163	3.38	-	0.07	0.0038

Limited XRF results are given in Table 15. These compare with the last data point from each of the re-dissolved solids results given in Table 12, Table 13, and Table 14. The XRF results are already normalized to weight percent, as reported by the instrument and Table 16 gives normalized results from salt re-dissolution analysis given in previous tables for comparison.

Table 15. XRF results of final precipitant samples [weight %]

T [°C]		Cl	Br	S	Na	K	Mg	Ca
50	2-6	57.58	2.79	2.22	22.70	9.46	5.02	0.15
75	1-6	58.42	1.87	0.33	35.00	3.28	0.91	0.08
100	1-4	61.70	2.52	0.54	32.90	1.06	0.97	0.16

The XRF results are similar to those derived from re-dissolving precipitated salts, with some exceptions. The re-dissolved salts showed no sulfate in the 75 ºC:1-6 sample, while the XRF results showed the presence of sulfur. The re-dissolved salts showed no potassium in the 100 ºC:1-4 sample, while XRF results for this sample showed potassium weight percent higher than magnesium and sulfur.

At all three temperatures the XRF results show measurable bromide, at levels higher than calcium and sulfur. This bromine is likely substituted for chloride into the halite crystals (Adams, 1969) or possibly present in fluid inclusions. This bromine should also present in the liquid samples derived from re-dissolving the precipitants, but apparently it is at levels below the detection limit of the IC. The XRF results appears more sensitive to minor components than the analysis of re-dissolved brine.

Table 16. Normalized salt re-dissolution results for select samples [weight %]

T [°C]		Cl^-	Br^-	$SO_4^=$	Na^+	K^+	Mg^{++}	Ca^{++}
50	2-6	54.9	-	7.11	27.9	6.18	3.79	0.11
75	1-6	57.1	-	-	35.3	6.95	0.46	0.23
100	1-4	59.0	-	1.85	38.3	-	0.79	0.04

Using the re-dissolved salt composition data, and the NNLS estimation approach, the salts were estimated that were present during the evaporation experiment (Table 17 and Table 19). The solutions presented here to the NNLS optimization problem are not exact but represent most-likely combinations of salts required to produce the ratios of ions observed. The matrix representing the physically plausible solid mineral phases given by Eugster et al. (1980) has rank 5, meaning one of the rows/species (in this case the last row, sulfate) can be expressed as a linear combination of the other rows/species. Rank deficiency of the matrix means the optimization results are less unique than if the matrix was full rank (6).

Table 17 shows almost exclusively halite is present in samples 1 through 3 of the 50 ºC evaporation experiment, while later samples (4 through 6) show the hydrous species carnallite ($KMgCl_3 \cdot 6H_2O$) was

present in significant quantities and the minerals aphthitalite ($NaK_3(SO_4)_2$), bloedite ($Na_2Mg(SO_4)_2 \cdot 4H_2O$), and tachyhydrite ($Mg_2CaCl_6 \cdot 12H_2O$) were present in trace quantities.

Table 17. NNLS-predicted minerals in 50 °C evaporation experiments [mole %]

	Carnallite	Kainite	Halite	Kieserite	Leonite	Sylvite	Anhydrite	Polyhalite	Glauberite	Aphthitalite	Antarcicite	Bischofite	Bloedite	Syngenite	Tachyhydrite	Thenardite
2-1			99.0							0.3						0.7
2-2			99.7													0.2
2-3			99.2													0.8
2-4	4.7		93.6							1.3			0.2			
2-5	4.9		94.3							0.4			0.5			
2-6	9.3		87.6							0.9			1.9		0.3	

Table 18 shows that at 75 ºC the precipitants are dominated by halite to a lesser degree, with higher levels of potassium. This combination leads to a prediction of significant amounts of sylvite (KCl) and the remaining sodium is then associated with thenardite (Na_2SO_4). Minor amounts of aphthitalite, antarcticite ($CaCl_2 \cdot 6H_2O$), and tachyhydrite are also predicted in the last four samples. Sylvite and thenardite are predicted to be present in early samples but make smaller fraction of the total solids by the end of the experiment.

Table 18. NNLS-predicted minerals in 75 °C evaporation experiment [mole %]

	Carnallite	Kainite	Halite	Kieserite	Leonite	Sylvite	Anhydrite	Polyhalite	Glauberite	Aphthitalite	Antarcicite	Bischofite	Bloedite	Syngenite	Tachyhydrite	Thenardite
1-1			63.9			25.9										10.2
1-2			77.0			18.2										4.8
1-3			92.6			5.5				1.9						
1-4			88.4			10.3					0.5				0.9	
1-5			85.4			11.4					1.3				1.8	
1-6			91.8			7.3				0.9						

Table 19 shows that at 100 ºC all samples had significant halite, with minimal contributions of carnallite, bischofite ($MgCl_2 \cdot 6H_2O$) and tachyhydrite. The highest average proportion of halite across the entire experiment was found in the 100 ºC evaporation experiment.

Table 19. NNLS-predicted minerals in 100 ºC evaporation experiments [mole %]

	Carnallite	Kainite	Halite	Kieserite	Leonite	Sylvite	Anhydrite	Polyhalite	Glauberite	Aphthitalite	Antarcicite	Bischofite	Bloedite	Syngenite	Tachyhydrite	Thenardite
1-1	0.3		98.9									0.2			0.6	
1-2	0.2		98.6									0.9			0.3	
1-3			98.4	0.2								1.4				
1-4			98.5	1.5												

The XRF observations (Table 15) were similarly analyzed using the NNLS approach (Table 20). Results from XRF also indicate halite is unsurprisingly the primary mineral phase, but differences exist as to the secondary mineral phases predicted. The rows of Tables 17-19 that correspond to samples in Table 20 are shaded.

Table 20. NNLS-predicted minerals using XRF data [mole %]

T [°C]		Carnallite	Kainite	Halite	Kieserite	Leonite	Sylvite	Anhydrite	Polyhalite	Glauberite	Aphthitalite	Antarcicite	Bischofite	Bloedite	Syngenite	Tachyhydrite	Thenardite
50	2-6	16.1		77.8			3.9									0.5	1.7
75	1-6	2.1		95.4			2.3				0.3						
100	1-4			94.5			2.9					0.1				2.5	

SEM images (Figure 17) were taken of precipitants at different stages of evaporation, at each of the three experimental temperatures. Based on the compositional analysis, these crystals are halite with minor amounts of other minerals. EDS compositional maps were not taken yet. The SEM images show larger crystals at higher temperatures, but more systematic investigation (including EDS compositional results to map the occurrence of non-halite phases) will be performed in FY19 to confirm other analyses of precipitants via re-dissolution and XRF.

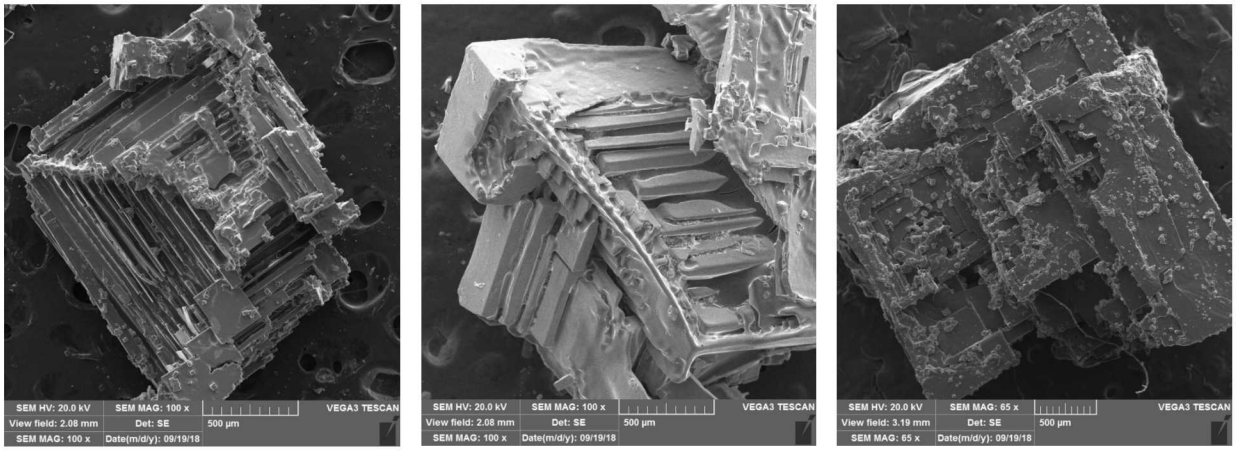

Figure 17. SEM images of precipitants 50 °C: 3-6 (left), 75 °C: 3-6 (middle), and 100 °C: 3-4 (right)

2.4.6 Evaporation Experiment Results Summary

The results of the liquid composition analysis agreed with previous results of Krumhansl et al. (1991), especially at lower temperatures. The 100 ºC experiments showed more scatter in the liquid composition data than the lower-temperature experiments. The solids collected in the 50 ºC and 100 ºC initially were primarily halite, with other salts upon further evaporation. This is consistent with the seawater evaporation sequence presented in Table 5. WIPP MU-0 brine is similar to stage 2.1, which is during the phase of primary halite precipitation, but MU-0 brine has higher potassium ion concentrations (resulting in it plotting further to the right on the mass ratio plots). The high levels of potassium in the 75 ºC test were a bit of an anomaly.

Mass ratio plots show good general agreement between model predictions and observations. Despite general agreement, the model predictions indicated vertical lines at early time, while the data from these experiments and those of Krumhansl et al. (1991) show a less steep slope at lower temperatures.

The preliminary analysis of the solid components from the evaporation experiments agrees qualitatively between analysis of re-dissolved components and XRF. Of the minerals included in the NNLS analysis,

kainite, leonite, anhydrite, polyhalite, glauberite, and syngenite were not predicted to be present at levels above 0.1%. The NNLS analysis is based solely on stoichiometry and does not take the thermodynamic stability of phases into account, and therefore its predictions should be checked against those of a thermodynamically constrained model like EQ3/6. Further analysis will be conducted using EDS and SEM to identify the spatial distribution and nature of mineral phases.

2.4.7 Analysis of Degree of Evaporation

The mass ratio plots do not allow straightforward indication or prediction of solid phases present during evaporation. Krumhansl et al. (1991) used the ternary Jänecke diagram to infer the solid phases in equilibrium with the brine during evaporation; these plots were not created for this report. Instead of the Jänecke diagrams, this study plotted the evolution of both the solid and liquid components are shown during the evaporation experiment using the x-axis to represent evaporation progress. This evaporation progress approach allows plotting both the solid and liquid components predicted by the numerical simulations and observed in the laboratory results. The most convenient way to plot predictions would be using the activity of water (or EQ3/6's reaction progress variable, ξ) as a measure of the degree of evaporation – however, this is more difficult to control or measure experimentally (equivalent to RH).

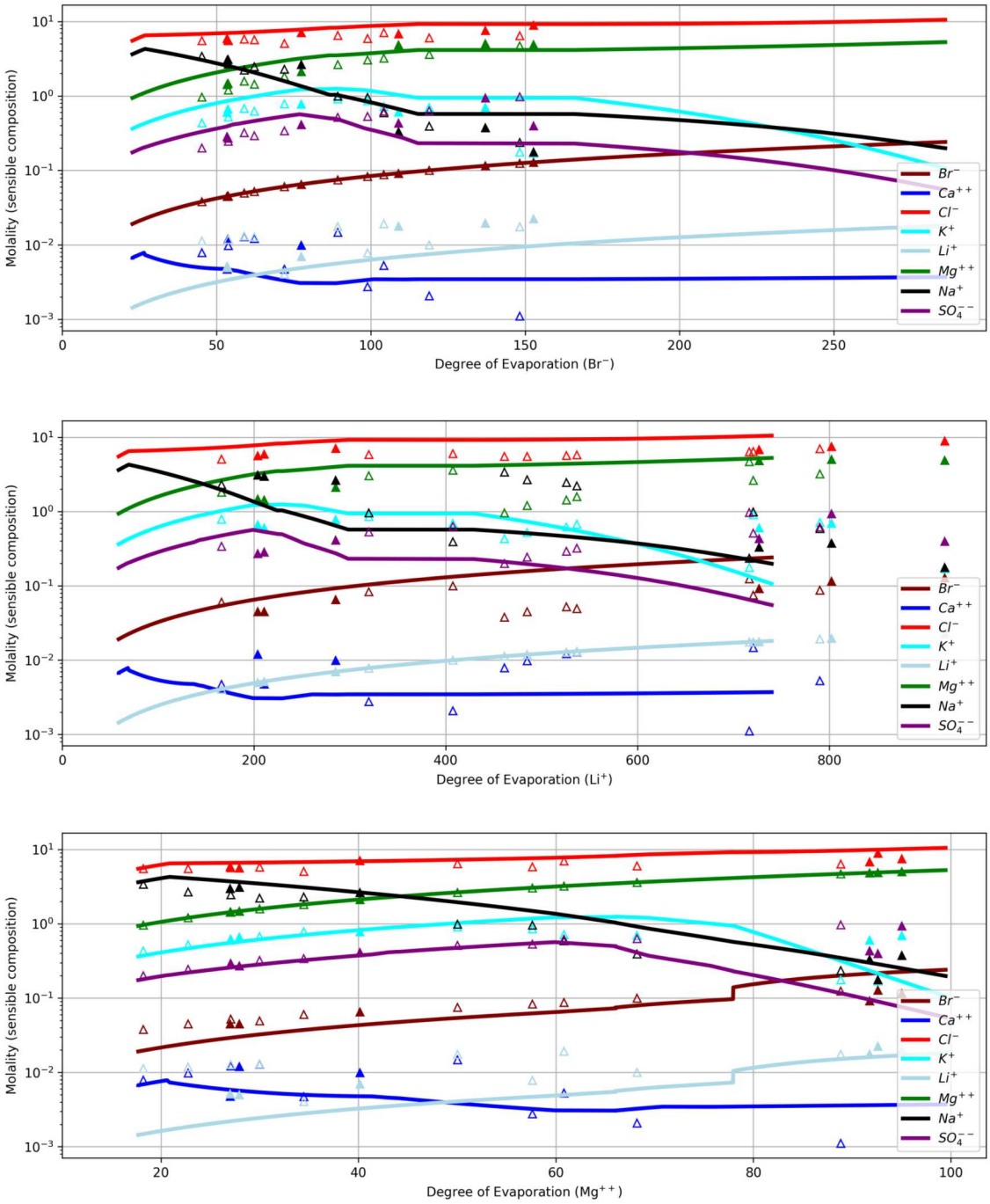

Figure 18. Liquid composition vs. degree of evaporation (50 °C) calculated using Br^-, Li^+, and Mg^{++}. Lines are EQ3/6 results; markers are observations. Solid markers correspond to samples with solid analyses.

Three different normalization approaches were investigated to approximate the degree of evaporation from lab-measured compositional data, to allow plotting both model output and lab experiments on the

same figure, including solid phase composition. McCaffery et al. (1987) used a combination of Mg^{++} and Li^{+} for degree of evaporation.

The most straightforward way to estimate degree of evaporation, is through a conservative ion that does not precipitate out during the evaporation process. Li^{+} would have been an ideal ion, but it is present in concentrations near the detection limit and therefore makes a poor candidate for normalizing all other data (i.e., dividing by noisy values makes all data noisy). Another option was to use Br^{-}, which is also largely conservative (e.g., see monotonically increasing Br^{-} concentrations observed during evaporation in Table 5 and Table 6) and is present at levels ~10 times higher in WIPP brine than Li^{+}. Unfortunately, Br^{-} was measured with the IC, which has higher detection limits than the ICP-OES. Lithium ion concentrations are lower and bromine concentrations, but they can be measured on the ICP-OES, which has a lower detection limit than the IC. As stated earlier, Br^{-} will also substitute into halite crystals during precipitation and is not completely conservative. In the end both of these ions had some issues being used as a measure of the degree of evaporation. Mg^{++} is present at much higher levels, and therefore makes a better measure of degree of evaporation, but only until Mg-Cl salts begin to form later in the evaporation process, then the concentration of Mg^{++} is modified by the solids present.

The “degree of evaporation” axes shown in Figure 18 compare the same EQ3/6 predictions and observations using the three different method proposed for scaling. The numbers on each of the degree of evaporation axes are not meaningful, they simply represent the number of times this species is concentrated over the level found in seawater. Clearly, the representation of the model predictions and laboratory results on these plots are not unique. Further investigation will be made to determine the most informative way to plot these results and make quantitative statements about model/data agreement.

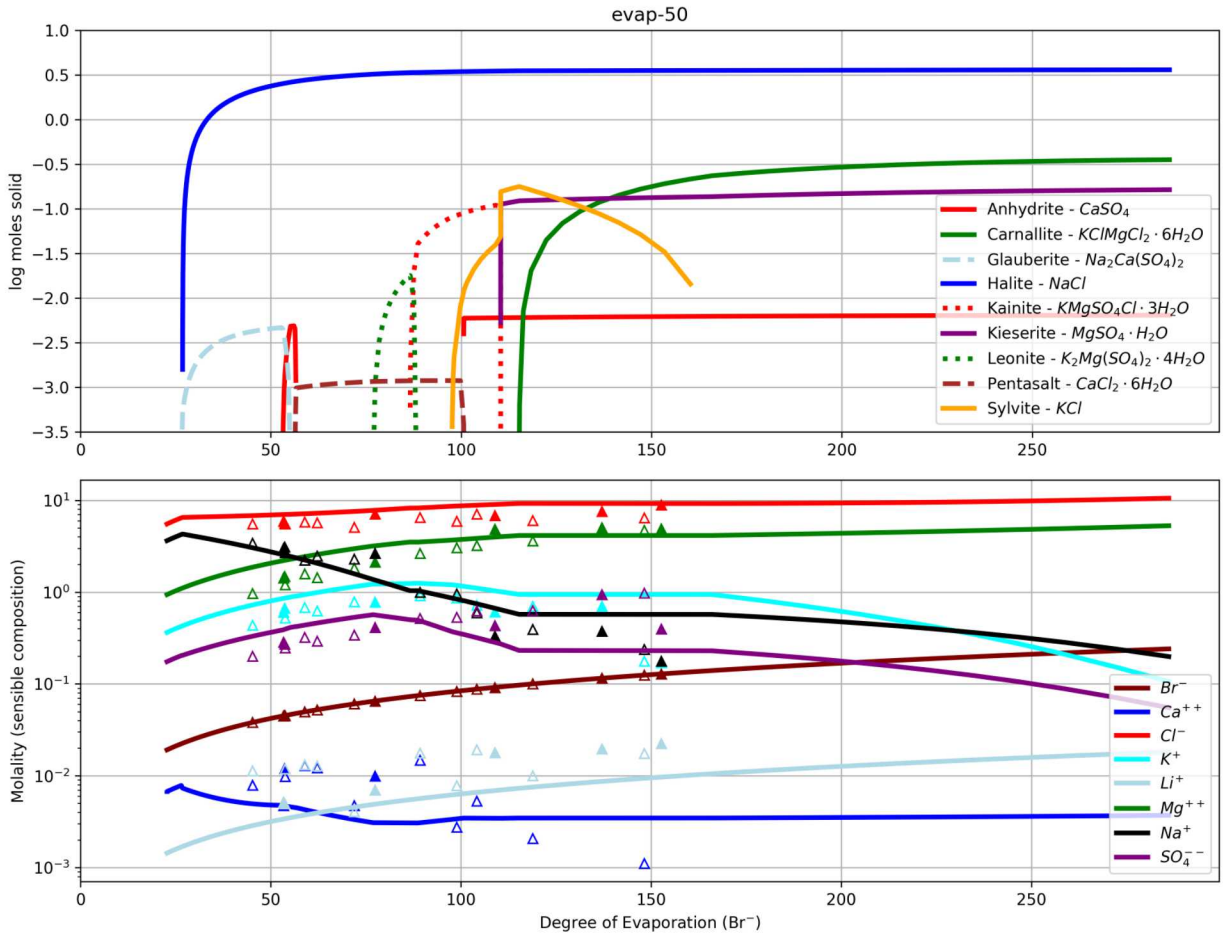

Figure 19. EQ3/6 predicted liquid and solid components during evaporation at 50 ºC; solid markers are samples with precipitant analyses

The solid triangles in Figure 19 correspond to the samples listed in Table 17, which were analyzed for precipitant composition by re-dissolution of solids. The blue curve in the upper subplot shows EQ6 predicts the majority of the precipitant to be halite, as was estimated from the NNLS analysis. For the rightmost three solid triangles (samples 2-4 through 2-6), EQ6 also predicts carnallite to be a significant mineral (solid green line in upper subplot), about one order of magnitude lower than halite (sample 2-6 was predicted to have ~9% carnallite and ~90% halite in Table 17). EQ6 predicted Kieserite to be the next most prevalent mineral, while the NNLS analysis showed other minerals not predicted by EQ6.

In the lower subplot of Figure 19, the sulfate data continue to rise in concentration at higher degrees of evaporation, after the model-predicted sulfate concentrations drop (purple markers and line). This bend in the predicted concentration of sulfate corresponds to a chemical divide where the system of leonite-kainite-kieserite are first predicted to appear during evaporation. EQ6 predicts a decline in sulfate concentration after a degree of evaporation of about 75. Potassium predictions and observations follow similar trends (cyan markers and line, with the drop associated with the chemical divide related to the appearance of sylvite), and both calcium (dark blue) and lithium (light blue) ion concentrations are generally higher in the laboratory data than were predicted by EQ6. Calcium ion concentrations drop in the EQ6 prediction because of the appearance of glauberite, but this is not necessarily reflected in the observations.

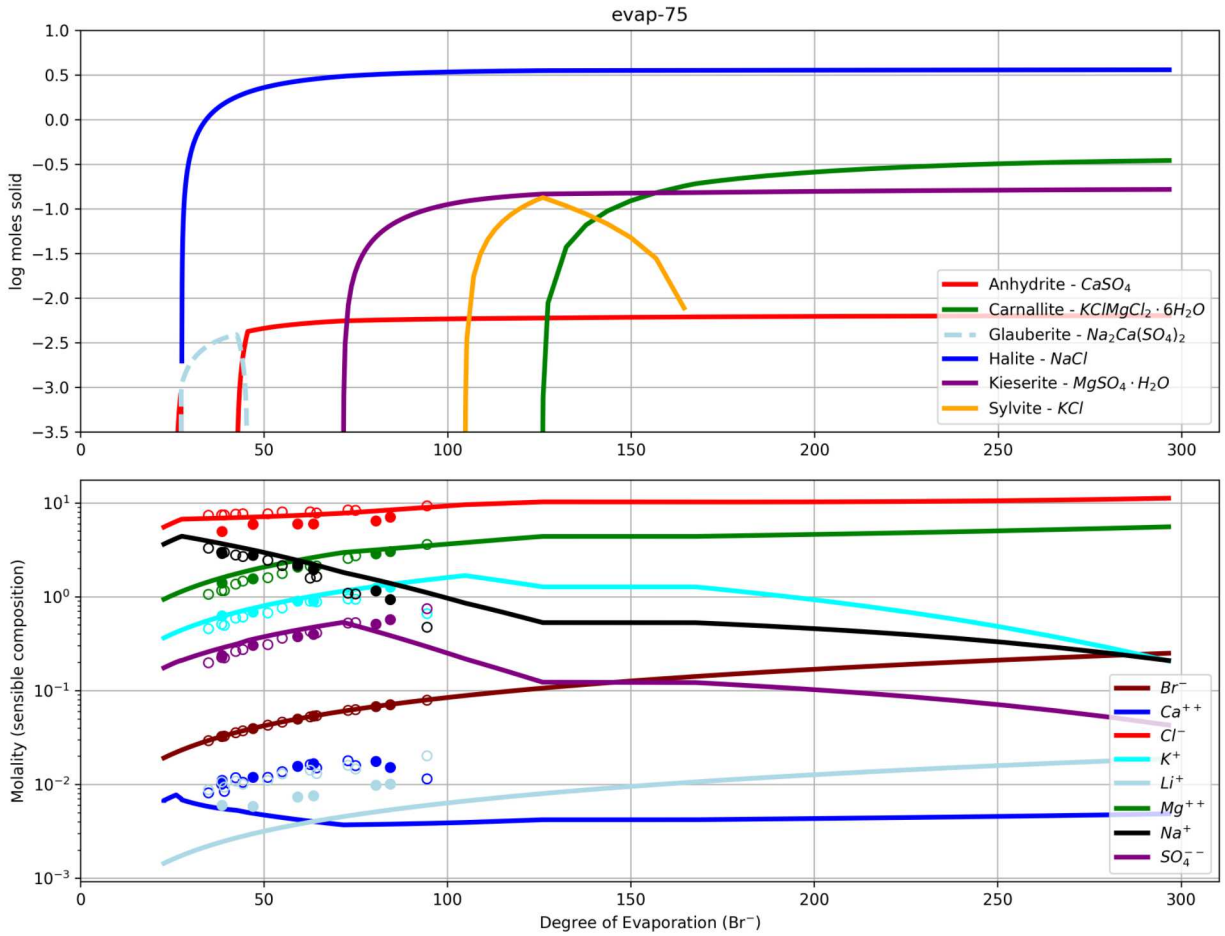

Figure 20. EQ3/6 predicted liquid and solid components during evaporation at 75 ºC; solid markers are samples with precipitant analyses

The solid circles in Figure 20 correspond to the samples listed in Table 18, which were analyzed for precipitant composition by re-dissolution of solids. As stated previously, the 75 ºC evaporation experiment did not proceed as far along the degree of evaporation scale as the other experiments (dots are farther to the left in this figure). The NNLS results predicted significant amounts of sylvite in all the samples, especially the first two (1-1 and 1-2), but the EQ6 results don't show sylvite appearing until later in the evaporation experiment (orange curve in upper subplot appearing after degree of evaporation of 100). The minerals predicted to precipitate by EQ6 at early time (glauberite and anhydrite) don't involve any potassium and would not result in the high potassium levels observed. This discrepancy between model predictions and observations will be investigated further.

In the lower subplot of Figure 20, the observed value of sulfate concentration continues to rise, while the EQ6-predicted concentrations drop at a degree of evaporation of about 75. Similar to the 50 ºC data, lithium and calcium ion concentrations are again higher in observations than in EQ6 predictions. Calcium ion concentration again drops in the EQ6 prediction because of the appearance of glauberite, which was not seen in the NNLS data, or in the calcium ion concentrations.

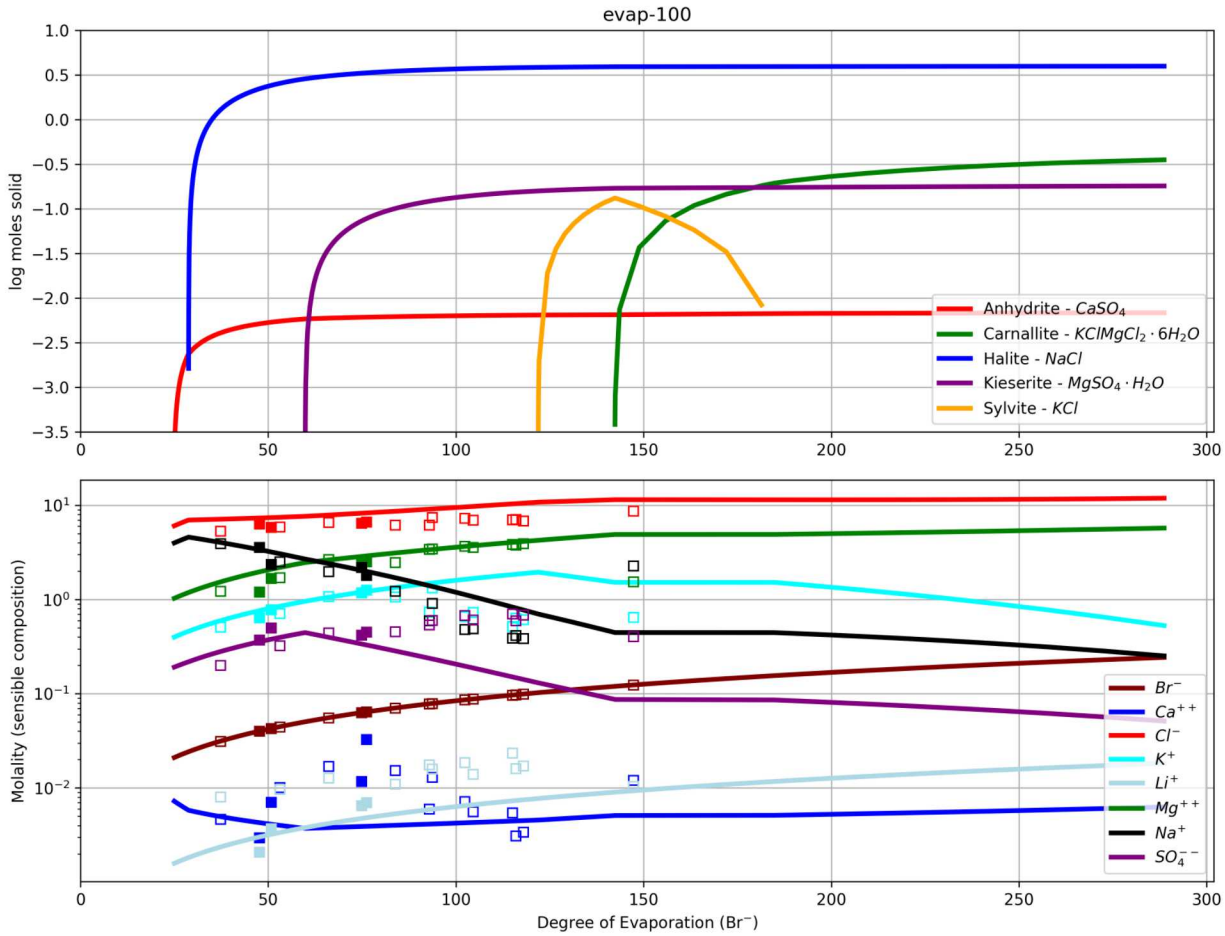

Figure 21. EQ3/6 predicted liquid and solid components during evaporation at 100 ºC; solid markers are samples with precipitant analyses

The solid squares in Figure 21 correspond to the samples listed in Table 19, which were analyzed for precipitant composition by re-dissolution of solids. EQ6 and the NNLS analysis both predict mostly halite, but the minor species predicted by NNLS do not correspond to those predicted by EQ6 (anhydrite and kieserite). Similar to the lower-temperature experiments, the observations of sulfate at late time, lithium, and calcium are generally higher than those predicted by EQ6 (see lower subplot of Figure 21). At 100 ºC calcium ion concentrations drop in the EQ6 prediction due to the appearance of anhydrite, which is not predicted by the NNLS results or the calcium ion concentrations.

Kinks in the plots of liquid composition predicted by EQ3/6 and observed in lab data represent chemical divides, which are where a new solid phase appears (corresponding to "stages" in Table 5 seawater data). This new solid phase further constrains the composition of the solution. For a solid formed from two ions (e.g., NaCl), the ion that is present in higher concentrations (e.g., Cl^-) will continue to increase after the divide, while the concentration of the species that exists at lower levels (e.g., Na^+) will decline. This is due to the mass-action constraint.

2.4.8 EQ3/6 Mixing Analysis

The brines appearing in WIPP boreholes may come from any or all of the three contributing types of water in salt: intergranular water, intragranular water, and hydrous minerals.

To gain further insight into the processes that drive brine formation, an additional study was done regarding solution mixing. Starting compositions from five WIPP sites were used: MU-0, group 2 of the fluid inclusions from Stein & Krumhansl 1988, MB-139, MB-140, and the dissolved WIPP salt. Eight pairings of these sample compositions were mixed together using EQ3/6. First, both solutions were equilibrated using EQ3. One solution was then titrated into the other in EQ6, in a 100:1 ratio, such that a large amount of the titrant was added. This titration produces a curve connecting the points representing all solution to all titrant. These results (Figure 22) show dashed lines plotting the mixing path on the mass-ratio plot follows a mostly-straight but slightly curved line between the mixed endpoints.

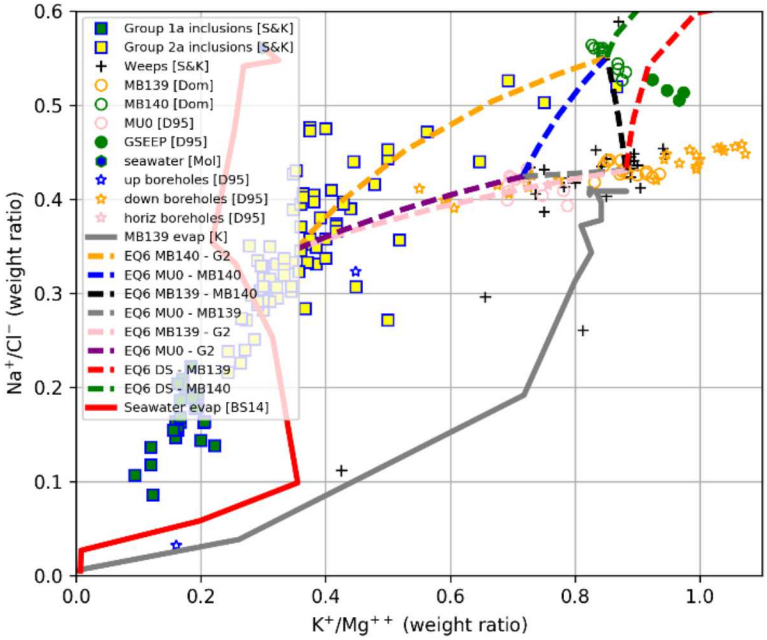

Figure 22. Mass ratios for mixed brines; dashed lines show mixing paths

2.5 Future Work

The numerical modeling and laboratory investigations discussed in this section show the complications associated with laboratory analyses and geochemical modeling of hypersaline brines. In the future, multiple quantitative comparisons will be made between modeling results and laboratory data (using the mass ratio plots, the evaporation evolution plots, and Jänecke diagrams), to improve simulations and understanding of the geochemical systems. The mineral phases observed in the experiments will be compared quantitatively to predictions of stable phases at all three temperatures. Some minerals can be suppressed in the EQ6 simulation, to see if the model results then more closely resemble the liquid and solid observations during evaporation.

Investigations will be made regarding the use of other thermodynamic databases or thermodynamic data for compositional models, which have been produced for work with high ionic strength brines (e.g., the Nuclear Energy Agency's Thermochemical Database Project https://www.oecd-nea.org/dbtdb/tdbdata/). There are fewer thermodynamic data available to constrain models at elevated temperatures, which may result in more uncertainty in model predictions.

Future work will quantify and assess the importance of uncertainty of both laboratory measurements and numerical model predictions. This quantification will help identify the level of match to be expected between the numerical model and field observations, given their inherent uncertainties. Numerical models will be used to check and report the charge balance of laboratory analytical measurements, since the large

number of complexes associated with each ionic species make manual computation of charge balance more difficult and error-prone.

Additional parameters will be measured in future laboratory brines and samples collected from the field to better constrain their composition and degree of evaporation. More effort will be put into estimating pH accurately. Additional measurands include specific gravity and electrical conductivity.

2.6 References

Adams, S.S., 1969. *Bromine in the Salado Formation, Carlsbad Potash District, New Mexico*. Bulletin 93. Socorro, NM: New Mexico Bureau of Mines and Mineral Resources.

Babel, M., B.C. Schreiber, 2014. Geochemistry of evaporites and evolution of sea water. *Treatise on Geochemistry*, 2(9): 483-560.

Boukhalfa, H., P.J. Johnson, D. Ware, D.J. Weaver, S. Otto, B.L. Dozier, P.H. Stauffer, M.M. Mills, E.N. Matteo, C.G. Herrick, M.B. Nemer, K.L. Kuhlman, Y. Wu & J. Rutqvist, 2018. *Implementation of a Small Borehole Heater Test at WIPP*. M3SF-18LA010303014, Los Alamos National Laboratory.

Deal, D.E., R.J. Abitz, D.S. Belski, J.B. Case, M.E. Crawley, C.A. Givens, P.P.J. Lipponer, D.J. Milligan, J. Myers, D.W. Powers and M.A. Valdivia, 1995. *Brine Sampling and Evaluation Program 1992-1993 Report and Summary of BSEP Data since 1982*. DOE-WIPP 94-011, Carlsbad, NM: Westinghouse Electric Corporation.

Eugster, H.P., C.E. Harvie & J.H. Weare, 1980. Mineral equilibria in a six-component seawater system, Na-K-Mg-Ca-SO_4-Cl-H_2O, at 25 °C, *Geochemica et Cosmochimica Acta*, 44(9):1335-1347.

Hardie, L.A. & H.P. Eugster, 1970. The evolution of closed-basin brines, *Mineralogical Society of America Special Papers, 3*:273-290.

Harvie, C.E., H.P. Eugster & J.W. Weare, 1982. Mineral equilibria in a six-component seawater system, Na-K-Mg-Ca-SO_4-Cl-H_2O, at 25 °C. II: Compositions of the saturated solutions, *Geochemica et Cosmochimica Acta*, 46(9):1603-1618.

Johnson P.J., Boukhalfa H., Weaver D.J., Otto S., Dozier B.L., Stauffer P.H., Mills M.M., Matteo E.N., Kuhlman K.L., Rutqvist J., & Wu Y, 2017. *Test Plan Document for Thermal Testing in Salt Test Plan*, TP-18-001-REVISION 0LA-UR-17-30762, DMS-SFWD-SFWST-2017-000043.

Jové Colón, C.F., P.F. Weck, T. Hadgu, J.E. Bean, M.J. Martinez, J.G. Argüello, C.D. Leigh, and F.D. Hansen, 2012. *Thermomechanical, Hydrological and Chemical (THMC) Model Development*. SAND2013-1412P, FCRD-UFD-2013-000064, Albuquerque, NM: Sandia National Laboratories.

Kirkes, L., 2018. *WIPP Procedure SP 12-14: Use of pH Meters and Electrodes, Revision 5*. Carlsbad, NM: Sandia National Laboratories.

Krumhansl, J.L., K.M. Kimball, C.L. Stein, 1991. *Intergranular Fluid Compositions from the Waste Isolation Pilot Plant (WIPP), Southeastern New Mexico*. SAND90-0564, Albuquerque, NM: Sandia National Laboratories.

Kuhlman, K.L., M.M. Mills, E.N. Matteo, 2017. *Consensus on Intermediate Scale Salt Field Test Design*. SAND2017-3179R, Albuquerque, NM: Sandia National Laboratories.

McCaffery, M.A., B. Lazar, H.D. Holland, 1987. The evaporation path of seawater and the coprecipitation of Br- and K+ with halite. *Journal of Sedimentary Petrology*, 57(5): 928-937.

Roberts, R.M., R.L. Beauheim, P.S. Domski, 1999. *Hydraulic Testing of Salado Formation Evaporites at the Waste Isolation Pilot Plant Site: Final Report*. SAND98-2537, Albuquerque, NM: Sandia National Laboratories.

Sandia National Laboratories (SNL), Los Alamos National Laboratory (LANL) & Lawrence Berkeley National Laboratory (LBNL), 2018. *Project Plan: Salt in situ Heater Test*, SAND2018-4673R.

Stein, C.L. and J.L. Krumhansl, 1988. A model for the evolution of brines in salt from the lower Salado Formation, southeastern New Mexico, *Geochemica et Cosmochimica Acta*, 52:1037-1046.

Xiong, Y, 2008. *WIPP Procedure SP-20-4: Preparing Synthetic Brines for Geochemical Experiments*. Carlsbad, NM: Sandia National Laboratories.

3. Brine Composition Effects on Dihedral Angle

Authors: Kristopher L. Kuhlman, Jessica M. Rimsza, David C. Sassani

The dihedral angle in the halite-brine system has been shown to be a function of pressure and temperature in the experiments of Holness & Lewis (1997). Two compositional effects are discussed that can shift the dihedral angle (via changes to interfacial tension) in typical brines found geologic salt deposits, compared to pure NaCl used in experiments. First, the impact that additional ions in solution have on the interfacial tension at a constant pressure and temperature is considered. This then can impact the dihedral angle under field-relevant conditions. Secondly, the laboratory experiments of Holness & Lewis (1997), which were performed at halite saturation, rather than at constant composition are considered. These two compositional effects imply the previously published relationship of dihedral angle to pressure, temperature, and burial depth should be modified to be more applicable to real-world evaporite deposits of variable brine composition.

3.1 Introduction

Bedded salt formations have very low porosity and low permeability and are therefore considered as candidates for permanent isolation of radioactive waste. The permeability of salt is known to be very low far from excavations (unmeasurably low), such that it is used for containment of hydrocarbons and industrial gases in man-made caverns in addition to salt domes naturally being large-scale hydrocarbon traps over geologic time scales (Beauheim & Roberts, 2002).

Lewis & Holness (1996) state the connectivity of the network of pores in halite (NaCl-water brine system) can be related to the dihedral angle, which is the angle where two salt grains meet with a compatible brine. This connectivity defines the permeability in the salt, as the halite crystals are impermeable themselves. This relationship in the halite-brine system is drawn via analogy to a solid-liquid metal system known to metallurgists. At equilibrium the dihedral angle between solid and liquid metal is a function of pressure (P), temperature (T), and composition (μ). At higher pressure or higher temperature, the dihedral angle decreases allowing more connectivity of brine along grain boundaries, which increases permeability at the same porosity. The equilibrium relationship illustrated in Lewis & Holness (1996) is for halite crystals and a Na-Cl brine in equilibrium (i.e., at saturation) with those crystals. If the solid phase is not halite (i.e., contains other chemical components besides NaCl and H_2O), or if the pores are filled with hydrocarbons, gas, or vapor, the equilibrium relationship between solid and liquid (or vapor) is different.

As presented by Holness & Lewis (1997), the pressure-temperature dependence mechanism for dihedral angle is convolved with the changes in solubility of NaCl, since the experiments were not performed at constant composition, but at NaCl saturation, which is itself a function of pressure and temperature. Separation of variables should be done explicitly in order to incorporate additional chemical components into the model for consideration of more realistic salt systems. As such, other chemical variables affecting NaCl saturation (i.e., composition of the brine, including presence of other ionic components) should affect the diheral angle as well. The confirmatory laboratory measurements (Holness & Lewis, 1997) were with pure NaCl and DI water. Geologic salt/brine systems have other components in both the solid phase (e.g., anhydrite, polyhalite, and clay) and the brine phase (e.g., Mg^{++}, K^{+}, Br^{-}, and $SO_4^{=}$), which increase the ionic strength (I) of the brine compared to the simpler NaCl-only system. Such increases in I should increase the interfacial tension associated with the brine, which increases the dihedral angle at constant pressure and temperature. The pressure-temperature-dihedral angle relationships derived for pure NaCl systems would not be applicable to real-world evaporite deposits but would need to be adjusted to incorporate such for compositional effects explicitly.

Microscopic analyses of salt core samples collected before and after heating in the upcoming WIPP heater test could be analyzed to estimate the dihedral angle and quantify any changes that might occur to it due to heating or changes in pressure.

3.2 Dihedral Angle as a Function of Interfacial Tension

Smith (1948) illustrated how connectivity of molten-metal filled porosity in an equilibrium liquid-solid system arises from a dihedral angle $< 60°$, based solely upon geometrical considerations (i.e., force balance). Smith (1948) initial considered solid and molten metal, and his approach has been extended directly to the ice and liquid water system. The extension of the approach to the salt-brine system is analogous, but not exact because the solid-liquid metal system or the ice-water system both represent single component systems where only *P* and *T* effects need to be considered. That is, for those systems, the impacts of multicomponent solutions and compositional changes to the properties of the solvent have not been fully understood explicitly in the literature. The empirical relations defined for the NaCl-brine (saturated) system provide a substantial starting point, but the compositional effects (*I* in this case) need to be explicitly separated from the *P* and *T* effects before additional chemical components can be incorporated.

At a junction of two solid grains and a liquid (Figure 23), the balance of the "grain boundary tension" $\gamma_{a_1a_2}$(between two solid grains of the same material) and components of the "interfacial tension" γ_{a_1b} or γ_{a_2b} (between liquid and common solids comprising two different grains) is what determines the dihedral angle (angle between solid-liquid interfaces of two different grains). Dihedral angle ($0 \leq \Theta \leq \pi$) is

$$\gamma_{a_1a_2} = 2\gamma_{a_1b} \cos\frac{\Theta}{2}, \quad (1)$$

stated as a balance of tension forces, where a is the solid and b is the brine (these are α and β in Figure 23) and it is assumed $\gamma_{a_1b} = \gamma_{a_2b}$. If the interfacial tension term in Equation 1 (γ_{ab}, where 1,2 sub-subscripts are now dropped for simplicity) is increased, so is the dihedral angle.

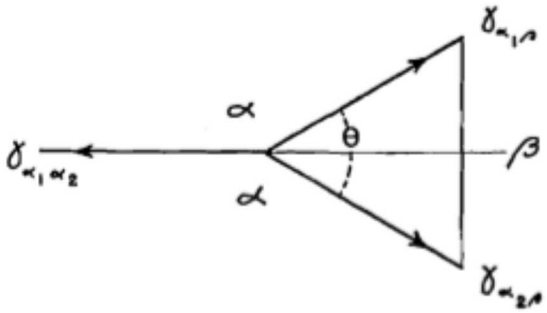

Figure 23. Intersection of two similar grains (α) and compatible liquid β, from Smith (1948). α and β in figure are a and b in text.

Smith (1948, Figure 4) shows the critical dihedral angle of 60° corresponds to a balance of forces given by

$$\gamma_{ab} = \frac{\gamma_{aa}}{2\cos\frac{\Theta}{2}}, \quad (2)$$

which corresponds to a value of 0.577 ($1/\sqrt{3}$). If the interfacial tension γ_{ab} is increased, the dihedral angle is likewise increased, with the amount of increase depending on the numerical value of the grain boundary tension γ_{aa}.

Figure 24 shows plots from Holness & Lewis (1997) that illustrate the observed differences in dihedral angle for changes in pressure and temperature in the pure H_2O-NaCl system at halite saturation. Figure 25

illustrates this same data plotted against burial depth, with green shading illustrating the impact of a change in dihedral angle from 55 to 60°.

The green area in Figure 25 is highlighted to illustrate how a small change in dihedral angle (5°) can correspond to a large change pressure (or burial depth) and temperature. Figure 26 replots the data reported by Holness & Lewis (1997), including the two-sigma error bars they reported (their data given in Table 22). The error bars for the measured dihedral angle are on the order of 6 to 10°wide.

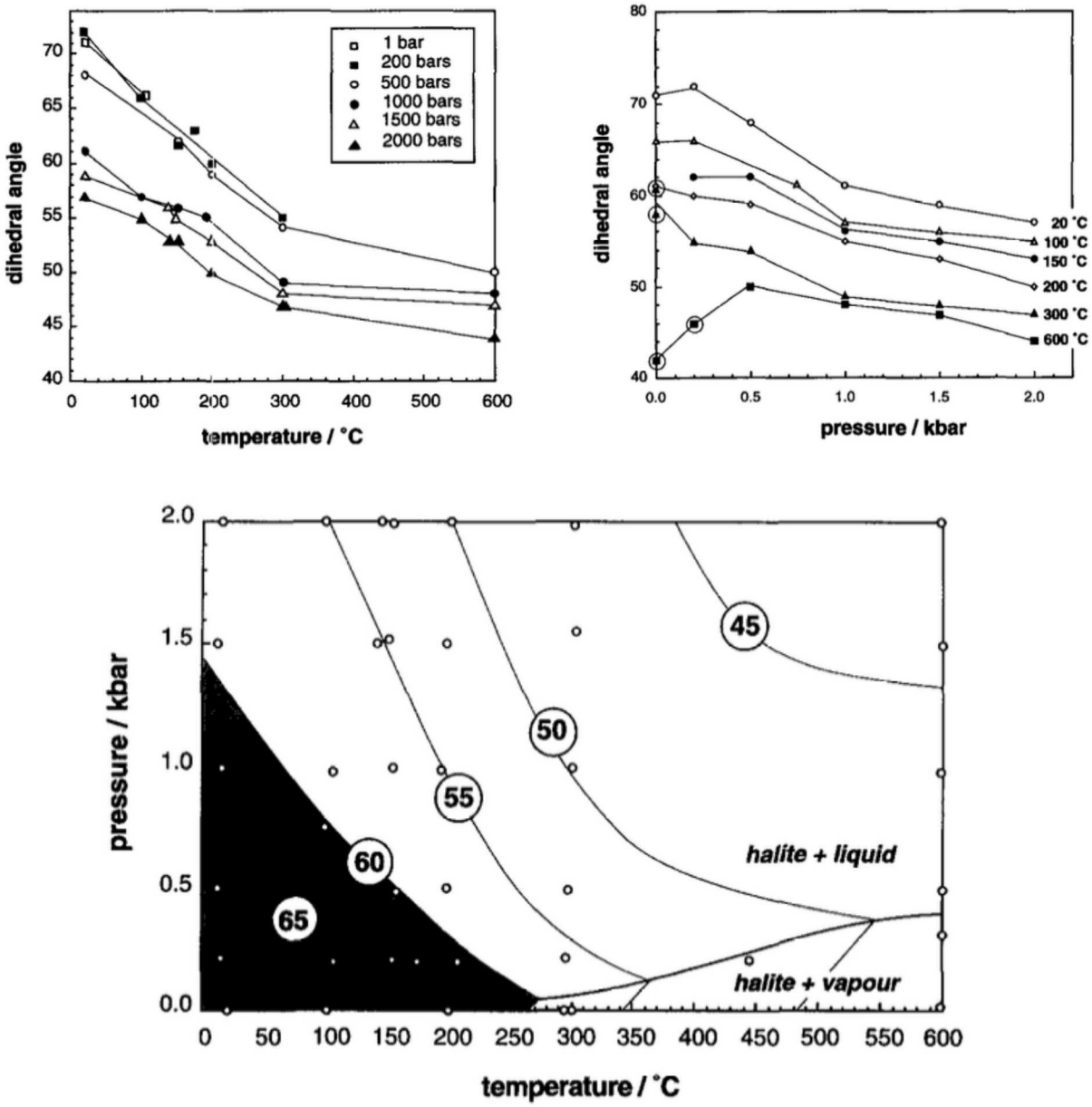

Figure 24. Laboratory-observed dihedral angle in pure NaCl-H_2O system at halite saturation (Holness & Lewis, 1997)

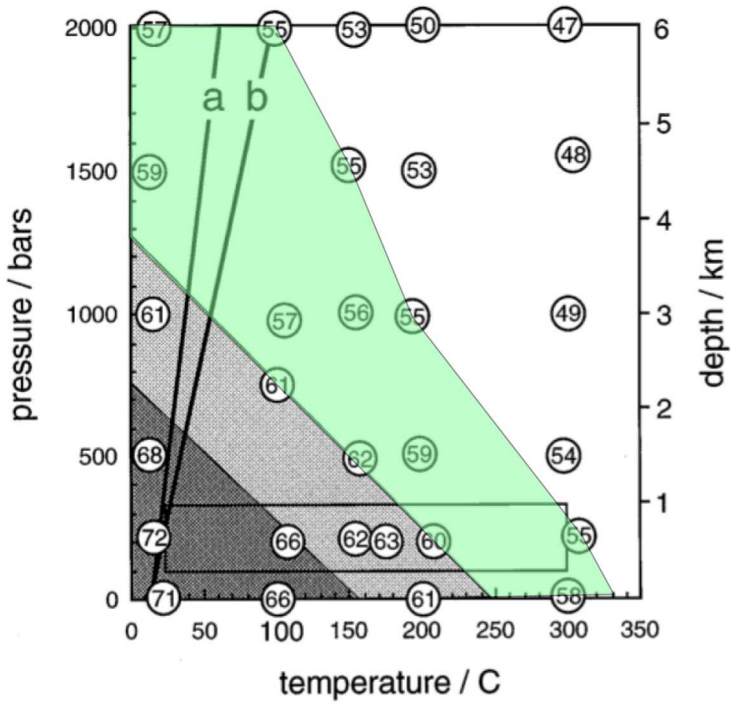

Figure 25. Θ (values circled) related to P, T, and burial depth (Lewis & Holness, 1996). Gray region is $\Theta > 60°$, where porosity should not be connected. Green region is $55° \leq \Theta \leq 60°$

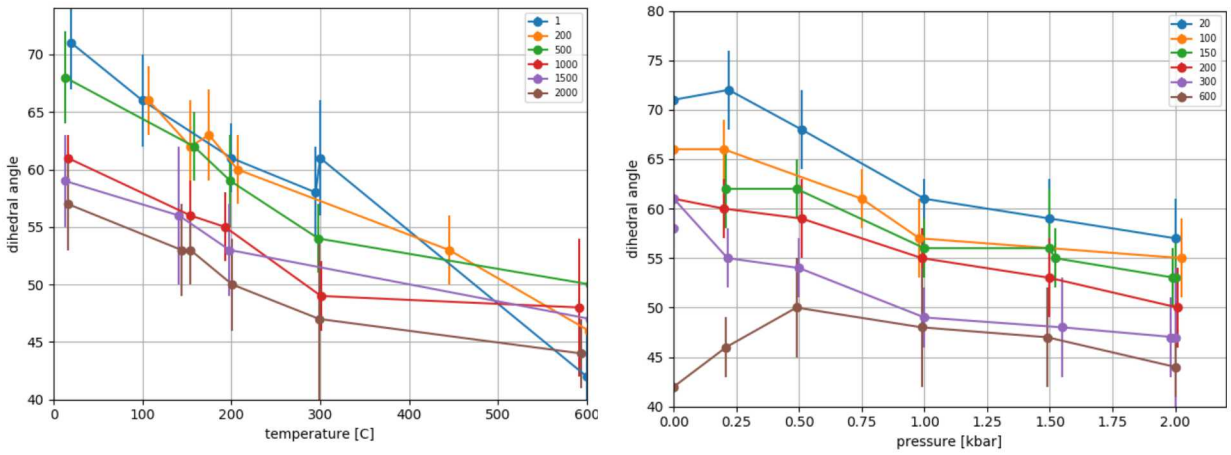

Figure 26. Data reported by Holness & Lewis (1997) (Figure 24) including their reported 2σ error bars

3.3 Dihedral Angle and Fluid Expulsion

At lower temperatures and shallower burial depths associated with radioactive waste repositories in halite, where $\Theta > 60°$, the intergranular porosity of halite is poorly connected, resulting in its well-known ultra-low permeability. This is supported by extensive observations from repository science programs and operationally through the many tight gas and petroleum storage caverns in salt domes.

Any pore fluid in salt at shallow burial depths and low temperatures is at or near lithostatic pressure (i.e., undrained conditions). This is a difficult observation to make but has been shown at depths of ~650 m at WIPP (Figure 27), where pore pressures on the order of lithostatic pressure (15 MPa or 150 bar) were observed in the far-field away from excavations. Hydrostatic pressure at WIPP is on the order of 6.5 MPa (65 bar).

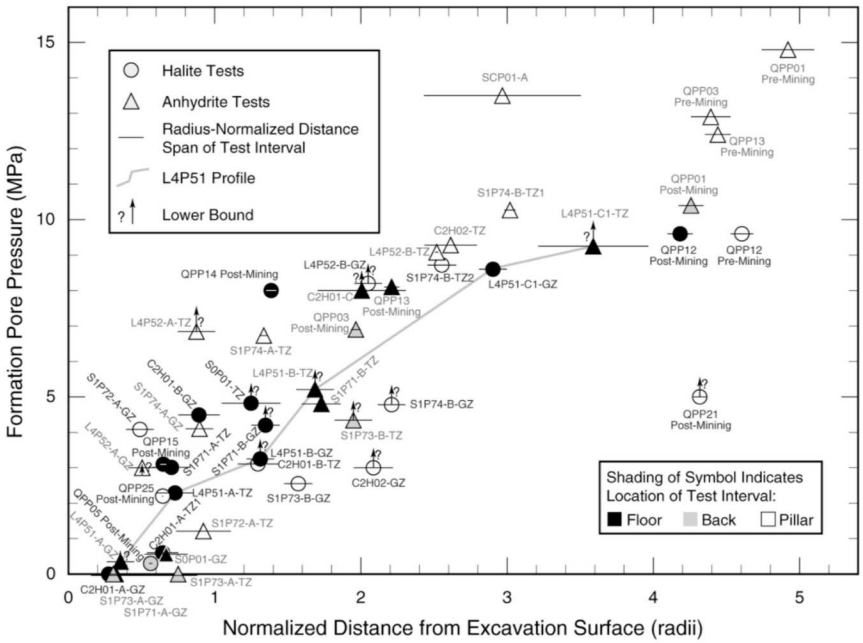

Figure 27. Brine pore pressures from hydraulic tests at WIPP (Beauheim & Roberts, 2002)

At greater burial depths where the pressure and temperature are higher, where $\Theta < 60°$, the intergranular porosity would then be more connected, allowing any overpressured (i.e., greater than hydrostatic pressure) intergranular brine to be forced out along connected pathways until the intergranular brine is at hydrostatic pressure. Therefore, when salt is buried in geologic systems to the conditions corresponding to $\Theta < 60°$, much of the brine should be drained off, resulting in halite with less intergranular brine. Using this line of reasoning, it would be expected the salt at WIPP has never experienced conditions where $\Theta < 60°$ for long enough periods of time to allow expulsion of brine, since brine at greater than hydrostatic pressure (lithostatic pressure) has been observed.

3.4 Relating Changes in Interfacial Tension to Surface Tension

Surface tension (interfacial tension between liquid and air) is well known to be a strong function of I (Pegram & Record, Jr., 2007; Shah et al., 2013). The effect has been observed to be linear and additive in the Pitzer coefficients (Li et al., 1999). This well-known increase in surface tension with I may correspond to changes in interfacial tension between brine and halite with increasing I.

3.4.1 Girifalco & Good

Starting from a balance of free energies, Girifalco & Good (1957) presented a relationship between interfacial tensions and surface tensions:

$$\gamma_{ab} = \gamma_a + \gamma_b - 2\Phi\sqrt{\gamma_a\gamma_b}, \quad (3)$$

where γ_a and γ_b are surface tensions, and γ_{ab} is an interfacial tension, and Φ represents Good's interaction parameter (Li & Neumann, 1992). Equation (3) comes from the ration of the sum of cohesion free energy within each phase to the adhesion free energy between the two phases, which is $\Delta F_{ab}^{\text{adhesion}} = \gamma_{ab} - \gamma_a - \gamma_b$, and the free energy of cohesion in each phase, given by $\Delta F_a^{\text{cohesion}} = 2\gamma_a$ (Israelachvili, 2010).

By definition $\Phi \leq 1$, and when predominant forces within the separate phases are of unlike types Φ will be small (Girifalco & Good, 1957). The actual value of Φ will depend on internal cohesion of each phase and the interaction between the two phases. Physical adsorption (i.e., van der Waals) occurs within liquids, but is not likely important between the solid and liquid at the *P* and *T* inside the earth (Holness & Lewis, 1997). Chemical adsorption involves chemical bonds (i.e., exchange or sharing of electrons), requires higher energies, and occurs at *P* and *T* within the earth. Fölsch et al. (1992) found that some water chemically adsorbs to NaCl, but most of the water is physically adsorbed at lower energies. Most of the chemically bonded water appears to be associated with the defect structure (cation vacancies) of the halite (Wassermann et al., 1993), and water tends to more strongly bond with itself (in an ice-like arrangement) than with the bulk halite (except at vacancies).

Holness & Lewis (1997) further indicate that the observed temperature-dependence of the dihedral angle in their pure NaCl-H_2O system infers that there is a negative surface excess entropy term, which indicates there is significant interaction between the two phases or components. Based on this argument, it appears most of the H_2O is adsorbed to the salt via physical adsorption, with only some chemically adsorbed to defects. It does not appear that this line of reasoning cannot be easily be used to predict *how much* less than unity Φ will be.

Li & Neumann (1992) propose an equation of state for interfacial tension in liquid-solid systems, $\Phi = \mathrm{e}^{-\beta(\gamma_a-\gamma_b)^2}$, where $\beta \approx 0.0001247 \left(\frac{\mathrm{m}^2}{\mathrm{mJ}}\right)^2$ is estimate from least-squares fitting a wide range of solids and liquids. This form shows that $\Phi = 1$ corresponds to $\gamma_a = \gamma_b$, but in most cases this term is less than unity.

Starting from Equation (3), increasing the liquid surface tension (γ_a) by a factor c (substitute $c\gamma_a$ for γ_a) would lead to a change in γ_{ab} (subtract original definition of γ_{ab}) of

$$\Delta\gamma_{ab} = (c-1)\gamma_a - \left(\sqrt{c}-1\right)2e^{-\beta(c\gamma_a-\gamma_b)^2}\sqrt{\gamma_a\gamma_b}. \quad (4)$$

The solution depends on the relative size of both γ_a and γ_b. If it is assumed $\Phi = 1$ and $\gamma_a = \gamma_b$ (the scenario where the change in interfacial tension would be the smallest), then $\Delta\gamma_{ab} = \gamma_a\left[c - 2\sqrt{c} + 1\right]$. An increase in γ_a of 15% ($c = 1.15$) would result in $\Delta\gamma_{ab} = 1.005 \cdot \gamma_a$, given these assumptions (0.5%).

Does the well-known increase in surface tension with increasing ionic strength lead to a corresponding increase the interfacial tension? It does, but the magnitude of the increase depends on γ_a and γ_b (the surface tension between solid and vapor or air), which may not be well-known.

Li & Neumann (1992) predicted γ_b from experimental measurements of liquid surface tension (γ_a) and contact angle between the liquid phase a and solid phase b (θ^*) given the best-fit β parameter as

$$\cos\theta^* = 2\sqrt{\frac{\gamma_b}{\gamma_a}}e^{-\beta(\gamma_a-\gamma_b)^2} - 1. \quad (5)$$

Assuming $\theta^* = 0$, leads to the relation $\gamma_a = \gamma_b$ (as assumed above). For a small contact angle (5°), $\gamma_b = 0.996\gamma_a$, and results in an increase in γ_{ab} of 0.55% for $c = 1.15$. Both this and the assumption for $\theta^* = 0$ are associated with a change in the dihedral angle of about 1°, e.g. (59 to 60°). This may not

seem like a large change in the dihedral angle, but it may be related back to a change in the burial depth of up to 1 km, see Figure 25 (Holness & Lewis, 1997; Lewis & Holness, 1996; Ghanbarzadeh et al., 2015).

3.4.2 Guggenheim

Holness & Lewis (1997) present surface chemistry thermodynamic arguments for the behavior of dihedral angle as a function of pressure and temperature, but all their experiments involved only pure NaCl and distilled water.

Interfacial tension is a function of pressure, temperature, and composition. Holness & Lewis (1997) present the relationship

$$\mathrm{d}\gamma = -\mathrm{S}^{\sigma}\mathrm{d}T - \sum_{i} \Gamma_i \mathrm{d}\mu_i + \tau \mathrm{d}P \tag{6}$$

where $\mathrm{d}\gamma$ is the change in free energy per unit surface area (either interfacial tension or surface tension), S^{σ} is the excess entropy per unit area, μ_i is the chemical potential of species i, τ is an "excess thickness term", and Γ_i is the surface excess (or deficit) of concentration (i.e., adsorption) for the ion compared to the bulk [mol/m^2]. For constant P and T, the change in the free energy is directly related to the change in chemical potential.

The concentration-dependence of interfacial tension is given at constant pressure and temperature as

$$\mathrm{d}\gamma = -[\Gamma_{\mathrm{Na}}\mathrm{d}\mu_{\mathrm{Na}} + \Gamma_{\mathrm{Cl}}\mathrm{d}\mu_{\mathrm{Cl}} + \cdots]_{P,T}, \tag{7}$$

where "…" indicates where the effects of other ions could enter into the equation (e.g., Mg^{++}, $SO_4^{=}$, or K^{+}). The change in the chemical potential can be expressed in terms of activities ($d\mu_i = RT\mathrm{d}(\log a_i)$, where a_i is the activity of electrolyte i) as

$$\mathrm{d}\gamma = -RT[\Gamma_{\mathrm{Na}}\mathrm{d}(\log a_{\mathrm{Na}}) + \Gamma_{\mathrm{Cl}}\mathrm{d}(\log a_{\mathrm{Cl}}) + \cdots]_{P,T}. \tag{8}$$

Simplifying the log differential gives

$$\mathrm{d}\gamma = -RT\left[\frac{\Gamma_{\mathrm{Na}}}{a_{\mathrm{Na}}}\mathrm{d}a_{\mathrm{Na}} + \frac{\Gamma_{\mathrm{Cl}}}{a_{\mathrm{Cl}}}\mathrm{d}a_{\mathrm{Cl}} + \cdots\right]_{P,T}, \tag{9}$$

which can be simplified into the typical form (Sullivan, 1981; Espinoza & Santamarina, 2010)

$$\Gamma_{\mathrm{i}} = -\frac{\partial\gamma}{\partial\mu_i} = -\frac{a_i}{RT}\frac{\partial\gamma}{\partial a_i}\bigg|_{P,T}. \tag{10}$$

For inorganic salts $\Gamma_{\mathrm{i}} < 0$, while for organic salts (e.g., CO_2) $\Gamma_{\mathrm{i}} > 0$. Positive adsorption of a component at the interface will reduce the interfacial energy (Bockris et al., 2002; Holness & Lewis, 1997).

Guggenheim (1940) presented this thermodynamic balance for interfaces and included the possibility for "inert components" (his page 405, §11), which are on one side of the interface, but not the other (like species in the brine, but not in the solid phase). The other components in solution that are not in the solid phase only affect the results by changing the activity coefficients (i.e., increasing the overall ionic strength of the brine), Guggenheim (1940) indicated they therefore don't appear where the ⋯ are in Equations (7 to 9).

Activity coefficients are reported for real brine and pure NaCl solutions in Table 23 and Table 24. Comparing the actual brine and NaCl-only brines, the ionic strengths are quite different (8.1 vs. 6.3 molal), and the activity coefficients for Na^+ and Cl^- are different (Cl^- is higher, but Na^+ is lower), but the sum of the log activities for Na^+ and Cl^- are both about 1.6. The balance of these terms depends on the relative magnitudes of Γ_{Na} and Γ_{Cl}, once again, estimates of their magnitude are required.

This approach (compared to the expression of Girifalco & Good (1957) presented in the previous section) leads to a similar assessment of a "second-order" effect of brine composition on the interfacial tension, but as shown in Figure 25, a large change in interfacial tension is not required to impact dihedral angle.

3.5 Interfacial Tension Change Estimates via MD Simulation

The effects brine composition has on interfacial tension are investigated directly using molecular dynamics (MD) simulation, rather than through analogous changes to surface tension, as discussed in the previous section. Classical MD simulations were employed to take advantage of the atomic resolution and highly controlled conditions that provide mechanistic insight into salt-brine interactions.

3.5.1 Introduction

Molecular dynamics (MD) is an atomistic simulation method for the prediction of material properties (Lee, 2016). The methodology is based on classical mechanics with interatomic forces specified by Newton's equation

$$F = ma = m\frac{\mathrm{d}v}{\mathrm{d}t} = m\frac{\mathrm{d}^2r}{\mathrm{d}t^2} = \frac{\mathrm{d}p}{\mathrm{d}t}, \tag{11}$$

where, F is force, a is acceleration, v is velocity, t is time, r is position, and p is momentum. Once the forces (and momentum) on each atom at a time are known the system is advanced in time (usually on the order of femtoseconds), after which the forces are updated, and the system iterates again. In this way the atomic system evolves with time.

Since Newton's equations of motion are easy to solve for atom-atom interactions, millions of atoms can be simulated simultaneously. MD simulations require empirical interaction potentials, or force fields, to describe the interatomic forces. The force field treats the atom as a whole, without differentiating between the nuclei and electrons. Therefore, MD is used only for predicting structural and kinetic properties and cannot be used for electronic or magnetic properties. The most common force field type is two-bodied, which includes two aspects of the atomic interaction and only considers interactions between atoms pairs. One of the simplest two-bodied potentials is used, a Lennard-Jones or "12-6" force field. It predicts potential energy given an energy (ε) and a characteristic length (σ) and the interatomic distance (r) between the two atoms,

$$U_{LJ}(r) = 4\varepsilon\left[\left(\frac{\sigma}{r}\right)^{12} - \left(\frac{\sigma}{r}\right)^{6}\right]. \tag{12}$$

For identification of brine-salt interactions a force field is required that can simulate salt components under both a solid and in aqueous conditions, as well as an appropriate water model.

Available force fields include AMBER, CHARM, and OPLS (Giri & Spohr, 2017), and available water parameters include SPC/E, TIP3P, and TIP4P (Joung & Cheatham, 2008; 2009). Comparison and discussion of these force fields have been performed (Giri & Spohr, 2017; Joung & Cheatham, 2009) as the interest in salt solutions continues to increase in geological, materials, and biological sciences. Our interest in mixed brine compositions limits the number of applicable force fields. Parameters used include: Lennard-Jones style force field by Joung & Cheatham (2008), a SPC/E water model, and parameters given in Table 21. The Joung-Cheatham force field was parametrized for a wide selection of anions (Li^+, Na^+, K^+, Rb^+, Cs^+) and cations (F^-, Cl^-, Br^-, I^-) and focused on both the structure of the

ions in liquid (hydration energies, ion-water binding energies, radii of first hydration shells) and the crystal properties (lattice energies, lattice constants). Even more favorably, the Joung-Cheatham force field was found to be the most accurate for the chemical potential of NaCl in water as well as the solubility limit, predicting 4.8 M from free energy calculations, 5.1 M for coexistence simulations (Aragones et al., 2012).

Table 21. Ion Lennard-Jones parameters (Aragones et al., 2012)

L-J Interaction	ε/Kb [K]	σ [Å]	q [e]
O-O	78.20	3.166	-0.8476
H-H	-	-	0.4238
Na^+- Na^+	177.457	2.159	1.0000
Cl^-- Cl^-	6.434	4.830	-1.0000

High concentration brines represent a unique challenge for MD simulations. The first is that the structure of high concentration NaCl brines starts to change drastically once concentrations exceed 1.0 M and can become unreliable above 2.0 M. Several of the proposed force fields (Luo & Roux, 2009) start to provide unphysical results in this regime. Issues include under- or over-estimation of the solubility limit (Aragones et al., 2012) or the formation of ion clusters (Giri & Sporh, 2017). The deviation of MD predictions from experimental results in high molarity simulations has been attributed to using a mixing rule with a Lennard-Jones type force field (Luo & Roux, 2009), and significant effort has been put forth to characterize this effect in the MD modeling community. Recent work by Giri and Spohr (2017) have noted that the formation of cluster is particularly sensitive to selection of the O-Cl interaction parameter, which will be investigated further in future work. A Lorentz-Berthelot mixing rule is used ($\sigma_{ij} = \frac{\sigma_{ii}+\sigma_{jj}}{2}$, $\varepsilon_{ij} = \sqrt{\varepsilon_{ii}\varepsilon_{jj}}$). All simulations are periodic and are performed in LAMMPS, an open-source molecular dynamics code developed at Sandia National Laboratories (Plimpton, 1995).

To identify the surface energy three system energies are required. First, a bulk NaCl system containing 5832 atoms was created in a sodium chloride crystal structure. The bulk NaCl system was relaxed under isothermal-isobaric conditions (damping coefficient set at 1000 timesteps) at 300 K for 50 ps and then cooled to 0.1 K at a 1 K/ps rate. The final energy represents the bulk NaCl system (E_B).

To investigate the surface energy the bulk NaCl system needs to be in contact with water. Therefore, a box of water molecules with an equivalent volume to the NaCl structure was placed in contact with the salt surface (Figure 28). The initial was density was 0.75 g/cm^3 and had a final density of ~1.10 g/cm^3 following relaxation. The entire system was simulated for 50 ps at 300 K with an isothermal-isobaric conditions (damping coefficient set to 10 timesteps for temperature and 1000 times steps for pressure). The system was then cooled from 300 K to 0.1 K at a 1 K/ps rate. The final energy of the system (E_{S+B}) was used for the surface energy calculation. For the salt surfaces in contact with brine solutions the same methodology was used, only the composition of the brine was adjusted through random placement of Na^+, K^+, and Cl^- ions in the water region until the desired molarity is reached. Brine compositions are discussed below. Total system sizes varied from 22,359 to 23,759 atoms, changing with the composition of the brine solution.

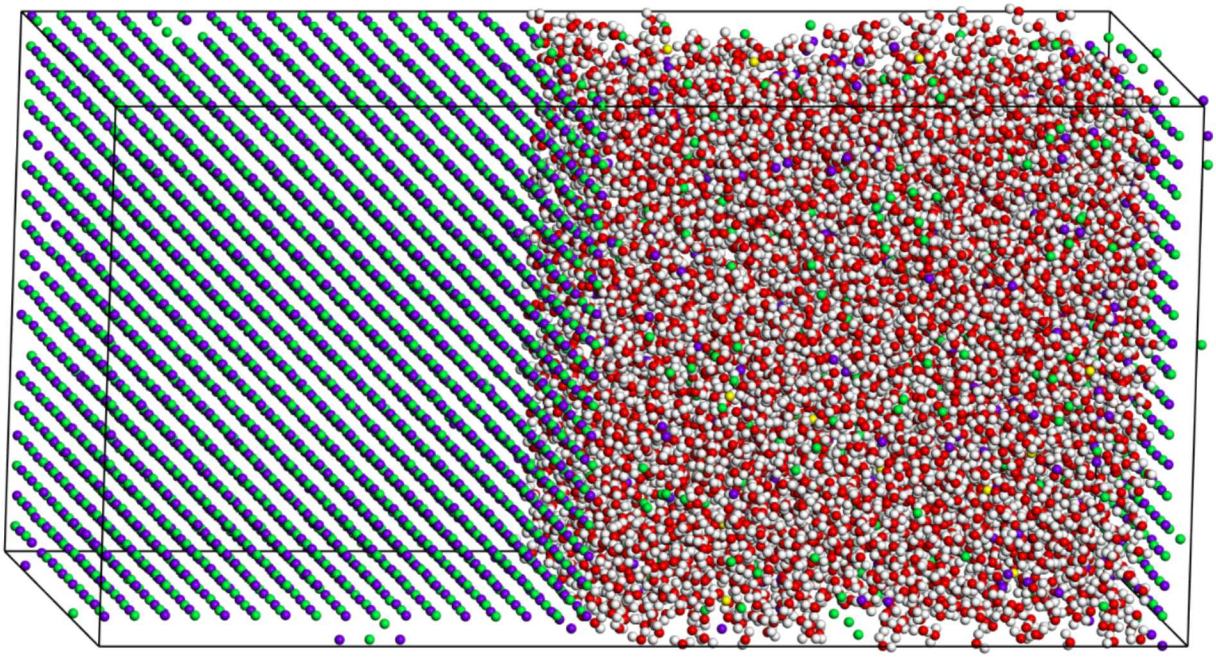

Figure 28. Snapshot of NaCl crystal in contact with a brine solution (NaCl+KCl, 2.65M). Cell Dimensions: 54.5Å×54.5Å×109.3Å. Colors: purple (Na), green (Cl), white (H), red (O), yellow (K).

The final component of the surface energy calculation requires the energy of the brine system separate from being in contact with the salt (E_B). A water box with an initial density of 0.75 g/cm^3 was generated and then the Na^+, K^+, and Cl^- ions were added to replicate the desired molar concentration of salts in solution (discussed below). The systems were simulated for 50 ps at 300 K with isothermal-isobaric conditions (damping coefficient set to 10 timesteps for temperature and 1000 times steps for pressure). Final energies were used for the E_B parameter.

Overall, three different types of brines were considered: NaCl, KCl and NaCl+KCl (here to represent composition of brines at WIPP). These brines were selected based on the typical molarities of the brines at WIPP. The NaCl brine concentration (0.0 M, 1.0 M, 3.0 M, 5.0 M, 7.0 M) was varied from 0.0 M (water) to 7.0 M to exceed the NaCl solubility limit. The KCl concentrations are much lower (0.1 M, 0.3 M, 0.5 M, 1.0 M) to encompass the range of KCl compositions reported for a typical WIPP Brine composition (0.42 M) reported in Table 15. The NaCl+KCl concentration was in an intermediate range (1.33 M, 2.65 M, 4.00 M, 5.30 M) and includes the high and low strength salt concentrations. For the NaCl+KCl the NaCl:KCl ratio is 53:6, so the brine contains 8.8 times more Na^+ ions than K^+ ions.

Since the precise location of the solvated ions in the brine solution can slightly alter the energy of the system, three different structures were generated, with different ion starting positions. Variation is reported as the average and the standard deviation of the three replicates unless otherwise noted.

3.5.2 Results

Structural analysis was performed to investigate how the mixed cations alter the brine. First structural investigation uses a pair distribution function, which identifies the average interatomic distance of different ion pairs in solution. In Figure 29, the O-H distance is reported with a primary peak of ~1.00 Å and a secondary peak at 1.72 Å, consistent with the intermolecular O-H bond and the hydrogen bond length of water respectively. For the hydration of the cation and anion species, the tightest solvation shell occurs with the Na^+ atom with a coordination distance of ~2.50 Å by water molecules. This is followed

by the O-O distance indicative of water clusters, at ~2.68 Å. The K^+-O peak occurs at ~2.8 Å, and Cl^--O at 3.26 Å, indicating a more open hydration shell around the anion, compared with the cation species. The Cl^--O distance is of interest, since it has been reported as controlling the formation of clusters at high molar concentrations, and therefore has a significant effect on the results (Giri & Spohr, 2017).

Looking only at the Na^+, K^+, and Cl^- interactions (Figure 29) the first primary peak appears at 2.51Å for the Na^+-K^+ pair. This is equivalent to the Na^+-O distance, suggesting that the Na^+ ions can be coordinated by water or the K^+ ion. This can influence the bulk structure of the NaCl-KCl brine, since there may be more Na^+-K^+ association.

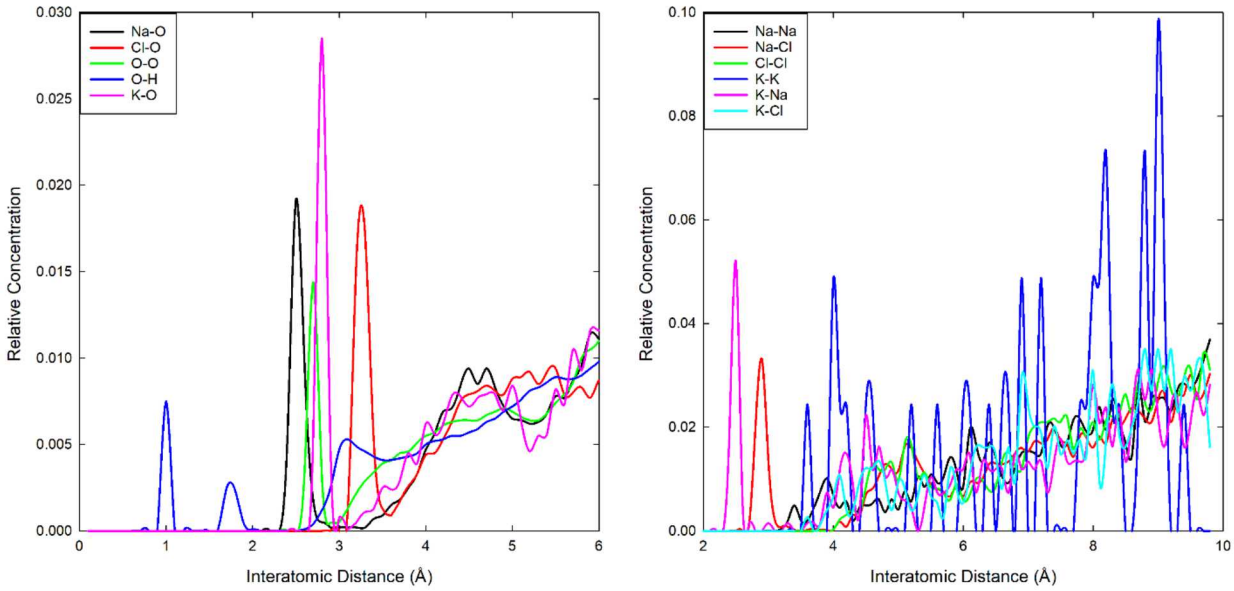

Figure 29. Pair distribution functions (PDF) of (left) oxygen containing interactions and (right) Na/K/Cl interactions for solution of NaCl-KCl at 2.65 M.

In addition to the pair distribution function, the density of the solution changes with composition. The density of the pure NaCl and KCl structures increase linearly with concentration, as would be expected when the mass of the dissolved salts increases. The outlier occurs with the mixed brines, which exhibit a peak in concentration at ~3 M (Figure 30). Some insight comes from the Na^+, K^+, and Cl^- pair distribution function (Figure 29), which indicates that there may be Na^+-K^+ association in solution. This could account for the high density in the middle range of compositions, since the Na^+-K^+ association may be increasing the compressibility of the brine, allowing for a higher density. This apparent effect will be investigated more closely in future work, looking at the role of individual Lennard-Jones parameters on the results and cluster formation at higher concentrations.

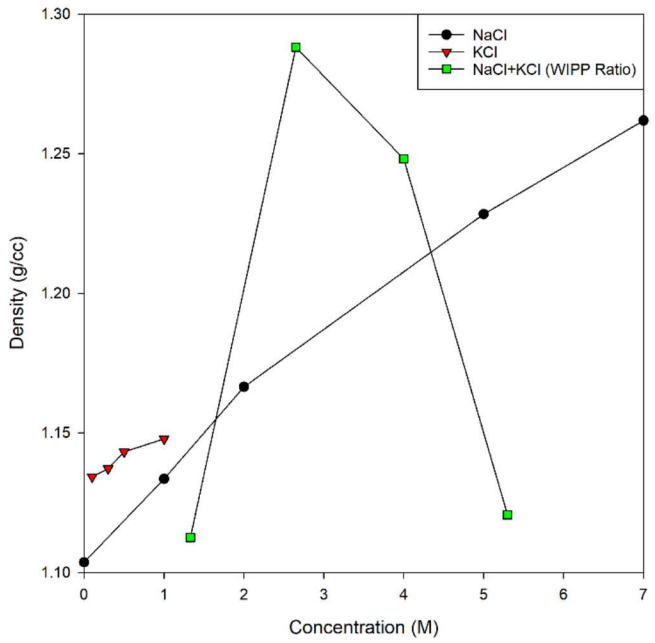

Figure 30. Predicted brine density against concentration for three different brine types (NaCl, KCl, NaCl+KCl).

Surface energy calculations used the well-established relationship

$$\gamma_S = \frac{E_{S+B} - E_S - E_B}{2S_A}. \quad (13)$$

With E_S as the energy of the salt, E_B as the energy of the brine, E_{S+B} as the energy of the combined systems, and S_A as the surface area of the interface (because the systems is periodic two surfaces are in contact with the brine). Using Equation (13), the surface energies for the three different brine solutions (NaCl, KCl, and NaCl+KCl) were compared. The surface energy increases linear with starting concentration (Figure 31). The NaCl and NaCl+KCl brines appear to have a surface energy that increases at the same rate with molar concentration, while the KCl brine shows a slightly lower slope, though more simulations will be necessary to confirm this behavior and determine if it is significant.

For analysis, the method of calculating the molarity of the brine composition becomes relevant, since the amount of dissolved salts can vary as Na^+ or Cl^- ions can reconnect with the surface during the simulation. Therefore, the molarity concentrations are reported based on the solvated Na^+, K^+, and Cl^- concentration at the end of the simulation and the final water volume. Unless otherwise stated, the salt concentration is reported as concentration of NaCl rather than the sum of the ionic components (Na^+ and Cl^- concentration). Solvated Na^+ and Cl^- ions are identified by the number of NaCl nearest neighbors. A cut-off value of 4Å is used and a bulk Na/Cl atom has a total of six nearest neighbor atoms. Surface NaCl have five nearest neighbors. A nearest neighbor concentration of less than five indicate that some level of solvation has taken place. When the molarity of the brine is recalculated based on the coordination number of the Na^+, K^+, and Cl^- constituents, the molarity decreases, as some of the ions reconnect with the surface or form clusters in solution. The surface energy continues to increase with concentration and reaches a maximum of ~13 J/m^2. Further analysis of the brine-salt interface and the possible formation of clusters in solution are being investigated. Investigations will continue to confirm and quantify what affect this can have on the dihedral angle and salt permeability.

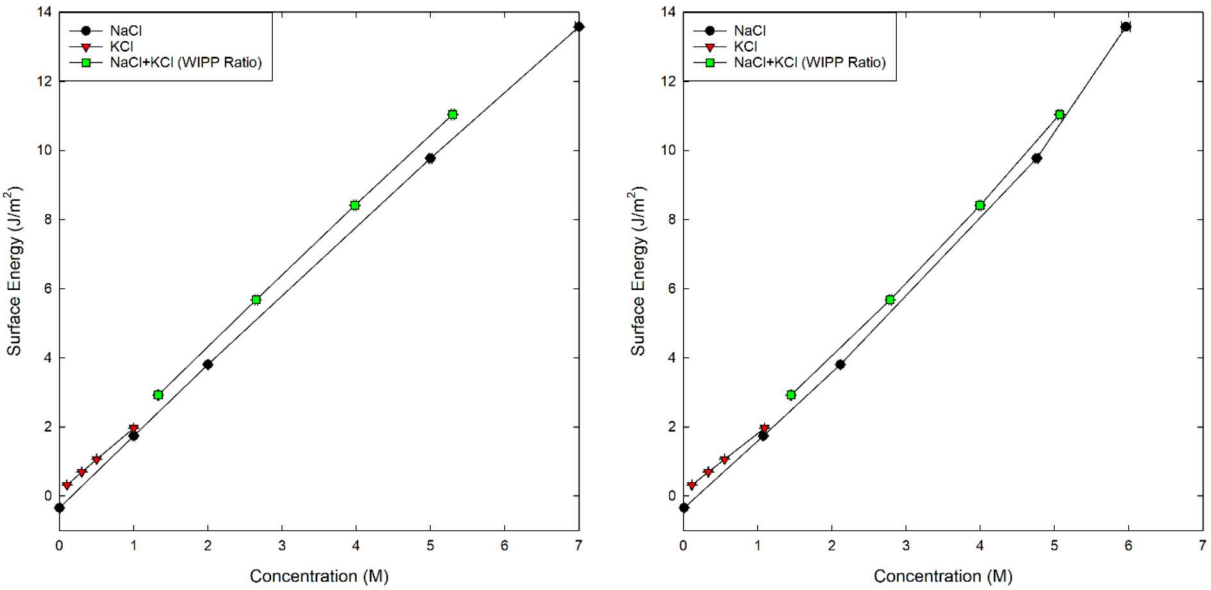

Figure 31. Surface energy as a function of concentration for three different brine mixtures (NaCl, KCl, and NaCl+KCl). Error bars are standard deviation from three different initial starting configurations.

3.6 Composition and Temperature Effects

In experiments conducted by Holness & Lewis (1997), shown in Figure 24, the change in dihedral angle for the halite-NaCl brine system is related to changes in pressure and temperature. Each term on the right-hand-side of (6) implicitly assumes the other terms are held constant, as they are total differentials. The experiments were conducted at halite saturation, not constant composition, so some contribution of the change in dihedral angle associated with changes in temperature could be attributed to changes in composition, which are related mostly to increased solubility of halite with temperature.

Table 22 shows the data from Holness & Lewis (1997) below 350° C, where EQ3 was used to predict the ionic strength of a halite-saturated solution at that pressure and temperature. Figure 32 shows a similar relationship for dihedral angle shown in Figure 25, but with the *x*-axis is ionic strength instead of temperature.

Table 22. Data from Holness & Lewis (1997) below 350 ºC with EQ3-predicted ionic strengths

pressure [bars]	temp [°C]	dihedral angle	EQ3 ionic strength [molal]
1	20	71 ± 4	6.2
1	100	66 ± 4	6.6
1	200	61 ± 3	8.0
1	295	58 ± 4	9.2
1	300	61 ± 5	9.3
220	16	72 ± 4	6.1
200	107	66 ± 3	6.7
210	154	62 ± 4	7.3
200	175	63 ± 4	7.6
200	207	60 ± 3	8.1
215	309	55 ± 3	9.7
510	13	68 ± 4	6.1
490	158	62 ± 3	7.4
510	199	59 ± 4	8.0
500	298	54 ± 3	9.3
750	100	61 ± 3	6.6
1000	16	61 ± 2	6.1
980	105	57 ± 4	6.7
1000	154	56 ± 3	7.3
990	193	55 ± 3	7.9
1000	301	49 ± 3	9.4
1500	13	59 ± 4	6.1
1500	141	56 ± 6	7.1
1520	151	55 ± 3	7.3
1500	198	53 ± 4	8.0
1550	303	48 ± 5	9.4
2000	16	57 ± 4	6.1
2025	104	55 ± 4	6.7
2000	144	53 ± 4	7.2
1990	154	53 ± 3	7.3
2010	201	50 ± 4	8.0
2000	299	47 ± 7	9.3
1980	302	47 ± 4	9.4

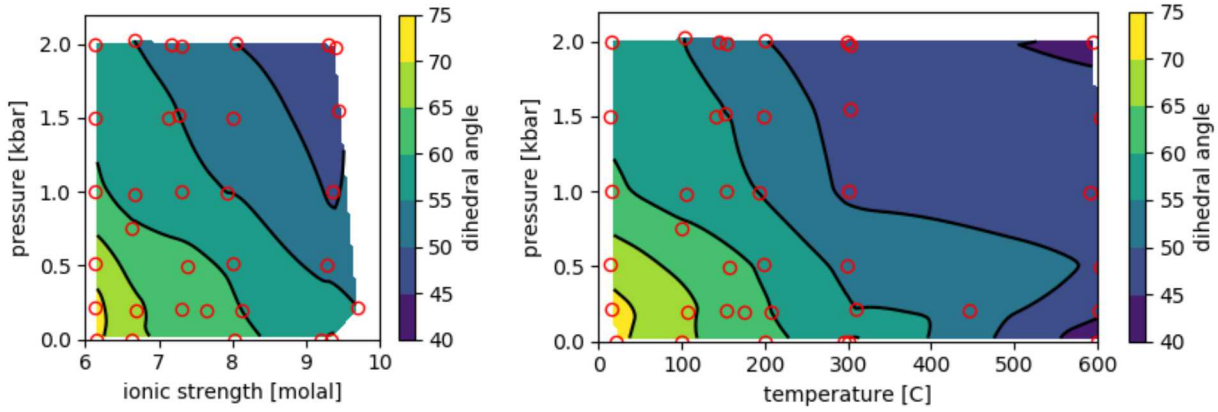

Figure 32. Dihedral angle (contour color) as a function of pressure and ionic strength (left) and pressure and temperature (right). The right plot is the same data as Figure 24, but using the same contouring algorithm as the plot on the left.

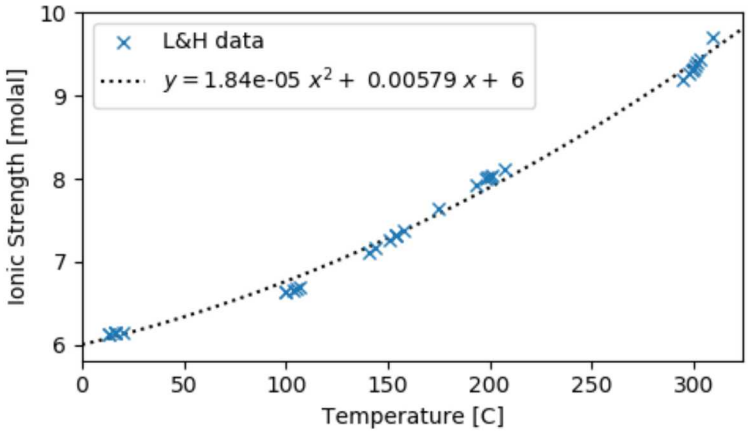

Figure 33. Relation between reported temperature and EQ3-computed ionic strength for data from Holness & Lewis (1997)

3.6.1 Brine Composition of Interest

As a "typical" example, Table 23 lists EQ3/6-simulated (Wolery & Jarek, 2003) molarities (using Pitzer activity model) of the primary ions taken from in average samples of WIPP brine (from 650 m depth and approximately 30° C), evaporated to the point of saturation with halite, sorted by decreasing molarity.

Table 23. EQ3 prediction (30 °C) of WIPP MU-0 brine at saturation; NBS pH = 6.0, *I* = 8.1 molal

ion	molarity	log activity coefficient	log activity
Cl^-	5.607	0.21	1.01
Na^+	3.672	-0.042	0.58
Mg^{++}	0.944	0.22	0.26
K^+	0.420	-0.40	-0.72
$SO_4^=$	0.180	-1.42	-2.11
$B(OH)_{3(aq)}$	0.144	0.00	-0.82
Br^-	0.020	0.39	-1.25
Ca^{++}	0.0074	-0.059	-2.27
HCO_3^-	0.00064	-0.35	-5.08
Rb^+	0.00018	-0.63	-4.31
I^-	0.00012	0.55	-3.32
Li^+	0.000053	0.39	-3.83
F^-	0.000033	-0.43	-4.84

For contrast, an EQ3/6 simulation of pure NaCl-only brine at the same point (saturation with halite) has lower ionic strength (Table 24). The sum of the log activities of Na^+ and Cl^- are the same between the two brines ($\approx$ 1.6). The activity of Cl^- is higher in the WIPP brine than in pure NaCl, but the activity of Na^+ is reduced. The ions with the next largest activity are Mg^{++} and K^+, with $SO_4^=$ less important, due to a smaller activity coefficient.

Table 24. EQ3 prediction (30 °C) of NaCl-brine at saturation; NBS scale pH = 6.3, *I* = 6.2 molal

ion	molarity	log activity coefficient	log activity
Cl^-	5.480	0.0058	0.80
Na^+	5.480	0.0058	0.80

Over the range of temperatures shown in Figure 24, the fraction of other components in evaporite deposits will change, since some evaporite minerals have a much more temperature-dependent solubility than halite (i.e., Mg-Cl salts). The activity of the different components will also change as a function of temperature.

3.7 Summary and Connections

When brines have additional ions that are not in the halite (NaCl) crystals (e.g., Mg^{++}, $SO_4^=$, and K^+), several different lines of investigation illustrate that the interfacial tension would be increased compared to pure NaCl solutions, due to the overall increase in ionic strength. An increase in the interfacial tension necessarily increases the dihedral angle. Increasing the dihedral angle makes the pore network less connected (i.e., lower permeability) at a given pressure and temperature. Increasing the ionic strength of the brine beyond that of a pure NaCl brine equilibrated with the halite crystals and adding divalent cationic constituents tends to make the pore network less connected, and the salt less permeable.

Laboratory work with pure NaCl and distilled H_2O has been reported that supports the pressure-temperature dependence of dihedral angle (Lewis & Holness, 1996; Holness & Lewis, 1997). The challenge lies in extrapolating their laboratory experiments with pure NaCl and water to realistic brine compositions under field conditions of *P* and T. The difference between field and laboratory observations, may partially be due to salt formations with brines that have higher ionic strengths than pure Na-Cl brines, as well as additional constituents, particularly divalent cationic components. The brines observed at WIPP in evaporite formations have elevated magnesium, sulfate, and potassium concentrations, too. The solid salt is >90% halite, but also includes disseminated anhydrite, clays, and polyhalite.

Further work is needed to quantify these effects fully, but the trends in real brines all indicate the dihedral angle should be increased in real systems compared to considerations of pure NaCl-H_2O system brines.

3.8 References

Aragones, J., E. Sanz & C. Vega, 2012. Solubility of NaCl in water by molecular simulation revisited, *Journal of Chemical Physics,* 136(24):244508.

Beauheim, R.L. & R.M. Roberts, 2002. Hydrology and hydraulic properties of a bedded evaporite formation, *Journal of Hydrology, 259*(1–4):66–68.

Bockris, J.O & A.K.N. Reddy, 1996. *Modern Electrochemistry*, volume 1. Kluwer, second edition.

Bockris, J.O., A.K.N. Reddy & M. Gamoa-Aldeco, 2002. *Modern Electrochemistry*, volume 2A. Kluwer, second edition.

Espinoza, D.N. & J.C. Santamarina, 2010. Water- CO_2-mineral systems: Interfacial tension, contact angle, and diffusion – implications to CO_2 geological storage. *Water Resources Research*, 46(W07537):1–10.

Fölsch, S., A. Stock & M. Henzler, 1992. Two-dimensional water condensation on the NaCl(100) surface. *Surface Science*, 264(1–2):65–72.

Ghanbarzadeh, S., M.A. Hesse, M. Prodanovic & J.E. Gardner, 2015. Deformation-assisted fluid percolation in rock salt. *Science*, 350(6264):1069–1072.

Giri, A.K. & E. Spohr, 2017. Cluster formation of NaCl in bulk solutions: Arithmetic vs. geometric combination rules*, Journal of Molecular Liquids,* 228:63-70.

Girifalco, L. & R. Good, 1957. A theory for the estimation of surface and interfacial energies I. derivation and application of interfacial tension. *Journal of Physical Chemistry*, 61(7):904–909.

Guggenheim, E., 1940. The thermodynamics of interfaces in systems of several components. *Transactions of the Faraday Society*, 35:397–412.

Holness, M.B. & S. Lewis, 1997. The structure of the halite-brine interface inferred from pressure and temperature variations of equilibrium dihedral angles in the halite-H_2O-CO^2 system. *Geochimica et Cosmochimica Acta*, 61(4):795–804.

Israelachvili, J.N., 2010. *Intermolecular and Surface Forces*. Academic Press, third edition.

Joung, I.S. & T.E. Cheatham III, 2008. Determination of alkali and halide monovalent ion parameters for use in explicitly solvated biomolecular simulations, *Journal of Physical Chemistry B*, 112(30):9020-9041.

Joung, I.S. & T.E. Cheatham III, 2009. Molecular dynamics simulations of the dynamic and energetic properties of alkali and halide ions using water-model-specific ion parameters, *Journal of Physical Chemistry B*,113(40):13279-13290.

Lee, J.G., 2016. *Computational Materials Science: An Introduction*, CRC Press.

Lewis, S. & M. Holness, 1996. Equilibrium halite-H_2O dihedral angles: High rock-salt permeability in the shallow crust? *Geology*, 24(5):431–434.

Li, D. & A. Neumann, 1992. Equation of state for interfacial tensions of solid-liquid systems. *Advances in Colloid and Interface Sciences*, 39:299–345.

Li, Z.-B., Y.-G. Li & J.-F. Lu, 1999. Surface tension model for concentrated electrolyte aqueous solutions by the Pitzer equation. *Industrial and Engineering Chemistry Research*, 38(3):1133–1139.

Luo, Y. & B. Roux, 2009. Simulation of osmotic pressure in concentrated aqueous salt solutions, *Journal of Physical Chemistry Letters,* 1(1):183-189.

Pegram, L.M. & M.T. Record, Jr., 2007. Hofmeister salt effects on surface tension arise from partitioning of anions and cations between bulk water and the air–water interface. *Journal of Physical Chemistry B*, 111:5411–5417.

Plimpton, S., 1995. Fast parallel algorithms for short-range molecular dynamics, *Journal of Computational Physics*, 117(1):1-19.

Shah, A.-u.-H.A., K. Ali & S. Bilal, 2013. Surface tension, surface excess concentration, enthalpy and entropy of surface formation of aqueous salt solutions. *Colloids and Surfaces A: Phyicochemical and Engineering Aspects*, 417:183–190.

Smith, C., 1948. Introduction to grains, phases, and interfaces – an interpretation of microstructure. *Transactions AIME*, 175:15–51.

Sullivan, D., 1981. Surface tension and contact angle of a liquid-solid interface. *Journal of Chemical Physics*, 74 (4):2604–2615.

Wassermann, B., S. Mirbt, J. Reif, J. Zink & E. Matthias, 1993. Clustered water adsorption on the NaCl(100) surface. *Journal of Chemical Physics*, 98 (12):10049–10060.

Wolery, T. & R. Jarek, 2003. *EQ3/6, Version 8.0, Software User's Manual*. US Department of Energy, Office of Civilian Radioactive Waste Management, Las Vegas, NV.

APPENDIX E
NTRD DOCUMENT COVER SHEET[1]

Name/Title of Deliverable/Milestone/Revision No. Evaluation of Spent Nuclear Fuel Disposition in Salt (FY18)

Work Package Title and Number Salt Disposal R&D - SNL

Work Package WBS Number SF-18SN01030303

Responsible Work Package Manager Kristopher L. Kuhlman.
(Name/Signature)

Date Submitted: 09/24/2018

Quality Rigor Level for Deliverable/Milestone[2]	☐ QRL-1 ☐ Nuclear Data	☐ QRL-2	☒ QRL-3	☐ QRL-4 Lab QA Program[3]

This deliverable was prepared in accordance with Sandia National Laboratories
(Participant/National Laboratory Name)

QA program which meets the requirements of

☒ DOE Order 414.1 ☐ NQA-1 ☐ Other

This Deliverable was subjected to:

☒ Technical Review ☐ Peer Review

Technical Review (TR)
Review Documentation Provided

☐ Signed TR Report or,

☐ Signed TR Concurrence Sheet or,

☐ Signature of TR Reviewer(s) below

Peer Review (PR)
Review Documentation Provided

☐ Signed PR Report or,

☐ Signed PR Concurrence Sheet or,

☐ Signature of PR Reviewer(s) below

Name and Signature of Reviewers

Kyung Won Chang Chang, Kyung

NOTE 1: *Appendix E should be filled out and submitted with the deliverable. Or, if the PICS:NE system permits, completely enter all applicable information in the PICS:NE Deliverable Form. The requirement is to ensure that all applicable information is entered either in the PICS:NE system or by using the NTRD Document Cover Sheet.*

- *In some cases there may be a milestone where an item is being fabricated, maintenance is being performed on a facility, or a document is being issued through a formal document control process where it specifically calls out a formal review of the document. In these cases, documentation (e.g., inspection report, maintenance request, work planning package documentation or the documented review of the issued document through the document control process) of the completion of the activity, along with the Document Cover Sheet, is sufficient to demonstrate achieving the milestone.*

NOTE 2: *If QRL 1, 2, or 3 is not assigned, then the QRL 4 box must be checked, and the work is understood to be performed using laboratory QA requirements. This includes any deliverable developed in conformance with the respective National Laboratory / Participant, DOE or NNSA-approved QA Program.*

NOTE 3: *If the lab has an NQA-1 program and the work to be conducted requires an NQA-1 program, then the QRL-1 box must be checked in the work Package and on the Appendix E cover sheet and the work must be performed in accordance with the Lab's NQA-1 program. The QRL-4 box should not be checked.*